ANALYSE DER LOGISTISCHEN KONSTRUKTIONS-ASPEKTE EINES SONNENSCHILDKONZEPTES IM EINFLUSSBEREICH DES SONNE ERDE L1 LAGRANGE PUNKTES

ANALYSIS OF LOGISTICAL CONSTRUCTION ASPECTS OF A SUNSHADE CONCEPT IN THE VICINITY OF THE SUN EARTH L1 LAGRANGE POINT

Master Thesis of
B.Sc. Tharshan Maheswaran
IRS-21-S-017

Supervisor:

Prof. Dr. rer. nat. Reinhold Ewald
M. Sc. Markus Graß

Institute of Space Systems
University of Stuttgart

April 2021

Abstract

Climate change is the greatest threat to mankind of the 21st century and the biggest challenge modern civilization has ever had to face [1]. The mitigation of solar radiation using sunshades is a promising strategy in terms of uniform and predictive temperature reduction, but their deployment will require several technological and logistical advancements in the upcoming decades. This master thesis deals with the analysis of the logistical construction aspects of a sunshade concept around SEL_1. Based on a roadmap incorporating previous results of lunar exploration missions as well as planned expeditions, the transfer trajectories in the Sun-Earth-Moon system have been designed. The focus is on the trajectories in the Earth-Moon system to establish a cargo hub at EML_2. In this context different orbits, their stability, as well as their accessibility and visibility to the lunar south pole region were analyzed. To ensure the transport of the high raw material masses for the construction of the sunshade constellation at SEL_1, the concept of a lunar coilgun in the Shackleton crater is introduced. The environmental conditions in the crater region allow the use of innovative superconducting technology and indicate synergy potentials for future lunar exploration missions. In addition, first estimations for a scalable concept of the lunar coilgun as well as its power supply are discussed, and overall integration of the different transportation technologies is described. Finally, aspects of an International Planetary Sunshade (IPSS) attitude and orbit control system are highlighted to realize stabilization and controllability based on existing technologies.

Kurzfassung

Der Klimawandel ist die größte Bedrohung des 21. Jahrhunderts und die essentiellste, der sich die moderne Zivilisation jemals stellen musste [1]. Die Abschwächung der Sonneneinstrahlung mit Hilfe von Sonnenschilde ist eine vielversprechende Strategie in Bezug auf eine gleichmäßige und vorausschauende Temperaturreduzierung, jedoch erfordert ihr Einsatz diverse technologische und logistische Fortschritte in den kommenden Jahrzehnten. Diese Masterarbeit befasst sich mit der Analyse der logistischen Konstruktionsaspekte eines Sonnenschildkonzeptes um den SEL_1. Auf Basis eines Strategieplans wurden unter Einbindung bisheriger Erkenntnisse von Monderkundungsmissionen sowie geplanter Expeditionen die Trajektorien im Sonne-Erde-Mond-System ausgelegt. Der Fokus liegt auf den Trajektorien im Erde-Mond-System, um einen Knotenpunkt für die Nutzlastversorgung am EML_2 zu etablieren. In diesem Zusammenhang wurden verschiedene Orbits, deren Stabilität sowie die Erreichbarkeit und Sichtbarkeit der lunaren Südpolregion analysiert. Um den Transport der hohen Rohstoffmassen für den Bau der Sonnenschildkonstellation am SEL_1 zu gewährleisten, wird das Konzept einer lunaren Coilgun im Shackleton Krater vorgestellt. Die Umweltbedingungen in der Kraterregion ermöglichen den Einsatz innovativer Supraleitertechnologien und zeigen Synergiepotentiale für zukünftige Monderkundungsmissionen auf. Darüber hinaus werden erste Abschätzungen für ein skalierbares Konzept der lunaren Coilgun sowie deren Energieversorgung diskutiert und eine Gesamtintegration der verschiedenen Transporttechnologien beschrieben. Abschließend werden Aspekte eines International Planetary Sunshade (IPSS) Lage- und Bahnkontrollsystems beleuchtet, um eine Stabilisierung und Kontrollierbarkeit auf der Basis bestehender Technologien zu realisieren.

Acknowledgement

First of all, my special thank goes to Prof. Dr. rer. nat. Reinhold Ewald, Head of the working group of Astronautics and Space Stations, enabling me the opportunity to write my master thesis at the Institute of Space Systems. My greatest debt goes to my supervisor, Mr. Markus Graß, whose active support and advice during the visionary task, guided me through the whole development process of the following concept. He helped me to structure and clarify my thoughts and encouraged new impulses. In this context, I also thank Sebastian Fix for the enthusiastic cooperation and the fruitful exchange throughout the whole development process of the roadmap. I would also like to express my special thanks to Uwe Brauer, Andreas Wiegand, and our American colleagues Ross Centers, Liz Scott, and Josh Schertz, for their constant exchange with innovative impulses and technical expertise. In addition, my special appreciation goes to Jose Tatay Sanguesa and Marius Schwinning, for their active support despite time constraints, and without whose support such a comprehensive simulative illustration with the integration of innovative tools would not have been possible.

I am grateful to all my family and especially to my parents Maheswaran Velupillai and Thayalini Maheswaran for their unrestricted care and constant support starting from my childhood and during my studies, which was an essential ingredient in this long journey and for this work.

Last but not least, my special thanks goes to my fiancée Laxshana Sivabalan. Above all, I am especially grateful for her relentless and patient advice, her support in wording, and her encouragement during the turbulent final phase of this master thesis.

Contents

List of Symbols

Latin Symbols

a	$\frac{\mathrm{m}}{\mathrm{s}^2}$	Acceleration
A	m^2	Area
A_z	m	Maximum out-of-plane amplitude
C	-	Jacobi integral
C_A	-	Absorptivity coefficient
C_D	-	Diffuse reflectivity coefficient
C_S	-	Specular reflectivity coefficient
E	J	Energy
F	N	Force
L	m	Track length
M	kg	Total mass
m	kg	Mass of body
MLR	$\frac{\mathrm{kg}}{\mathrm{s}}$	Mass launch rate
p_0	$\frac{\mathrm{N}}{\mathrm{m} \cdot \mathrm{m}^2}$	Torque of the sunlight per unit wavelength per unit area
P_P	W	Power supply
$P_{RCD,ON}$	$\frac{\mathrm{N}}{\mathrm{m}^2}$	Solar radiation pressure for RCD ON
$P_{RCD,OFF}$	$\frac{\mathrm{N}}{\mathrm{m}^2}$	Solar radiation pressure for RCD OFF
r	m	Radius
r_p	m	Perilune distance
t	s	Time

$t_{recharge}$	s	Recharge time
$t_{req,cycle}$	s	Cycle time
$\bar{T}$	Nm	Time-averaged attitude torque of RCD
TOF	s	Time of flight
$\bar{U}$	$\frac{\mathrm{m}^2}{\mathrm{s}^2}$	Effective potential of the system
v	$\frac{\mathrm{m}}{\mathrm{s}}$	Velocity
x	m	Primary axis of a Cartesian coordinate system
y	m	Secondary axis of a Cartesian coordinate system
z	m	Third axis of a Cartesian coordinate system
$\dot{x}$	$\frac{\mathrm{m}}{\mathrm{s}}$	Velocity in x-direction
$\dot{y}$	$\frac{\mathrm{m}}{\mathrm{s}}$	Velocity in y-direction
$\dot{z}$	$\frac{\mathrm{m}}{\mathrm{s}}$	Velocity in z-direction
ΔC_S	-	Difference of the specular reflectivity
ΔC_D	-	Difference of the diffuse reflectivity
ΔP_{RCD}	$\frac{\mathrm{N}}{\mathrm{m}^2}$	RCD performance
ΔV	$\frac{\mathrm{m}}{\mathrm{s}}$	Change in velocity

Greek Symbols

ε	-	Mass ratio of the primaries
η_C	-	Efficiency of coilgun
η_P	-	Efficiency of photovoltaics
λ	m	Wavelength
λ_{max}	-	Maximum eigenvalues of the state transition matrix

θ	rad	Angle to the sun
ϑ	$\frac{\text{kg}}{\text{m}}$	Mass per unit length
ν	-	Stability index
ρ_A	$\frac{\text{g}}{\text{m}^2}$	Surface density
$\psi_{in-situ}$	-	In-situ mass fraction

Constants

AU	1.496x10^{11} m	Astronomical unit
S	1,360 $\frac{\text{W}}{\text{m}^2}$	Solar constant
g	9.81 $\frac{\text{m}}{\text{s}^2}$	Standard acceleration due to gravity (near Earth surface)

List of Abbreviations

ACE	Advanced Composition Explorer
AOCS	Attitude and Orbit Control System
CNSA	China National Space Administration
CFS	Commonwealth Fusion Systems
CR3BP	Circular Restricted Three-Body Problem
DARPA	US Defense Advanced Research Projects Agency
DT	Direct Transfers
EDLC	Electro-Chemical Double-Layer Supercapacitor
EMALS	Electromagnetic Aircraft Launch System
EML_i	Earth-Moon Lagrange Point i
EMM	Electromagnetic Mortar
ESA	European Space Agency
EVA	Extravehicular Activities
GEO	Geostationary Orbit
GDP	Gross Domestic Product
GREB	Globally Resolved Energy Balance
GTO	Geostationary Transfer Orbit
HTS	High Temperature Superconductor
IKAROS	Interplanetary Kite-craft Accelerated by Radiation Of the Sun
IPCC	Intergovernmental Panel on Climate Change
IPSS	International Planetary Sunshade
ISECG	International Space Exploration Coordination Group

ISM	In-space Manufacturing
ISRO	Indian Space Research Organisation
ISRU	In-situ Resource Utilization
JAXA	Japan Aerospace Exploration Agency
JWST	James Webb Space Telescope
L_A	Artificial Lagrange Point
LC	Lunar Coilgun
LEO	Low Earth Orbit
LFB	Lunar Flyby
L_i	Libration Point i / Lagrange Point i
LOLA	Lunar Orbiter Laser Altimeter
LRA	Lorentz Rail Accelerator
LSMAT	Lunar Surface Mission Analysis Tool
MCB	Marine Cloud Brightening
MIDACO	Mixed Integer Distributed Ant Colony Optimization
MIT	Massachusetts Institute of Technology
NASA	National Aeronautics and Space Administration
NEA	Near-Earth Asteroid
NRHO	Near-Rectilinear Halo Orbit
OSAM	On-orbit Servicing, Assembly, and Manufacturing
PCM	Propulsion and Communication Module
PROSPECT	Package for Resource Observation and in-Situ Prospecting for Exploration, Commercial Exploitation and Transportation
RCD	Reflectance Control Device
RCP	Representative Concentration Pathway

RCS	Reaction Control Systems
REBCO	Rare Earth Barium Copper Oxide
SAI	Stratospheric Aerosol Injection
SEL_i	Sun-Earth Lagrange Point i
SOHO	Solar Heliospheric Observatory
SRM	Solar Radiation Management
SRP	Solar Radiation Pressure
SSO	Sun-synchronous Orbit
STM	State Transition Matrix
TLI	Trans Lunar Injection
TLO	Trans Lunar Orbit
TRL	Technology Readiness Level
WMAP	Wilkinson Microwave Anisotropy Probe
WSB	Weak Stability Boundaries

1 Introduction

Climate change is the most serious threat of the 21st century and the biggest modern humans have ever had to face [1]. Despite some unfounded skepticism, the scientific evidence of the last decades clearly proves the consequences of industrialization as well as globalization and promotes the awareness of our responsibility as well as a change of mindset among the population. The recent developments in climate research, but especially the strongly changed climatic conditions and the related natural catastrophes like the increase of hurricane strength in the US [2], the record temperatures, the heat waves, and floods have contributed to an increased interest of the population in climate change and its consequences [3].

Climate science is no longer a cornerstone discipline, but one of the essential scientific fields to prepare our generation and the generations to come for the future, which is a source of great concern for the current generation in terms of how our children will be affected in the future. The strong interest in saving the Earth and protecting human existence, due to the slow development of renewable energies, has led to a completely new scientific field - geoengineering. This field deals with the influenceability of the Earth's climate by using new intervention technologies.

However, many of the terrestrial methods have not been sufficiently investigated yet and, there is a lot of skepticism about the impact of intervening in the atmosphere and the possible side effects. But it is not only climate research dealing with this topic; climate change has already reached space technology. Space-based geoengineering approaches have already been analyzed several times in the last decades and offer today a possibility to provide us with a temporary buffer to expand renewable energies by mitigating the catastrophic consequences of climate change to a certain extent [4]. The International Planetary Sunshade (IPSS) concept is an international space-based geoengineering approach with the objective to achieve a global reduction of solar insolation by involving international collaborations.

1.1 Motivation

Time is the crucial showstopper in terms of climate change, as already stated by various scenarios in the Intergovernmental Panel on Climate Change (IPCC) reports [5]. Whereas the focus so far has been on costs and effort, it is now a question of gaining as much time as possible by preventing the passing of critical tipping points [6] in order to develop technologies in the field of renewable energies to perform the global energy transformation [7; 8]. Moreover, the IPSS concept could provide an alternative way to generate solar energy.

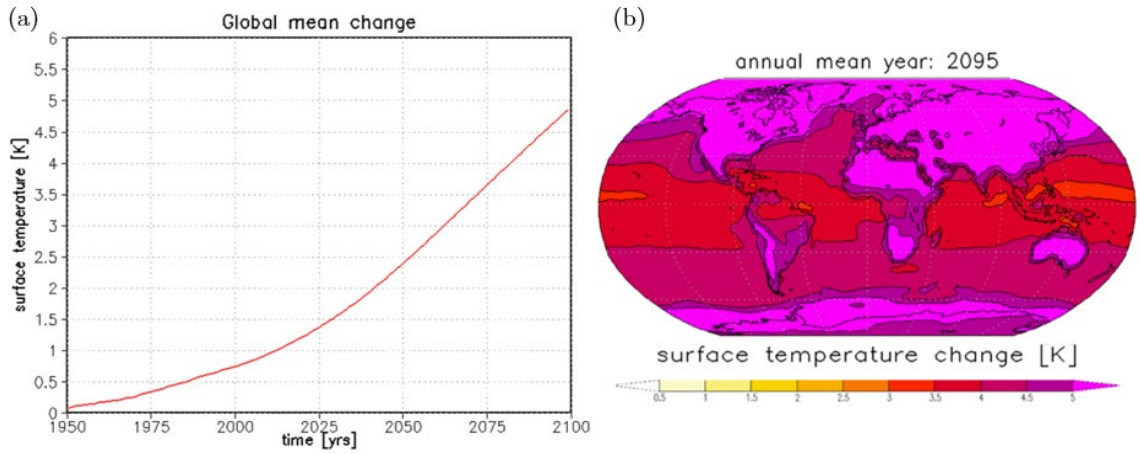

Figure 1: IPCC Scenario - RCP 8.5 CO_2-forcing. (a) Global mean change in surface temperature until 2100. (b) Global mapping of annual mean surface temperature in 2095 [9].

Figure 1 contains a selected simulation, derived from the Monash simple climate model, which illustrates the dramatic development predicted in the upcoming years [9]. A comparison of the projected temperature developments according to the IPCC illustrates the critical development. In the worst-case scenario, representing the current situation, in which no action is taken, and economic trends increase constantly an average temperature rise of 4.8 K by 2100, referenced to 1955, is expected according to IPCC Representative Concentration Pathway 8.5 (RCP8.5).

Our climate system and the associated processes are highly complex and accordingly there are a large number of tipping points in the various systems [6]. Consequently, even with the current target temperature increase of no more than 2.0 K by 2100, the mean net present value of the costs of damages is estimated to be $69 trillion due to the climate

impacts [10]. In addition, a mean annual Gross Domestic Product (GDP) loss of up to 4.5 percent (%) is projected in 2100 [11]. Thus, current technological advances are not sufficient to expand renewable energies and carbon capturing in time, whereby geoengineering can play a decisive role in providing more time for technological development. This clearly indicates the urgent demand for effective actions to be taken and implemented by 2060 [12], in order to avoid reaching the tipping point and to save our planet Earth. Consequently, for all mentioned concepts, but especially for the IPSS concept, a deadline of 2060 has to be achieved, which can only be accomplished in an international cooperation.

1.2 Objectives and Outline

Initiated by Airbus Defense and Space the objectives of this work are to analyze the different sunshade concepts in detail with regard to the logistical aspects. The major tasks focus on the investigation of possible trajectories to implement an IPSS in the vicinity of the Sun-Earth Lagrange Point L1 (SEL_1) using lunar resources. Special focus is set on the analysis of the conceptual design of a lunar launch system and a sunshade attitude and orbit control system (AOCS) taking the overall mission scenario into account.

In chapter 2, the orbital mechanics for the design of the trajectories, a short overview of solar radiation management (SRM) methods, and the investigated constellation types for a space-based sunshade concept are presented. Chapter 3 deals with the definition of the IPSS mission scenario, including the overall roadmap, the derived logistical requirements, and the logistical concept of the mission scenario. Chapter 4 describes the defined trajectories for the different mission phases with respect to the applied transfer technologies, giving an overview of the ΔV(change in velocity)-demand and possible communication windows. In chapter 5 the transfer technologies are discussed more in detail, with a special focus on the coilgun concept concluding in a synergistic approach. Chapter 6 deals with the IPSS attitude and orbit control system, demonstrating technologies to stabilize the sunshade constellation at SEL_1. At the end, a summary of the results as well as an outlook for further work are given.

Based on the upcoming analysis of logistical aspects of an IPSS system and in collaboration with a parallel thesis [13], concentrating on the In-situ Resource Utilization (ISRU) and In-space Manufacturing (ISM), a roadmap for the overall mission scenario was developed, which is primarily referenced in this work.

2 Background

This chapter deals with the fundamental principles for the configuration of the IPSS system. The fundamentals are divided into the subjects of specific orbital mechanics, solar radiation management methods, and different constellation concepts as baseline for the developed IPSS system concept.

2.1 Orbital Mechanics

The orbit design of interplanetary trajectories reveals a high complexity due to the additional perturbation effects by additional bodies as well as the varying reference systems. The mathematical model of the Circular Restricted Three-Body Problem (CR3BP) represents the motion of a spacecraft under the gravitational influence of two massive bodies. The model enables an efficient and fast analysis of the transfer possibilities, for example, in the Earth-Moon and Earth-Sun systems [14–17]. In the following, the fundamental reduction to a circular restricted three-body problem as well as the special solutions of the libration points and the resulting special orbits are presented.

2.1.1 Circular Restricted Three-Body Problem

The reference frame for the CR3BP is the circular coplanar motion of two massive bodies m_1 and m_2 around their common center of mass, where the mass of the third body m_3 is negligible. Consequently, the motion can be described in the rotating reference frame concerning the center of mass of the two bodies, the primaries. To enable a standardized description (Figure 2), the quantities of the system are normalized to the distance between the primaries, the modulus of their angular velocity, as well as to the total mass of the system, resulting in the following equations for the position as well as the velocity of the spacecraft, described by $\bar{x} = \{x,\ y,\ z,\ \dot{x},\ \dot{y},\ \dot{z}\}$

$$\begin{cases} \ddot{x} - 2\dot{y} = -\bar{U}_x \\ \ddot{y} - 2\dot{x} = -\bar{U}_y \\ \ddot{z} = -\bar{U}_z \end{cases} \qquad \text{(Eq. 1)}$$

with

$$\bar{U}(r_1, r_2) = -\tfrac{1}{2}\left[(1-\varepsilon){r_1}^2 + \varepsilon {r_2}^2\right] - \tfrac{1-\varepsilon}{r_1} - \tfrac{\varepsilon}{r_2},$$

$${r_1}^2 = (x+\varepsilon)^2 + y^2 + z^2,$$

$${r_2}^2 = (x-1+\varepsilon)^2 + y^2 + z^2,$$

$$\varepsilon = \tfrac{m_2}{m_1 + m_2}.$$

The mass ratio of the primaries is described by ε, the distances between the spacecraft and the primaries are represented by r_1 and r_2, with r_1 referring to the larger primary, and $\bar{U}(r_1, r_2)$ expresses the effective potential of the overall system.

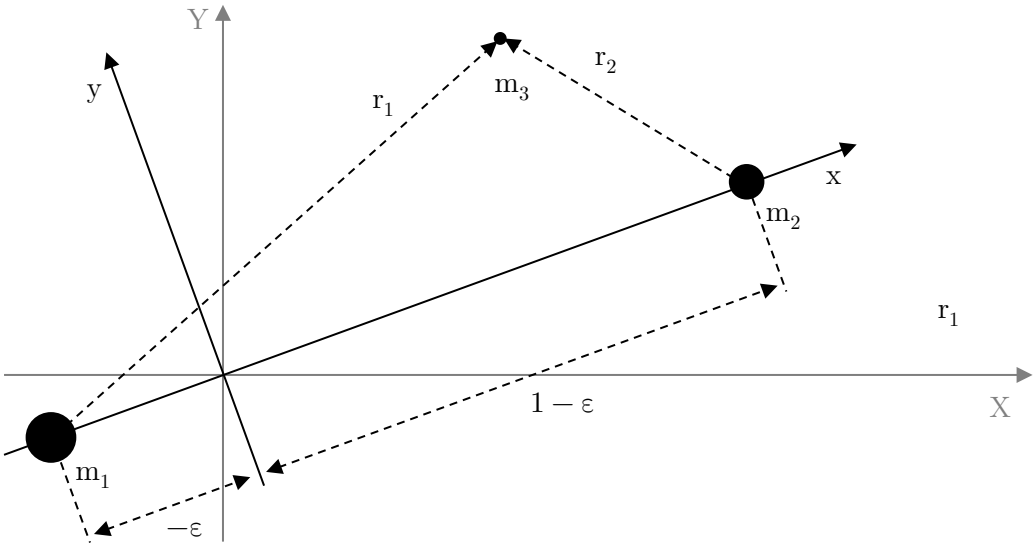

Figure 2: Scheme of the circular restricted three-body problem in normalized coordinates.

The energy integral of motion [18] of system (Eq. 1) is an essential parameter for describing orbits in the CR3BP and can be described by the Jacobi integral, defined as

$$C(x,\ y,\ z,\ \dot{x},\ \dot{y},\ \dot{z}) = -2\bar{U} - (\dot{x}^2 + \dot{y}^2 + \dot{z}^2). \qquad \text{(Eq. 2)}$$

2.1.2 Libration Points

The mathematical model of the CR3BP (Eq. 1) provides five equilibrium points, also called libration points or Lagrange Points, characterized by the stationary behavior of the spacecraft in the rotating reference frame (x-y-system). At the libration points the gravitational forces of the primaries and the centripetal force based on the spacecraft movement are mutually eliminated. The libration points can be distinguished by their location and stability (Figure 3). The unstable points L_1, L_2, L_3 are located on the

connecting line between the two primaries and form collinear configurations, whereas the stable L_4 and L_5 are situated at an angle of 60 degrees (°) to the connecting line.

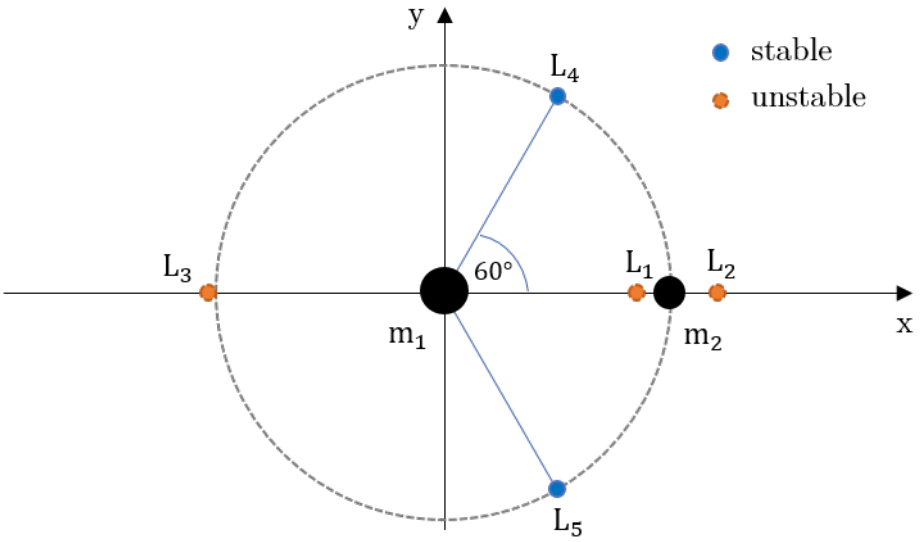

Figure 3: Plot of libration points of the circular restricted three-body problem in the x-y-plane including stability.

Due to their location and the stationary characteristics of the Lagrange points, they are of special interest for space missions. The Sun-Earth Lagrange Point 1 (SEL_1) provides an unrestricted view to the Sun and enables the investigation of the outer layer of the Sun, solar wind observations, and helioseismology [19]. Consequently, SEL_1 has already been selected for many scientific missions such as the Advanced Composition Explorer (ACE), Solar Heliospheric Observatory (SOHO), and the Global Geoscience WIND, providing a large amount of data with respect to the stabilization of different orbits [20].

The Sun-Earth Lagrange Point 2 (SEL_2) is of great importance for astronomical observations due to its constant position in the shadow of the Earth. Therefore, the Wilkinson Microwave Anisotropy Probe (WMAP) was formerly positioned here to investigate irregularities in the cosmic background radiation [21]. Due to its close distance to Earth, SEL_2 allows sufficient communication and also a clear view of deep space, which is the reason for the Planck Space Telescope [22] as well as its successor the James Webb Space Telescope (JWST) [23] to be operated at SEL_2. No missions have yet been considered for the Sun-Earth Lagrange Point 3 (SEL_3) because of its position behind the Sun. The instability of the orbits around L_1, L_2, and L_3 requires continuous course and attitude correction in a time frame of about 23 days [24]. Sun-Earth Lagrange Points 4

(SEL_4) and 5 (SEL_5) provide the only stable orbits as long as the mass ratio of the primaries is exceeding 24.96. This approximation applies to many systems in the solar system in addition to the Sun-Earth and Earth-Moon systems. Based on the natural objects around L_4 and L_5 in the Jupiter-Sun system, these objects are also called trojans [24].

The Lagrange points in the Earth-Moon system play an essential role, especially in the context of lunar exploration. The Earth-Moon Lagrange Point 2 (EML_2) enables communication with the far side of the Moon, while the Earth-Moon Lagrange Point 1 (EML_1) can serve as location for a fuel depot for orbital refueling. Both were analyzed with respect to their suitability as staging orbits for lunar missions [25].

Table 1 and Table 2 summarize the distances of the unstable L_1, L_2, L_3 for the Sun-Earth as well as for the Earth-Moon system.

Lagrange point	Position in normalized units		Position in [km]	
	x	y	x	y
SEL_1	0.9899859823	0.0000000000	148099795.0	0.0
SEL_2	1.0100752000	0.0000000000	151105099.2	0.0
SEL_3	-1.0000012670	0.0000000000	-149598060.2	0.0
SEL_4	0.4999969596	0.8660254038	74798480.5	129555556.4
SEL_5	0.4999969596	-0.8660254038	74798480.5	-129555556.4

Table 1: Position of Lagrange points in Sun-Earth system including normalized units referring to the Sun-Earth distance of 149,601,950 km [26].

Lagrange point	Position in normalized units		Position in [km]	
	x	y	x	y
EML_1	0.8369151324	0.0000000000	321710.2	0.0
EML_2	1.1556821603	0.0000000000	444244.2	0.0
EML_3	-1.0050626453	0.0000000000	-386346.1	0.0
EML_4	0.4878494157	0.8660254038	187529.3	332900.2
EML_5	0.4878494157	-0.8660254038	187529.3	-332900.2

Table 2: Position of Lagrange points in Earth-Moon system including normalized units referring to the Earth-Moon distance of 384,400 km [26].

2.1.3 Special Orbits

In the following, based on the properties of the libration points, four different orbits and their properties are shortly described [16; 27–29]. Basically, they can be classified by the motion in the different planes. Lyapunov orbits are periodic planar orbits, in which the spacecraft performs its motion only in the x-y plane of the primaries. Lyapunov orbits are only possible in CR3BP due to their two-dimensional motion. Lissajous orbits, on the other hand, are three-dimensional quasi-periodic orbits providing an oscillating motion normal to the orbital plane. Halo orbits also have a three-dimensional periodic pattern, named after the shape of the orbits as seen from Earth [27]. However, since halo orbits can only be calculated in CR3BP, quasi-halo orbits provide a solution between halo orbits and Lissajous orbits.

The accessible orbits, however, depend on the initial state of the spacecraft, which is shown schematically in Figure 4 for SEL_2. The optimization tool of Astos Solutions offers the possibility to calculate the transfer into different orbits based on different design parameters by propagating the initial state.

The different orbits allow a stationary, partly periodic movement around the respective Lagrange point, whereby lunar halo orbits have an essential role in future deep space exploration, especially for lunar exploration. Due to the high accessibility of the Moon from halo orbits around EML_1 and EML_2, these orbits were considered for an intersatellite link between Earth and the far side of the Moon [27], as gateway [30], and for the return mission of lunar samples [31].

In this context, the coverage potential of the lunar south pole [32] as well as concepts for lunar communication and navigation using a halo orbit around EML_2 were investigated [33]. Lagrange points not only allow access to scientific targets, but also allow efficient transfers between them using manifold transfers [34].

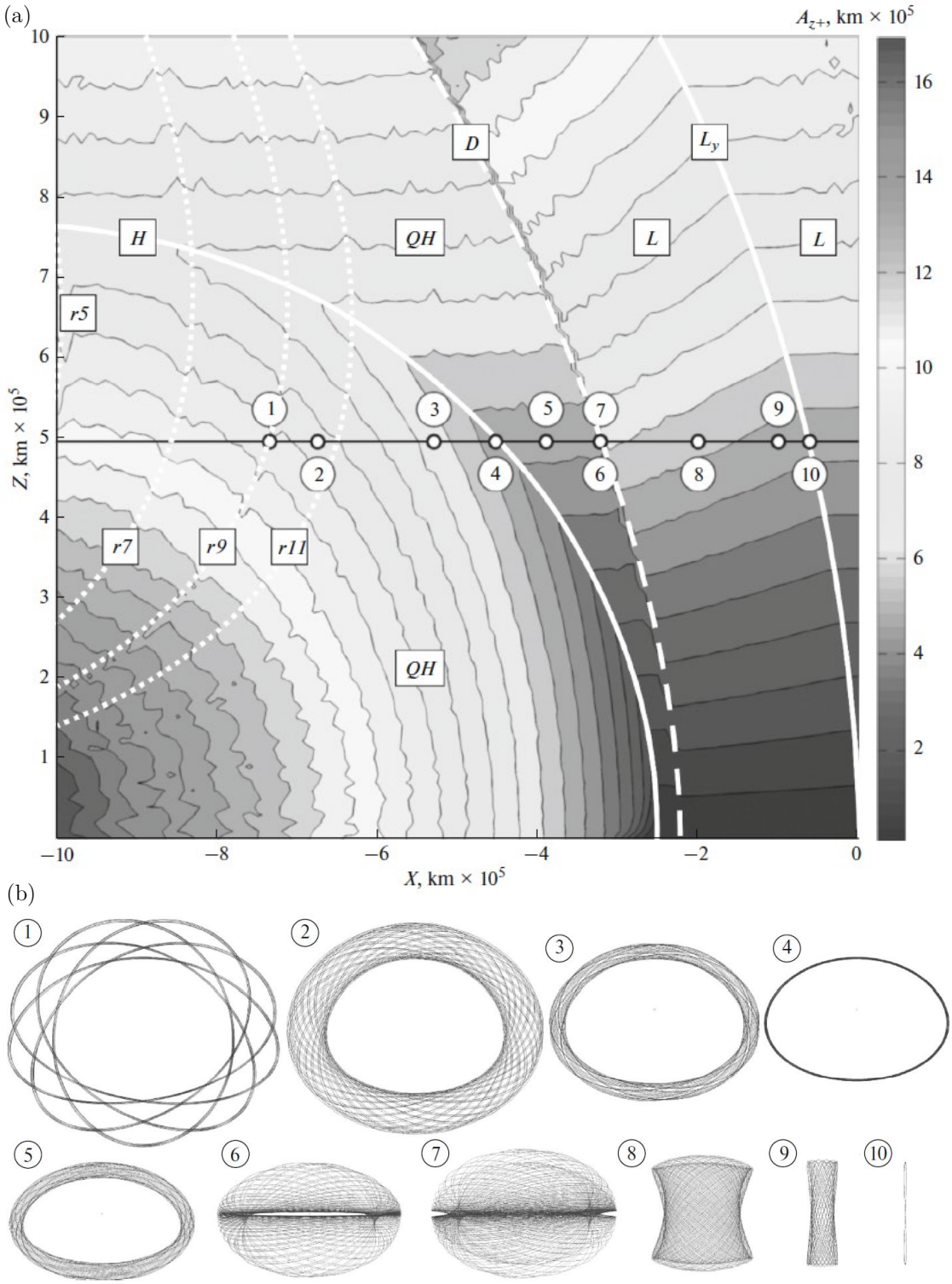

Figure 4: Visualization of different orbits around SEL_2 [25]. (a) Scheme illustrating the limited orbits around SEL_2 depending on the initial state: H is halo orbit; L_y is vertical Lyapunov orbit, L indicates Lissajous orbit, QH is quasi halo orbit, r5 – r11 are resonant orbits. (b) Projection of different orbits on y-z plane depending on initial state.

Due to the symmetry of the potential field of the CR3BP with respect to the x-y plane of the rotating frame, symmetric pairs of halo orbits result, which can be divided into southern and northern families. The classification is based on the maximum out-of-plane amplitude (A_z) in the respective hemisphere. A southern family halo orbit, with a maximum excursion in the -z direction, is largely in the southern hemisphere of the Moon, making them suitable for communication with the lunar south pole. On the other hand, a northern family halo orbit with an A_z in +z direction, allowing better coverage of the northern hemisphere [18]. Figure 5 illustrates the northern family of EML_1 halo orbits in comparison to the southern family of EML_2 halo orbits [35]. Another possibility to identify each member of a family is by the specific Jacobi integral C (Eq. 2).

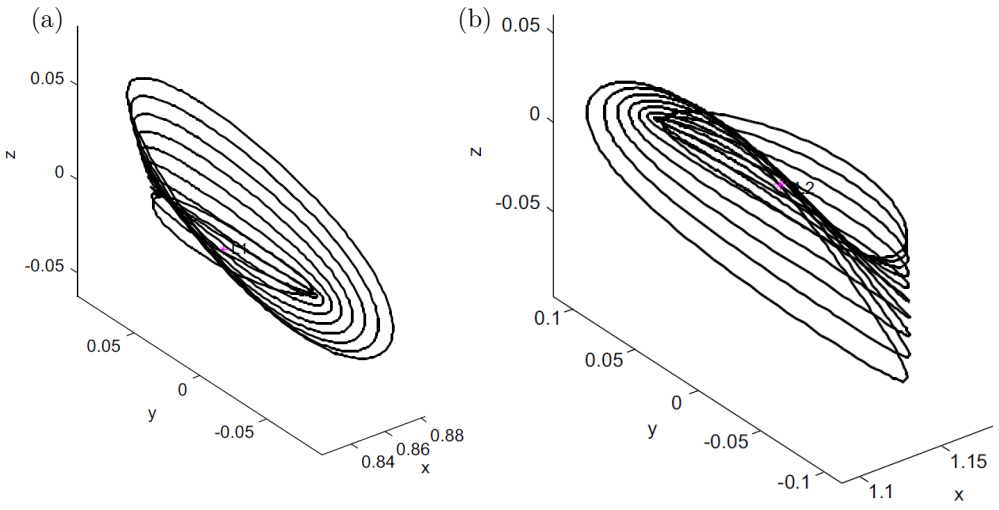

Figure 5: Visualization of halo orbit families [35]. (a) Northern family of EML_1 halo orbits. (b) Southern family of EML_2 halo orbits.

As a result of the instability of the orbits around the essential Lagrange points, a perturbation leads to an increasing drift away from the halo orbit. These asymptotic orbits exist for departing as well as for approaching unstable orbits around Lagrange points (Figure 6). The trajectories for asymptotic departures from the unstable orbit are called unstable invariant manifolds, and the trajectories for arrival at the unstable orbit are called stable invariant manifolds [35].

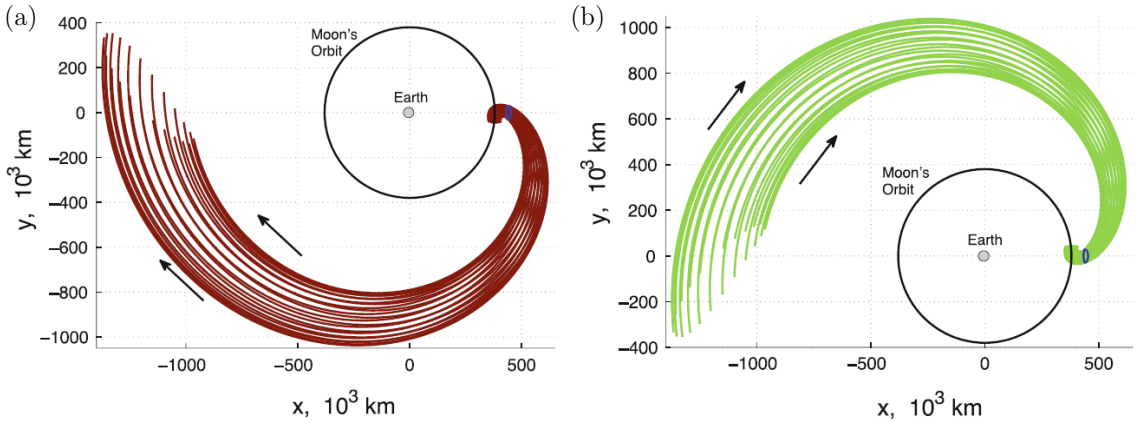

Figure 6: View of invariant manifolds of the EML2 halo orbits in the x-y plane [36]. (a) Unstable invariant manifolds for departs. (b) Stable invariant manifolds for arrival.

Near-Rectilinear Halo Orbits (NRHO) are a special subset of halo orbits in the vicinity of the collinear Lagrange points [37], which can be simulated in higher-fidelity models (Figure 7).

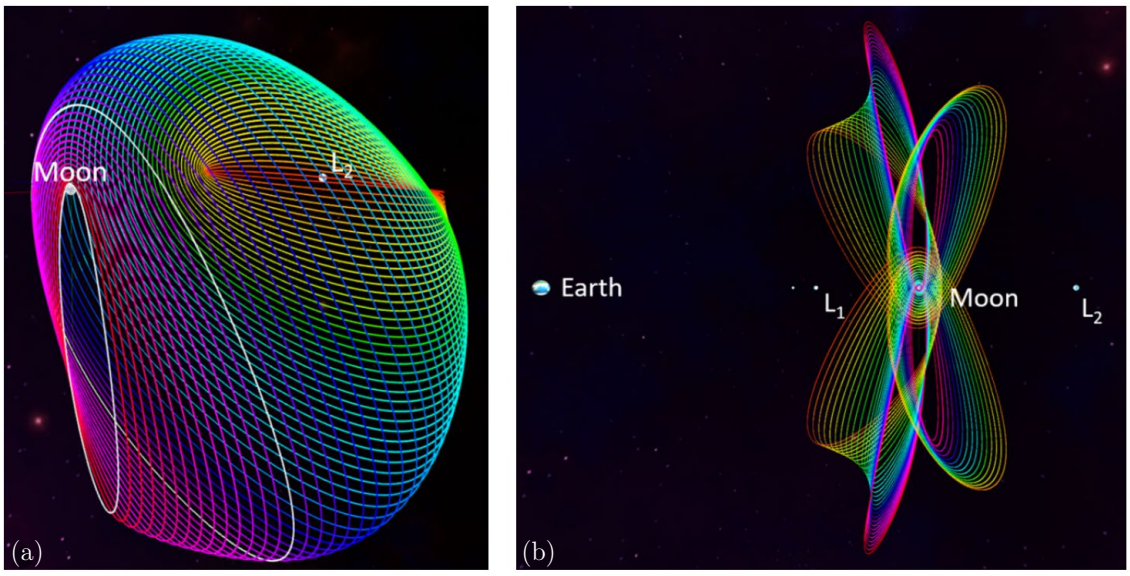

Figure 7: Halo orbits and NRHO in the vicinity of collinear Lagrange points [38]. (a) Southern halo family of EML_2. (b) Northern and Southern NRHOs of EML_1 and EML_2.

Therefore, NRHOs have been investigated for long-term missions as well as for manned missions to the Moon [25]. Due to their promising stability, NRHOs require only a small amount of propellant to maintain their orbit over a longer time period (4,5). In addition, NRHOs can be adapted to the mission scenario by choosing appropriate resonance properties to avoid eclipses [38; 39]. Due to their fuel-efficient stability as well as favorable access to the Moon, determined by their potentially short period, an NRHO is planned

for the Lunar Gateway [40]. The mapping in a high-fidelity model to demonstrate the capability for current missions requires an extension to the CR3BP [41]. The resulting nonlinear and sensitive dynamics as well as the simulative mapping of station-keeping strategies imply new challenges to identify energy-efficient solutions [38].

NRHOs can be characterized by their stability index ν, which is a function of the maximum eigenvalues λ_{max} of the state transition matrix (STM) after one period of the halo orbit. The stability index is defined as

$$\nu = \frac{1}{2} \left(\lambda_{max} + \frac{1}{\lambda_{max}}\right) \qquad \text{(Eq. 3)}$$

whereby a target stability index of one indicates a stable halo orbit. A stability index greater than one implies that perturbations will result in a drift from the intended orbit, therefore NRHOs are often defined by a ν lower than 1.5. The analysis of the stability behavior as a function of the perilune radius (Figure 8) illustrates the possible halo orbits and their stability. The linear analysis clearly shows that for large perilune distances (r_p), the stability index increases, resulting in rising instability. This region contains nearly planar halo orbits. At the same time, a decrease of r_p results first in a region with stability index one and then in a region with a slightly increased but sufficient stability index. The choice of a suitable halo orbit for the cargo hub at EML_2 (Chapter 4.2) is analyzed on the basis of the stability index ν in connection with the perilune distance r_p.

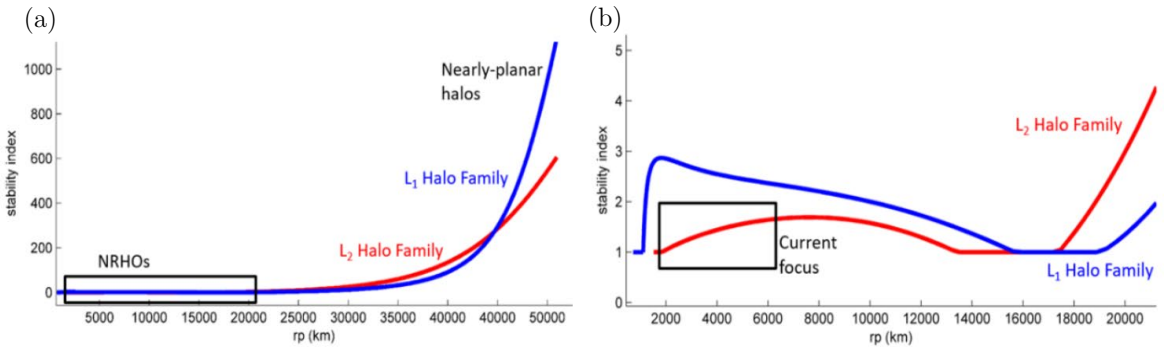

Figure 8: Stability indices of halo orbits around EML_1 and EML_2. (a) Stability indices for a perilune range of $r_p = 0$ km to $r_p = 50000$ km. (b) Stability indices for a perilune range of $r_p = 0$ km to $r_p = 20000$ km.

2.2 Solar Radiation Management (SRM) Methods

The field of geoengineering covers various technologies and methods for counteracting climate change with the support of technical interventions. Solar radiation management (SRM) methods provide special strategies for modifying Earth's radiation balance to reduce the increasing temperature. The reduction of the solar radiation exposure can be performed either directly on Earth's surface, in the atmosphere, in orbit, or in outer space (Figure 9). In the following, the different SRM methods are described shortly, and their advantages and disadvantages are discussed.

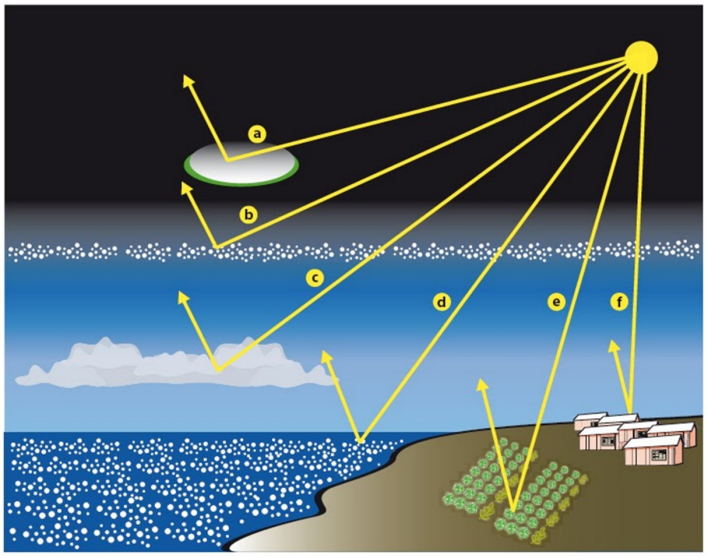

Figure 9: Solar radiation management methods [42].

2.2.1 Earth-based SRM

An Earth-based solution is to increase the reflectivity of Earth's surface [43]. One possibility is to increase the reflectivity of agricultural areas by cultivating highly reflective crops [44]. In addition, the reflectivity of urban roofs and large-scale artificial surfaces can be increased by applying reflective materials [45]. The Earth is mainly covered by water, accounting for 71% of its surface [46], thus an increase in oceanic albedo can be achieved using large solar reflectors [47]. In addition, by deploying seawater particles using the Marine Cloud Brightening (MCB) method, the cloud droplet number concentration can be increased and artificial clouds can be seeded over the oceans to increase atmospheric reflectivity [48; 49]. Inspired by the natural impact of volcanic eruptions on

atmospheric albedo, the Stratospheric Aerosol Injection (SAI) using sulphate aerosols in the low stratosphere provides another way to scatter incoming sunlight back to space [50; 51].

Based on the demand of large-scale environmental impact on Earth's surface, as well as in Earth's atmosphere, taking regional influences and efficiencies into account, Earth-based SRM are discussed controversially [4; 43; 52]. Non-uniform, local modification of surface albedo provides only partial relief [53]. Changing the atmospheric albedo using SAI is currently described as the most cost-efficient method [4; 54; 55], although continuous injection of aerosols is required to maintain long-term control of temperature warming [54].

2.2.2 Space-based SRM

Space-based methods, on the other hand, offer the possibility of diverting the incoming solar radiation before reaching Earth. A distinction can be made between solutions in Earth orbit and at stationary points such as SEL_1. An artificial Earth ring of light scattering particles [56; 57] as well as large dust clouds [58] of materials from Earth, Moon, or asteroids could provide a long-term solution, but would increase the collision hazard in Earth orbits due to their uncontrollability. In contrast, large, assembled structures called sunshades [59], which could be positioned at SEL_1, are able to provide a controllable solution despite their engineering complexity. In addition, these can be designed for uniform global shading [60]. However, the high costs as well as the required technological developments of this promising technology are a major challenge. Compared to the Earth-based SRM methods, these technologies do not directly interfere with the Earth's atmosphere and thus do not affect the atmospheric balance with respect to the particle budget [4]. By purely reducing the global solar radiation flux to a certain amount, space-based solutions represent a controllable and, if necessary, reversible method to achieve the targeted reduction of radiation. The cooling effect based on the change in radiative forcing [61] can be as effective as SAI methods. Thus, the technology must be analyzed in terms of technological and scientific showstoppers.

2.3 Constellation Types

Space-based solar radiation management methods are suitable for controlled and uniform shading. In the following, different approaches for a shading system around the SEL_1 are presented, which are used as a baseline for the IPSS concept. A detailed discussion with respect to the sunshade design as well as a first mass estimation for lunar materials was performed in the parallel thesis [13].

2.3.1 Large Sunshade

The basic idea of counteracting the global warming by space-based sunshades already emerged at the end of the 20^{th} century and was discussed in the works of Early [62] and Seifritz [63] with regard to the application of reflective materials. Stability aspects with respect to the balance between the absorbed and emitted thermal energy, as well as the effects of the Solar Radiation Pressure (SRP) were already described. Due to the pure solar radiation effect, first calculations regarding the positioning of a sunshade between Sun and Earth have been discussed. The first mass estimation in the order of 10^{11} kg to reduce the solar irradiance by 1.7% to achieve a reduction of 2 K illustrates the technological challenges involved. To reduce the high mass requirement for positioning at SEL_1, artificial Lagrange points L_A were investigated using SRP. Shifting the stationary point to a distance of $2.36x10^6$ kilometer (km) from Earth allows minimizing the mass to 240 million tons (t), which can be optimized by reduced solar radiation coefficients [64]. Thus, the solar radiation coefficient is a key parameter, which is depending on the material. The resulting mass estimations are a central topic of several sunshade concepts and were also discussed in the parallel work [13]. Due to the high mass requirement, the use of lunar resources [13] or iron and carbon materials from asteroids [65] was discussed and the impact on the sunshade design was analyzed. Asteroids offer the possibility of carbon-based coatings to reduce sunshade mass by lowering the reflectivity. The utilization of space resources poses new technological challenges for processing, manufacturing, and energy supply. In this context, solar reflectors for harvesting solar energy have been described to enable the processing of asteroids [66].

The global climate impact is the key advantage of space-based sunshades compared to Earth-based SRM methods. The simulation of the global climate impact requires sufficient modeling of the sunshade as well as the effects of orbital motion on the global shading impact [60]. The integration of the Globally Resolved Energy Balance (GREB) model illustrated the local temperature variation using a single stationary sunshade. The non-uniform shading leads to a higher temperature reduction in the equatorial region than in the polar regions, which could cause secondary climatic effects. To obtain a uniform reduction of temperature, a vertical oscillation of the sunshade around the Sun-Earth line was simulated (Figure 10). Adapting the period of the oscillating orbit by means of an active SRP control allows an adjustment to the rotation of the Earth around the Sun. The enforced periodic motion indicates an improvement of the local mean temperature, although a global loss of 0.4% of solar radiation blocking by the displacement has to be accepted. Consequently, a loss of a small amount of shading enables a more uniform temperature reduction to be obtained.

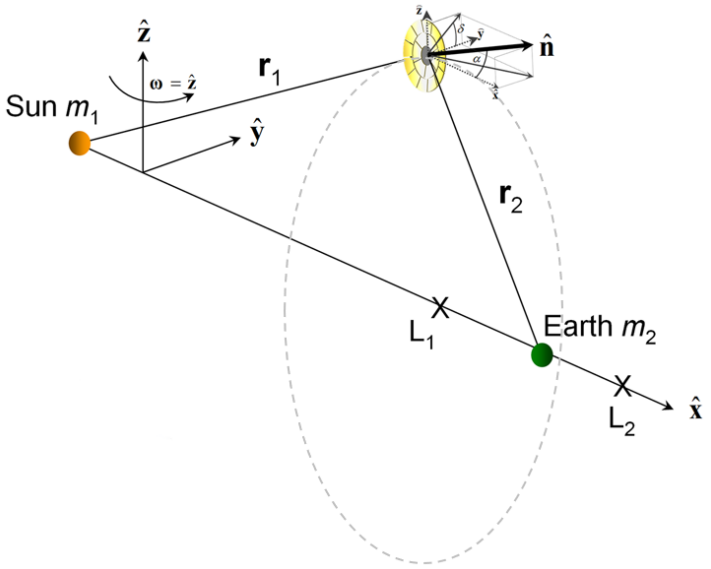

Figure 10: Occulting disk near the SEL_1 [60].

In order to achieve an optimization with respect to a homogeneous mean temperature, the concept was extended to two oscillating sunshades and optimized by numerical methods. First, the same total shading area was simulated, and the climatic impact was optimized by varying the sunshade size, period, out-of-plane displacement, and orbit control. The simulation resulted in two phase-synchronized oscillating sunshades with a radius of 1,200 km and 790 km, returning up to 40% of the Earth's surface to pre-global warming temperatures.

An extended optimization could be achieved by the additional variation of the shading area. In this context, the numerical optimization reveals that a halving of the residual increase of temperatures is possible by deploying two sunshades with radii of 1,522 km and 880 km in a phase-shifted configuration. Assuming the environmental damage is quadratically dependent on the temperature increase, the impact of global warming could be reduced by 75% [60].

2.3.2 Swarm of Autonomous Sunshades

The size and complexity of large sunshades present major challenges to the conceptional design. A reduced level of required technological advancement can be achieved through the utilization of small sunshades, known as flyers [67]. An autonomous formation of trillions of flyers around SEL_1 manufactured on Earth is proposed. Although the technical effort of constructing large sunshade structures is significantly reduced, the effort to control the large cloud of autonomous spacecraft in terms of self-shadowing, collision avoidance, as well as configuration stabilization increases. The application of electromagnetic launchers enables an emission-free launch technology, but due to the gravitational potential of Earth high amounts of energy are demanded. The concept envisages small sunshades with a diameter of 1 meter (m), produced with a special hole pattern on Earth to achieve a refractive effect in terms of on the solar radiation. Due to an Earth-based lightweight design, the overall system provides the lowest mass for a sunshade concept of only $2x10^7$ t, which will be delivered to SEL_1 by 20 million electromagnetic launches with a respective payload of 1 t.

However, the number of necessary launches and the associated demands on infrastructure and energy supply provide new technical challenges, so the utilization of space resources [66] can provide potential for the application of a modified concept. A more advanced concept of the sunshade as a solar power satellite [68] to provide space-based clean energy [69] could generate new synergies and contribute to an amortization of the overall system [70]. Based on these promising aspects, an international sunshade concept is presented in the following with an explicit discussion of the logistical aspects for implementation.

3 Definition of IPSS Mission Scenario

The following chapter presents the roadmap developed for the mission scenario of an IPSS system. The roadmap was developed in collaboration with a parallel thesis on ISRU and ISM [13], whereby the following chapters focus especially on the logistical aspects. Based on the conceptual design of the IPSS system, the logistical requirements are derived and a concept for the logistical design is presented.

3.1 Overall Roadmap

Based on the analyzed constellation types (Chapter 2.3), the roadmap for the IPSS system was developed, providing reasonable synergies between the IPSS system and existing efforts by the international space agencies. To enable further settlement and human-based exploration of the solar system, the ISECG Global Exploration Roadmap presents various scenarios [71; 72]. In this context, EML_1 and EML_2 play a decisive role as initial points for the next generation of space stations beyond Low Earth Orbit (LEO). The first estimations of the sunshade mass [13], positioned at the vicinity of SEL_1, clarify that an IPSS system can only be achieved by exploiting space resources. In combination with the current projects of a Lunar Gateway [40] as well as the potential resources for a sunshade [13], the Moon is considered as a promising material source for the sunshade production. In addition, current ISM methods and their potential application for the raw material extraction process on the Moon were analyzed [13].

To establish a feasible IPSS system concept, possible technological spin-ins were investigated to enable efficient developments as well as optimal exploitation of resources. At the same time, possible technological spin-offs were identified in order to achieve continuous benefits, to create synergies with ongoing projects, and to enable continuous adaption of the system to the current state of the art. Figure 11 shows the four phases of the current roadmap (Appendix A), which are the focus of further investigation.

	Phase1 Technology Development	Phase 2 Technology Demonstration	Phase 3 Sunshade Production	Phase 4 Sunshade Operation
Timeframe	2021 - 2040	2035 - 2045	2050 - 2070	**2060** - 20xx
Location	**Earth** (EML_2, SEL_1)	**EML_2, Lunar Surface** (SEL_1)	**SEL_1, EML_2**	**SEL_1**
Objectives	Development of mission critical technologies, Earth-built demonstrators	Demonstration of lunar production and mass transportation capabilities	Demonstration of sunshade production capabilities at SEL_1, bootstrapping of sunshade production	Shade operation, formation setup, climate monitoring and optimization of climate impact

Figure 11: Mission phases for IPSS system development.

In **phase 1**, the focus is on the development of required technologies for lunar exploration as well as individual components for a small Earth-built sunshade. The lunar technologies can be divided into the technologies for the material extraction and processing, as well as the transport within the Earth-Moon-EML_2-SEL_1 system. Efficient technologies for the generation, conversion, and storage of the required energy have to be developed in order to provide a sufficient energy supply for the electromagnetic launcher as well as for the energy consumption of ISRU processes. Furthermore, the components for a lightweight design of the Earth-built sunshade have to be designed and tested in Earth orbit followed by a final demonstration of the functionalities at SEL_1. The development can benefit from the existing know-how and technologies of missions like SOHO.

Phase 2 focuses on the technological demonstration of the lunar production processes and the development of high transport capacities using electromagnetic launchers. The focus is on setting up a cargo hub at EML_2 in order to first stock the raw material temporarily for the sunshade and then transport it to SEL_1.

In **phase 3**, the mass production of sunshades will be initiated with the construction of the large-scale production facilities. Through the logistical network established in phase 2, the required raw materials will be delivered just-in-sequence and processed to sunshades using the high solar energy available, generated by solar power satellites. The produced sunshades can in turn be used as photovoltaic sunshades [13] for further energy generation to drive the bootstrapping production process. Continuous development of

the sunshades based on new technological advances is essential for the constant improvement of the efficiency and the lightweight potential of the sunshades. In addition, the sunshade design must be specified and further developed with regard to energy-efficient stabilization and collision avoidance.

Phase 4 includes the primary operation as well as the adjustment of the overall constellation to achieve an efficient climate impact. In this context, climate monitoring is an essential objective in order to observe possible effects of the radiation reduction on the weather pattern. Due to the large constellation setup, the focus is on ensuring continuous collision avoidance in order to prevent the IPSS system being affected by malfunctions. However, a certain failure rate must be assumed, defining the basis for maintenance and service activities. Thus, after completing the IPSS sunshade formation, the production site at SEL_1 will remain for the production of spare parts as well as backup sunshades. In addition, secondary uses of the facility can then be initiated to exploit SEL_1 as a starting point for future space missions and as an expanded target for manned missions. The station can be used as human outpost, utilizing the high level of energy provided.

In order to provide the baseline for the visionary endeavor, the following chapters will describe the logistical aspects regarding launches within the Sun-Earth-Moon system focusing on the transfers in the Earth-Moon system and operation of the sunshades at SEL_1.

3.2 Logistical Concept

Initial estimations for the high mass requirements of the sunshades for the IPSS system, as well as the associated masses for production facilities, represent a major challenge. Based on the proposed sunshade designs, the orders of magnitude for the mass transport in the respective phases can be estimated (Table 3).

In dependence of the different orders of magnitude of required resources as well as the selected transfers, the derived requirements for the logistics result, enabling different transfer technologies for the respective phase.

Characteristics	Phase 1	Phase 2	Phase 3	Phase 4
Estimated payload range	~ 50 t	~ 100 kt	~ 500 Mt	~ 1kt
Transfers	E - SSO E - LS E - SEL_1	E - LS E - EML_2 LS - EML_2	E - SEL_1 LS - EML_2 EML_2 - SEL_1	LS - EML_2 E - SEL_1 EML_2 - SEL_1
Technologies	**RR**	**LC**, RR	**LC**, **SS/LBS**, RR	(LC, SS/LBS, RR)
In-space refueling	not planned	planned	not planned	planned

Table 3: Characteristics of transfers in the different phases. Transfer locations are differentiated between Earth (E), Sun-synchronous orbit (SSO), lunar surface (LS), Sun-Earth Lagrange Point 1 (SEL_1), Earth-Moon Lagrange Point 2 (EML_2). The transfer technologies are differentiated between reusable rockets (RR), lunar coilgun (LC) and solar sailing (SS)/laser-based sailing (LBS).

Phase 1 requires a low logistical effort, as the main focus is on the development of the relevant technologies. The transported masses include technological demonstrators, which are estimated to have a total mass of less than 50 t. Thus, the transportation using conventional rockets is sufficient. The considered transfers include the first technological component tests in a Sun-synchronous orbit (SSO), the first demonstrators for the material extraction and processing facilities on the lunar surface, as well as the final Earth-built sunshade demonstrator, which will be sent to SEL_1.

In phase 2, the transport mass increases significantly due to the construction process of the lunar coilgun (LC) system as well as the facilities for ISRU, construction facilities, and energy infrastructure to a maximum of 100 kt. The main transfer is between Earth and the lunar south pole region where the lunar base is constructed. Another minor mass contribution occurs from resources sent from Earth to EML_2 to establish the EML_2 cargo hub infrastructure in parallel with the lunar coilgun construction process. The largest mass fraction is covered by the launch of the first cargo blocks to the EML_2 cargo hub. Thus, the lunar coilgun is the key transfer technology in the second phase.

Phase 3 is the most substantial phase with an estimated mass in the order of 500 Mt, as the bootstrapping process of sunshade production at SEL_1 is scheduled. To initialize the bootstrapping process, the preliminary production equipment and energy infrastructure must be transported from Earth to SEL_1. In addition, sophisticated Earth-based components for the sunshade must also be provided. However, the largest mass fraction, the raw material mass, is transported to EML_2 by the coilgun and bundled at the cargo

hub. Further, an energy-efficient transfer from the cargo hub to the SEL_1 is performed utilizing low-thrust propulsion technologies. Solar sail-based propulsion concepts as well as laser-beam sailing are promising propellant-less transfer technologies to establish a continuous just-in-sequence process at SEL_1.

In Phase 4, the required mass transfer will be reduced significantly once the necessary raw material mass has been transported to SEL_1. However, a continuous supply of lunar and terrestrial resources in the order of 1 kt will remain in order to perform service and maintenance as well as to provide backup sunshades in case of potential failures. For the mass transportation, the already established logistical network in the Sun-Earth-Moon system will be used.

In the following chapter, the characteristics of the different logistical phases will be examined in terms of the required trajectories.

4 IPSS Trajectory Design

The following chapter gives an overview of the planned trajectories (Figure 12) focusing on the transfer between Earth and EML_2 using various tools to analyze possible orbits. Finally, an overview of transfer trajectories with respect to ΔV-demand is presented.

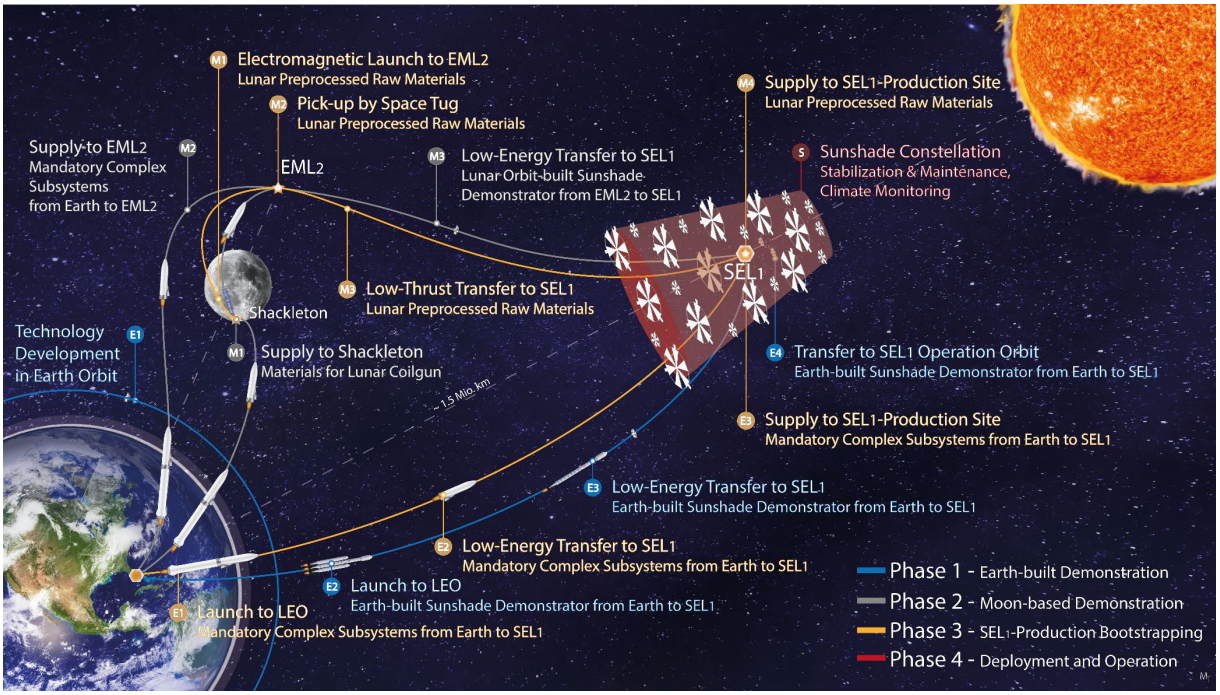

4.1 Earth-based Trajectories

Based on the current launcher technology (Chapter 5.1) as well as the upcoming future international developments, there are various possibilities for the transfer of the Earth-built demonstrator as well as the demonstrator technologies into Earth orbit, to the lunar surface, and to SEL_1.

Technology proof in the first phase is the essential foundation for the success of the IPSS system, which is why a fast-progressing development is crucial. The verification of necessary ISRU as well as ISM processes under space conditions can be conducted, for example, already on Earth in simulated lunar testbeds [73] or in combination with already planned missions such as the On-orbit Servicing, Assembly, and Manufacturing (OSAM) satellites [74], to demonstrate robotic manufacturing and assembly in space.

The transfer trajectories in the first phase do not pose a challenge to the current state of the art. The use of the AOCS of the IPSS system can be tested in a polar SSO (Figure 13) in order to provide a constant orientation to the Sun, as it is the case at SEL_1. Due to the low masses of the demonstrators, an international distribution and coordinated development is possible by combining international launcher capabilities (Chapter 5.1) in order to identify fast and efficient solutions.

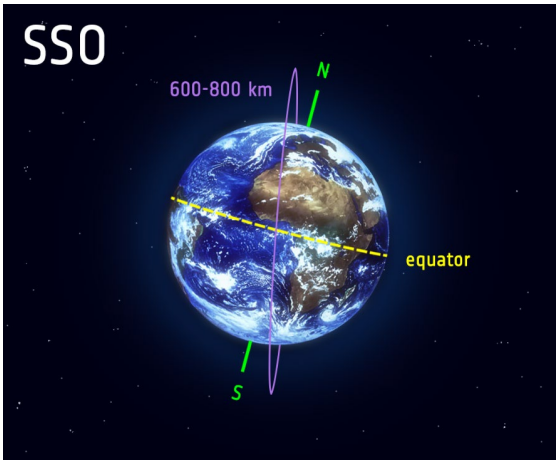

Figure 13: Trajectory of polar SSO [75].

With regard to the lunar missions, the diverse experience of lunar exploration missions can be utilized, and by taking advantage of synergy effects with planned missions Package for Resource Observation and in-Situ Prospecting for Exploration, Commercial Exploitation and Transportation (PROSPECT) of the European Space Agency (ESA) [76], the methods developed in the testbeds can be verified.

For the transfer trajectory of the first sunshade demonstrator, the already designed transfer trajectories of missions like SOHO (Figure 14), ACE and WIND can be used to investigate the possible orbits with respect to their suitability for a purely solar sail based AOCS (Figure 15).

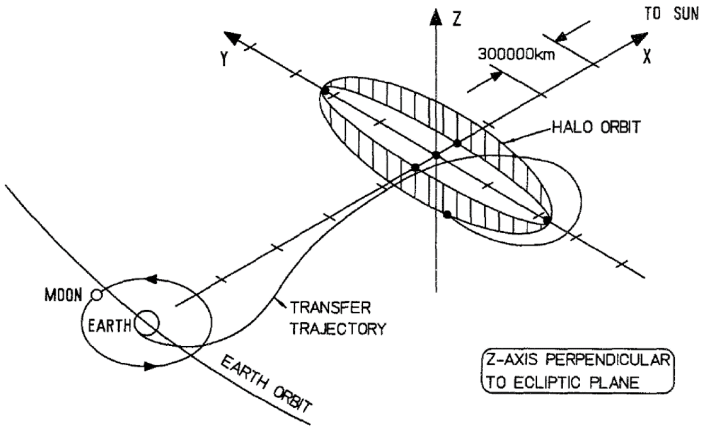

Figure 14: Overview of SOHO transfer trajectory and halo orbit [19].

The choice of the final orbit around SEL_1 has to be adapted with respect to stability and the balance between required and feasible ΔV-demand with solar sails. Due to the complexity of the transfer trajectories into a stable orbit around SEL_1, a more detailed design of the trajectory is planned for the future with the extended optimization tool of Astos Solutions [77].

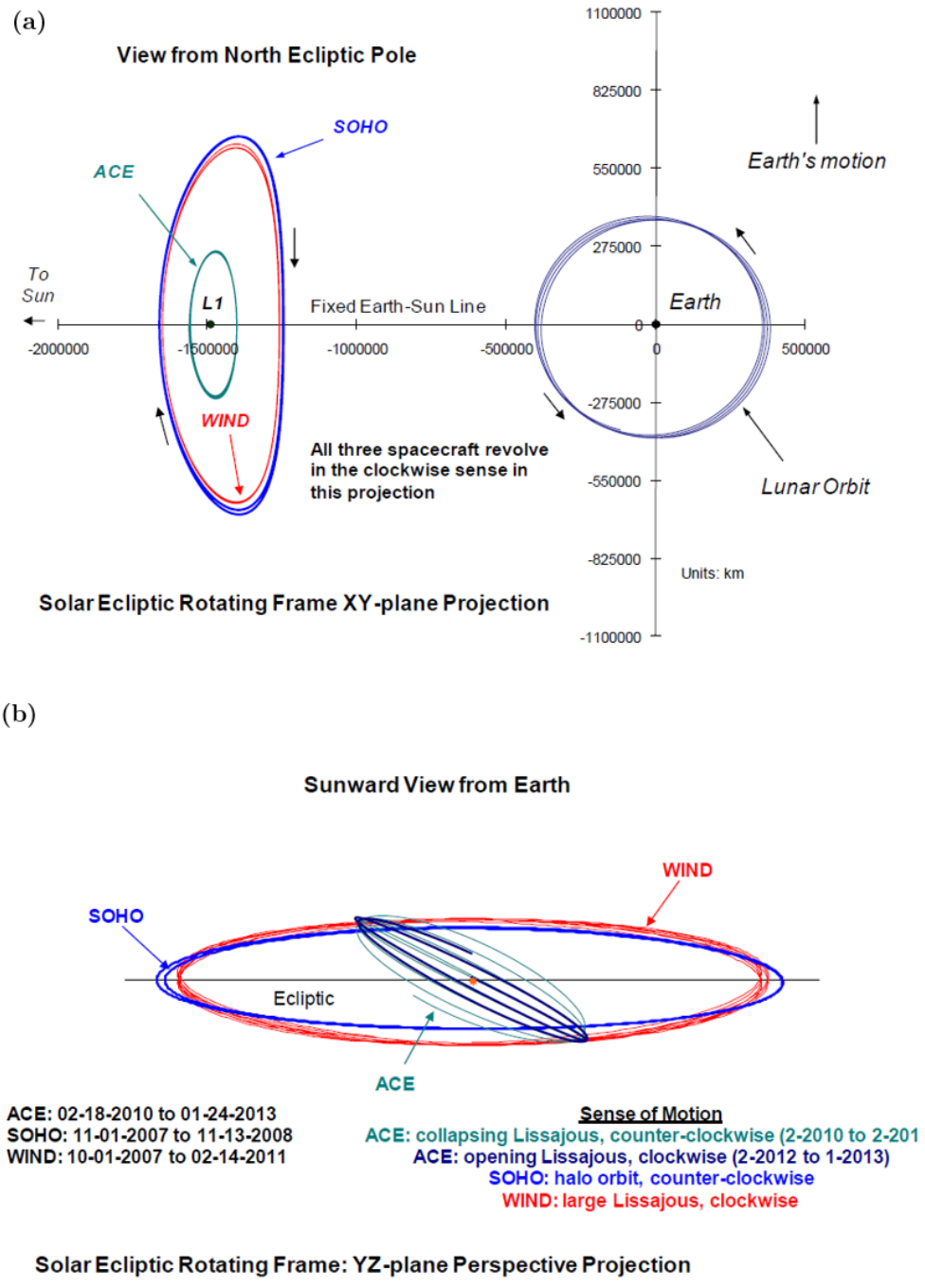

Figure 15: Overview of ACE, SOHO, WIND Lagrange point orbits. (a) View of motion in x-y-plane. (b) View of motion in y-z-plane [20].

4.2 Moon-based Trajectories

The first phase will focus on the transfer of the production facilities and required materials to deploy a production demonstrator around EML_2. Based on the launcher evaluation (Chapter 5.1.2) the reusable rockets Falcon Heavy and Starship are able to provide about 21.5 t (Appendix C) and up to 100 t payload for a Trans Lunar Injection (TLI), including multiple refueling operations in orbit for Starship to deliver the maximum payload to the lunar surface [78; 79]. Based on their high complexity and the limited possibilities to produce the complete launchers on the Moon, the reusability by refueling with lunar propellant will enable the first logistics to EML_2. In the second stage, high logistical efforts will be expended to construct a launch technology for high masses at the lunar south pole - the massdriver. The construction of the massdriver, based on the concept of a coilgun, will enable the transfer of raw materials to EML_2 serving as a transfer hub for material transportation to SEL_1 after the demonstrator phase at EML_2.

The logistical effort in the lunar phase is a decisive showstopper due to the transport of the components from Earth and high masses of raw materials from the lunar base to EML_2. Thus, in the following, the focus is on the development of a cargo hub at EML_2 by providing an efficient supply of resources. The energy-efficient transport of the raw material blocks from the lunar surface is performed by the lunar coilgun. The low-thrust transfer has to be investigated in future works. However, an efficient supply of the cargo hub with terrestrial components is mandatory in order to avoid inhibiting the bootstrapping process at SEL_1. Thus, the Earth-based trajectories to EML_2 as well as the communication windows with the lunar base at the south pole are highlighted in the following.

In order to deliver the maximum payload to EML_2 using refueling, the payload will be transferred from LEO via a Geostationary Transfer Orbit (GTO) utilizing a manifold transfer to EML_2. In order to utilize EML_2 as a hub, the transfers from a geostationary orbit (GEO) to different halo orbits around EML_2 were further analyzed. For this purpose, an optimization tool [77], provided by Astos Solutions, was used to design the transfer optimized in terms of time of flight (TOF) or ΔV as required. The tool allows to calculate a Pareto front for direct and manifold transfers based on the initial state of the parking and destination orbits. The Mixed Integer Distributed Ant Colony Optimization (MIDACO) global search optimizer [80] enables optimal solutions in a user defined

range, whereby the range of two to sixty days is selected for the optimization tool. The initial state can be defined by coordinates, Keplerian elements or predicted parameters, as it is necessary for Lyapunov orbits and halo orbits. The current version of the tool does not yet allow reliable results starting from a LEO or a GTO, but future enhancements will enable such simulations. The selected orbits were evaluated in terms of stability and visibility to the lunar south pole region in the latitudinal range of -89.5 to -90° to allow communication to the lunar base in the Shackleton crater area during electromagnetic launches, as well as to keep the stabilization effort low.

In the literature, halo orbits are classified based on different design parameters (Chapter 2.1.3). In this context, A_z, the maximum out-of-plane amplitude in the $+z$ direction of the considered halo orbit, is often used as a reference parameter. The first selected halo orbit has a low A_z of 5000 km, since a minimum A_z of 3100 km should be provided for communication with Earth [81]. In addition, reference sources are available for A_z of 5000 km to allow a more profound evaluation of the preliminary results [17; 35]. Another selection criteria is the low ΔV-demand for planar halo orbits with low A_z [29]. Based on the first simulation results (Figure 16), two scenarios are considered for further design.

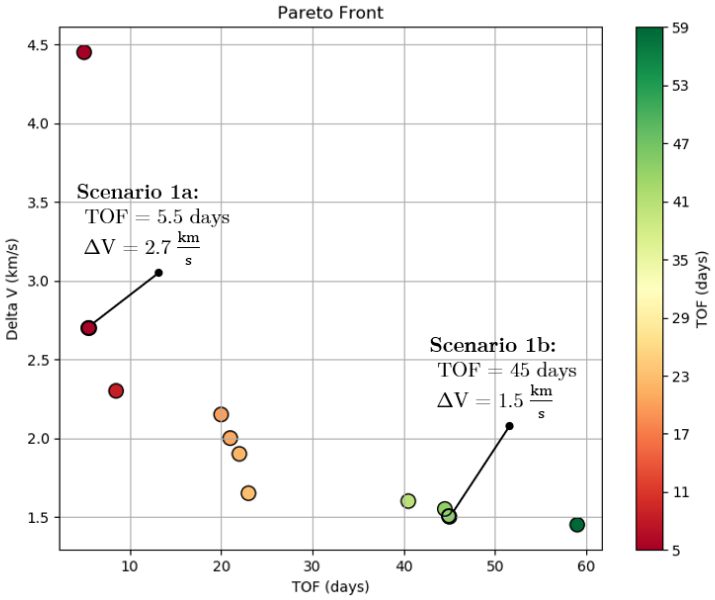

Figure 16: Pareto front for transfer from GEO to halo orbit around EML_2. Scenario 1a: *TOF* of 5.5 days and ΔV-demand of 2.7 $\frac{km}{s}$. Scenario 1b: *TOF* of 45 days and ΔV-demand of 1.5 $\frac{km}{s}$.

For manned missions, time-efficient transfer with a *TOF* of 5.5 days and a ΔV-demand of 2.7 $\frac{km}{s}$ is used for calculations. For cargo transport, an energy-efficient transfer with a *TOF* of 45 days and a ΔV-demand of 1.5 $\frac{km}{s}$ is proposed.

The verification with literature indicates that the ΔV-demand of the long-term transfer is around the expected value of 1.47 $\frac{\text{km}}{\text{s}}$ [82]. Table 4 lists the simulation parameters and Figure 17 and Figure 18 illustrate the calculated trajectories for the short-term (Figure 17) and long-term transfer (Figure 18).

EML-2 Orbit: HO with constant A_z = 5,000 km			
Orbit Type	Planar Halo Orbit $A_{z,norm}$ = 0.015527		
Family	Southern		
X	1.18067	V_x	0.00000
Y	0.00000	V_y	-0.15717
Z	-0.01515	V_z	0.00000
Period	14.91 days		
$R_{periapsis}$	50788 km		
Stability index	595.670		

Table 4: Initial state parameters of halo orbit with constant Az = 5000 km.

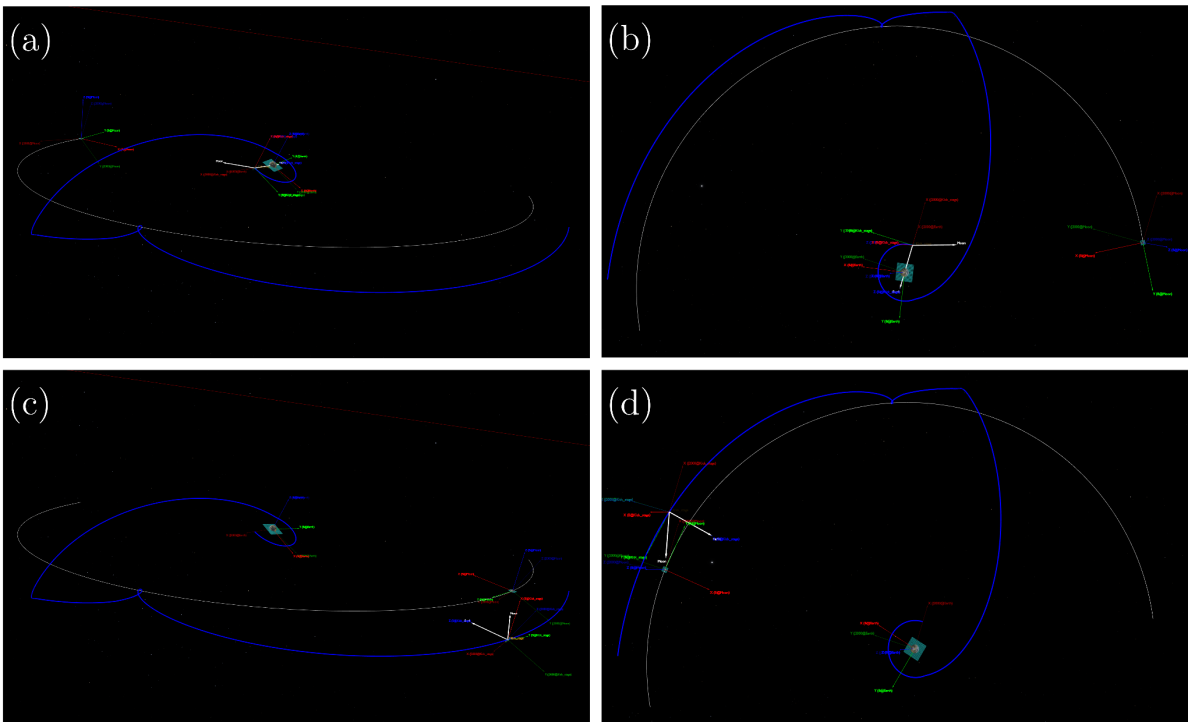

Figure 17: Short-term transfer trajectory (blue line) from GEO to halo orbit around EML_2 (Scenario 1a). (a) Angular view on parking orbit (t = 0.0 s). (b) Planar view on parking orbit (t = 0.0 s). (c) Angular view on destination orbit (t = 941,900.0 s). (d) Planar view on destination orbit (t = 941,900.0 s).

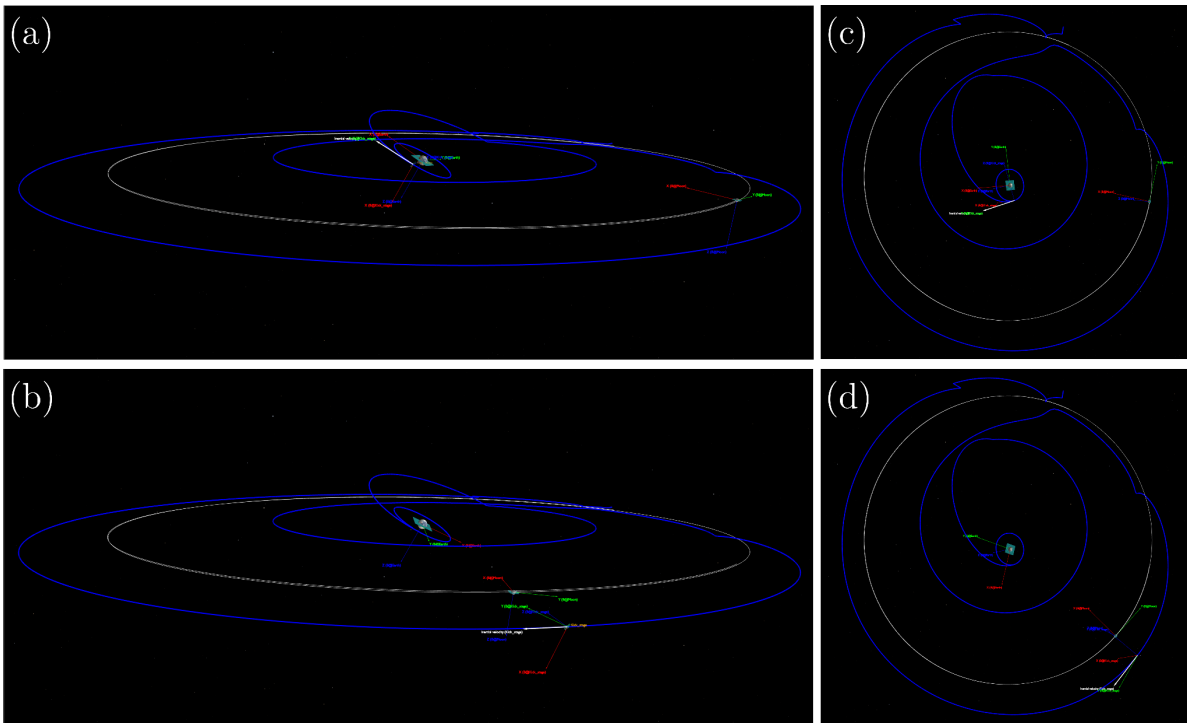

Figure 18: Long-term transfer trajectory (blue line) from GEO to halo orbit around EML_2 (Scenario 1b). (a) Angular view on parking orbit (t = 0.0 s). (b) Planar view on parking orbit (t = 0.0 s). (c) Angular view on destination orbit (t = 2,568,700.0 s). (d) Planar view on destination orbit (t = 2,568,700.0 s).

Furthermore, the communication window to the lunar south pole area was analyzed with the Lunar Surface Mission Analysis Tool (LSMAT) [83] over the period of 28 days to identify the contact capabilities to the Shackleton crater. Based on a discrete lunar terrain model derived from the data of the Lunar Reconnaissance Orbiter and the time-resolved trajectory data, LSMAT calculates the average visibility of spots in the lunar south pole region in the latitude range of -89.5 to -90°. The results indicate a maximum average coverage of only 44.55% over the simulation period based on the planar shape of the halo orbit. The analysis of the visibility data in the area of the Shackleton crater points out that there is only one potentially detectable spot with a visibility of more than 40% (Figure 19), whereby the majority of the crater is below a coverage of 20%.

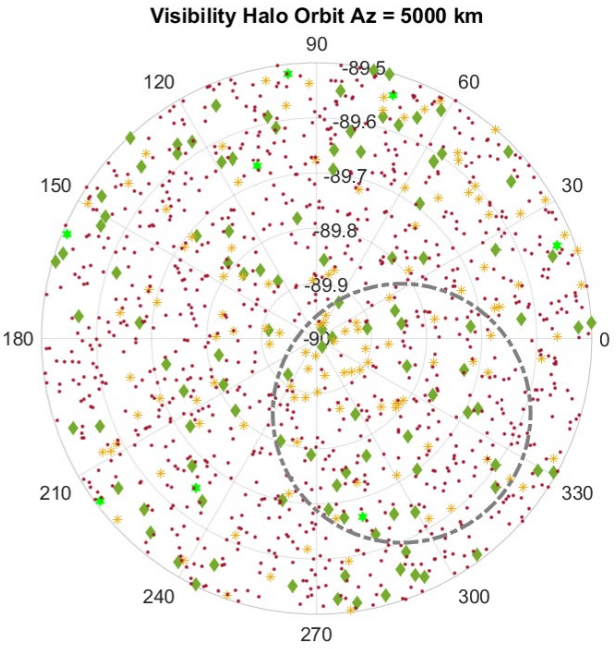

Figure 19: Communication coverage analysis for a halo orbit with A_z = 5000 km (calculated data based on LSMAT in the latitude range of -89.5 to -90°). Average coverage around the Shackleton crater area (grey dot line) differentiated between coverage above 40% (green star), 30 to 40% (green diamond), 20 to 30% (yellow cross), below 20% (red dot).

Due to the insufficient suitability of the halo orbit, the closest NRHO was included for further consideration. The closest NRHO, whose parameters can be found in Table 5, was also calculated using the optimization tool provided by Astos Solutions.

EML-2 Orbit: Closest NRHO			
Orbit Type	Near-Rectilinear Halo Orbit (NRHO)		
Family	Southern		
X	1.05940	V_x	0.00000
Y	0.00000	V_y	-0.17131
Z	-0.19933	V_z	0.00000
Period	8.87 days		
$R_{periapsis}$	11000 km		
Stability index	1.464		

Table 5: Initial state parameters of closest NRHO.

A subsequent analysis of the stability as well as the perilune distance exhibits a significant improvement in stability to a stability index of 1.46 and a perilune distance of 11,000 km. The Pareto front of the ΔV-demand over the TOF reveals that a short-term transfer with $TOF = 5.5$ days is feasible with a ΔV-demand of 2.68 $\frac{\text{km}}{\text{s}}$ (Figure 20).

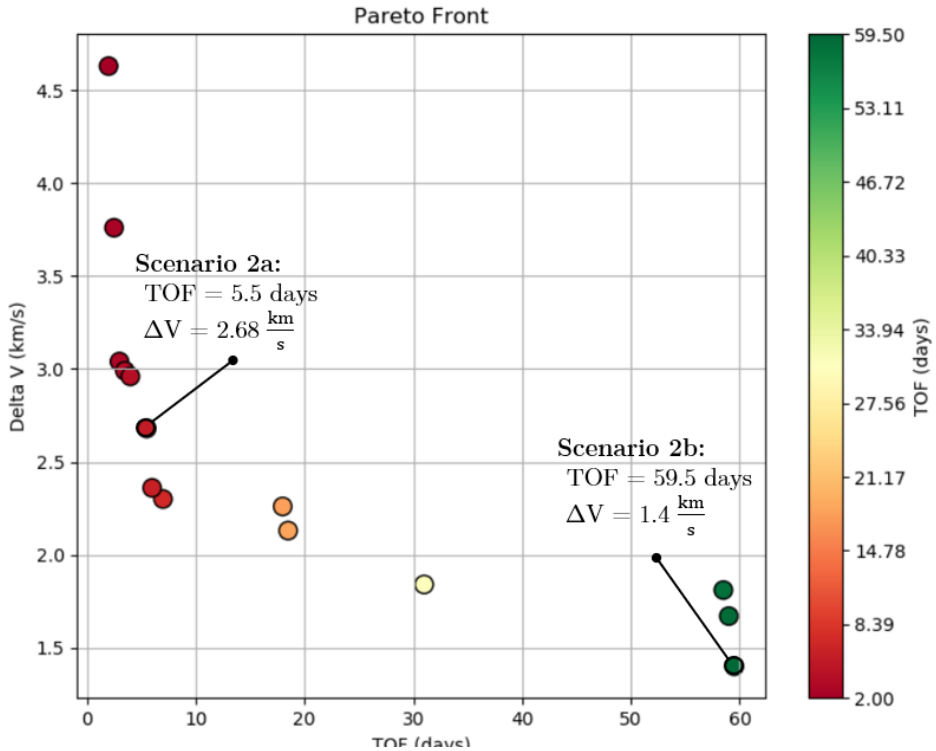

Figure 20: Pareto front for transfer from GEO to closest NRHO around EML_2. Scenario 2a: TOF of 5.5 days and ΔV-demand of 2.68 $\frac{\text{km}}{\text{s}}$. Scenario 2b: TOF of 59.5 days and ΔV-demand of 1.4 $\frac{\text{km}}{\text{s}}$.

The Pareto front does not represent a solution for $TOF = 45$ days, but this is related to the current development status of the optimization tool. The long-term transfers in the range of $TOF = 60$ days provide similar value ranges with a ΔV-demand of 1.4 $\frac{\text{km}}{\text{s}}$. The calculated trajectories for the short-term transfer (Scenario 2a) and the long-term transfer (Scenario 2b) are illustrated in Figure 21 and Figure 22.

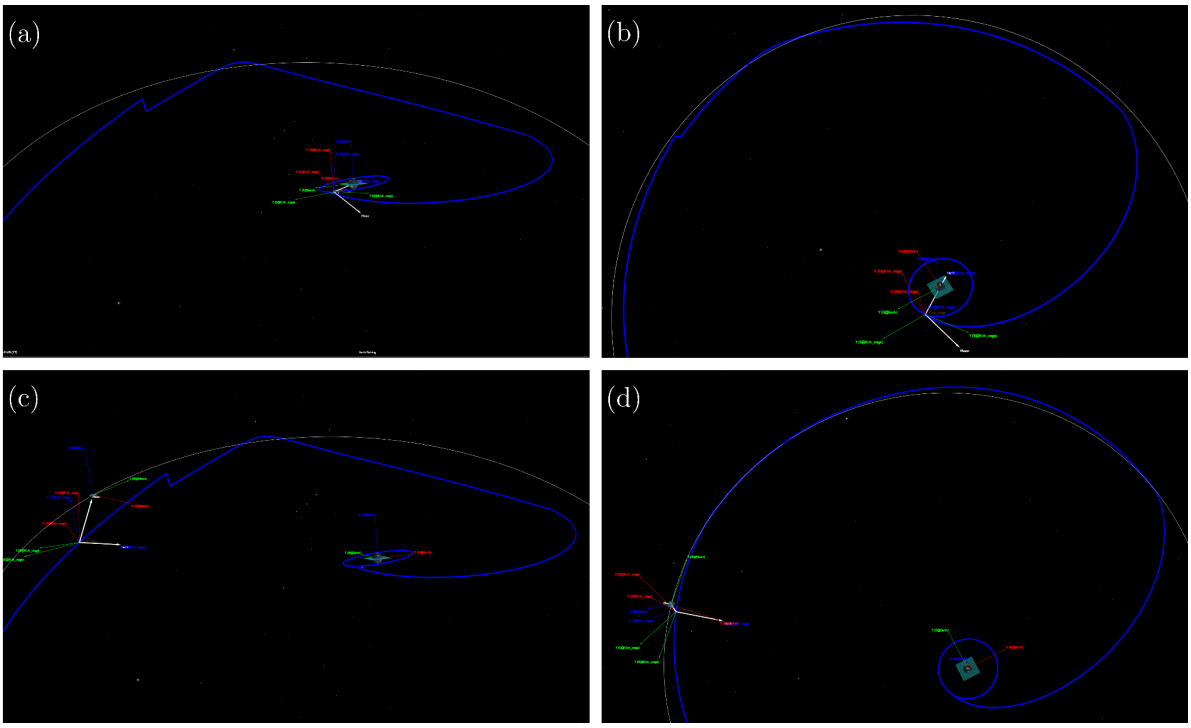

Figure 21: Short-term transfer trajectory (blue line) from GEO to NRHO around EML_2 (Scenario 2a). (a) Angular view on parking orbit (t = 0.0 s). (b) Planar view on parking orbit (t = 0.0 s). (c) Angular view on destination orbit (t = 1,357,360.0 s). (d) Planar view on destination orbit (t = 1,357,360.0 s).

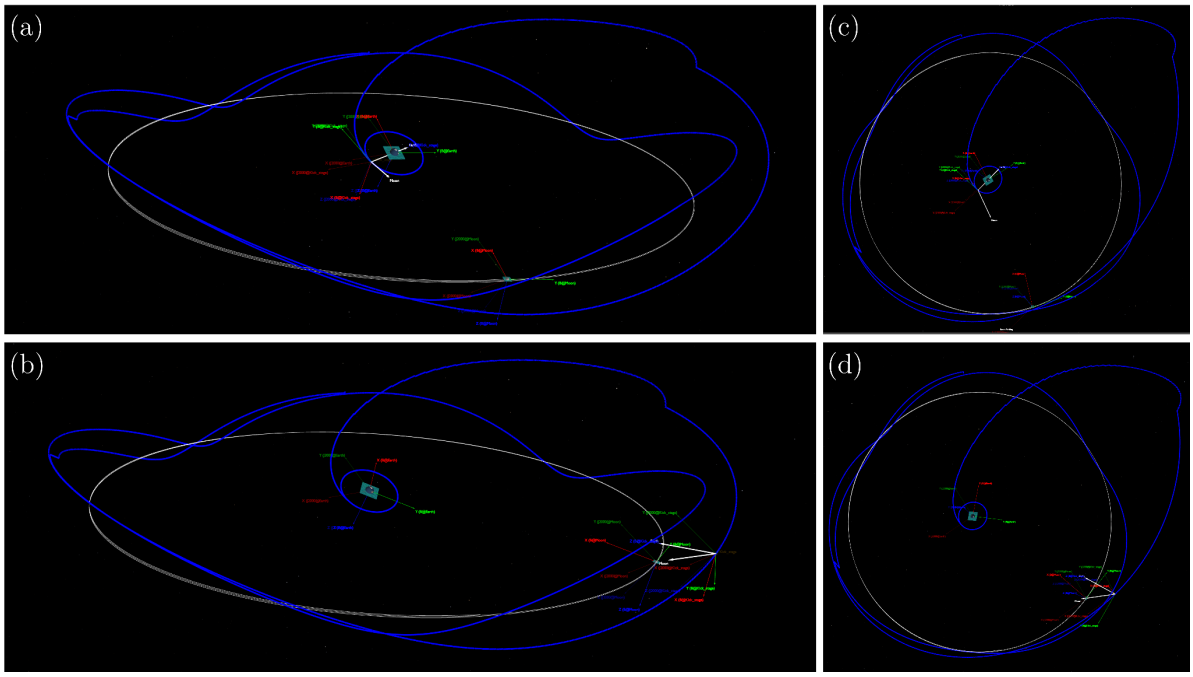

Figure 22: Long-term transfer trajectory (blue line) from GEO to NRHO around EML_2 (Scenario 2b). (a) Angular view on parking orbit (t = 0.0 s). (b) Planar view on parking orbit (t = 0.0 s). (c) Angular view on destination orbit (t = 2,075,466.4 s). (d) Planar view on destination orbit (t = 2,075,466.4 s).

The simulative mapping of the communication coverage with the lunar south pole area also reflects a significant improvement to a maximum coverage of up to 92%. The increased coverage is also evident in the area of the Shackleton crater. The area coverage exceeds 85% in the target region (Figure 23). The comparison of the visibility of the planar halo orbit with the closest NRHO again highlights the suitability of the NRHO as a parking orbit for the raw material cargo hub. With a period of 8.87 days and a perilune distance of 11,000 km, it provides promising access to the lunar surface.

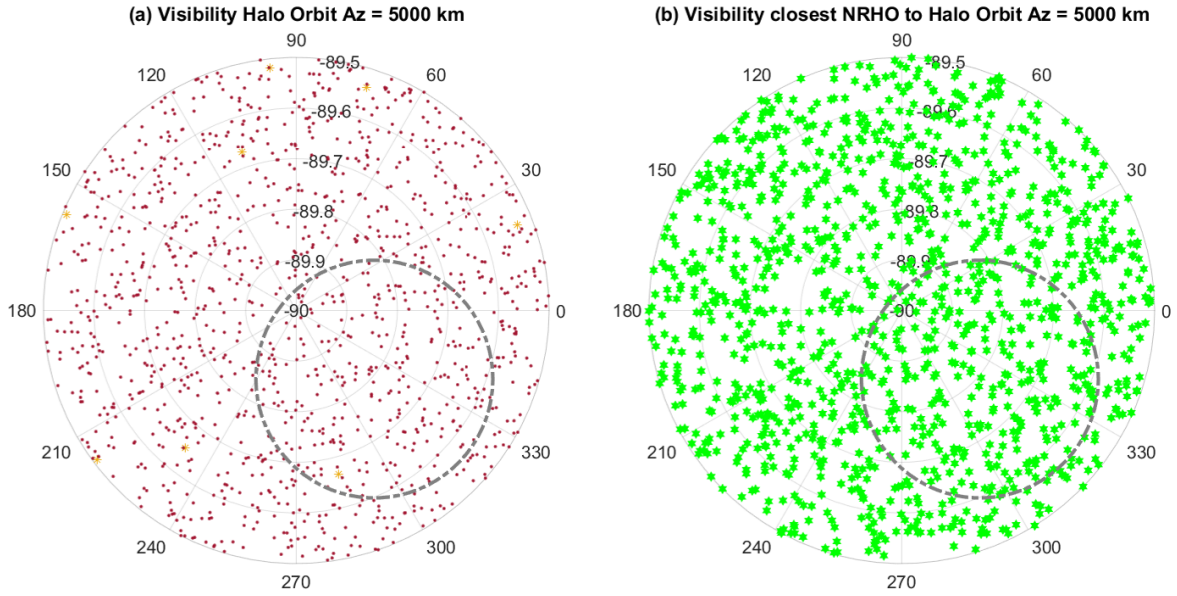

Figure 23: Comparison of communication coverage for a halo orbit with A_z = 5000 km and its closest NRHO (calculated data based on LSMAT in the latitude range of -89.5 to -90°). Average coverage around the Shackleton crater area (grey dot line) differentiated between coverage above 80% (green star), 60 to 80% (green diamond), 40 to 60% (yellow cross), below 40% (red dot).

For further evaluation of the selected NRHO, the 9:2 resonance orbit, used as Lunar Gateway orbit, and the 4:1 resonance orbit, which was also considered for the Lunar Gateway [84], were simulated. The initial state parameters can be obtained from Table 6 and Table 7.

EML-2 Orbit: 9:2 Resonance Orbit (Lunar Gateway Orbit)			
Orbit Type	NRHO		
Family	Southern		
X	1.02133	V_x	0.00000
Y	0.00000	V_y	-0.10174
Z	-0.18161	V_z	0.00000
Period	6.56	days	
$R_{periapsis}$	3300	km	
Stability index	1.304		

Table 6: Initial state parameters of 9:2 Resonance Orbit (Lunar Gateway Orbit).

EML-2 Orbit: 4:1 Resonance Orbit			
Orbit Type	NRHO		
Family	Southern		
X	1.03544	V_x	0.00000
Y	0.00000	V_y	-0.13070
Z	-0.19003	V_z	0.00000
Period	7.38	days	
$R_{periapsis}$	5600	km	
Stability index	1.615		

Table 7: Initial state parameters of 4:1 Resonance Orbit.

The comparison of the stability index reveals that the selected NRHO has a slightly higher stability index than the Lunar Gateway orbit. In addition, the NRHO has a higher perilune distance as well as a longer period, resulting in a reduction of the access to lunar surface.

Compared to the 4:1 resonance orbit, however, the selected NRHO shows higher stability, while the perilune distance is approximately doubled. The period of the 4:1 resonance orbit is slightly smaller, whereby it is not of great significance. Therefore, the selected NRHO offers a reliable solution with respect to its stability, whereby comparatively only a small ΔV-demand for stabilization can be expected. Despite a limited Pareto front, the optimization tool indicates that a lower ΔV-demand can be expected for the two reference orbits (Figure 24, Figure 25), but the current simulation does not provide a solid statement. The comparison of the communication coverage simulation indicates that the Lunar Gateway orbit provides the highest coverage with an overall visibility of more than 90%. However, it also is evident that the selected NRHO provides sufficient spots in the area of the Shackleton crater with similarly high coverage, ensuring a sufficient communication. Compared to the 4:1 resonance orbit, however, the selected NRHO shows a higher stability, whereas the perilune distance is about twice as large. The period of the 4:1 resonance orbit is slightly smaller, whereby it is not of great significance.

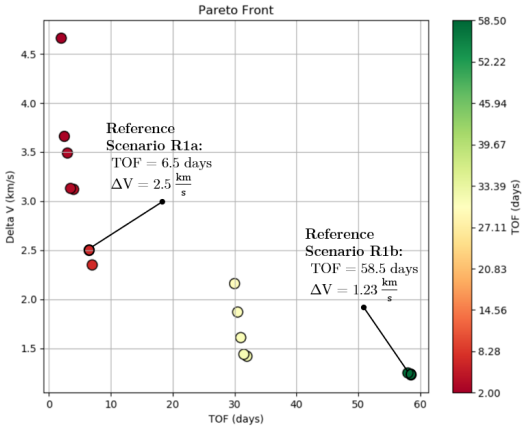

Figure 24: Pareto front for transfer from GEO to 9:2 resonance orbit (Lunar Gateway orbit). Scenario R1a: *TOF* of 6.5 days and ΔV-demand of 2.5 $\frac{\text{km}}{\text{s}}$. Scenario R1b: *TOF* of 58.5 days and ΔV-demand of 1.23 $\frac{\text{km}}{\text{s}}$.

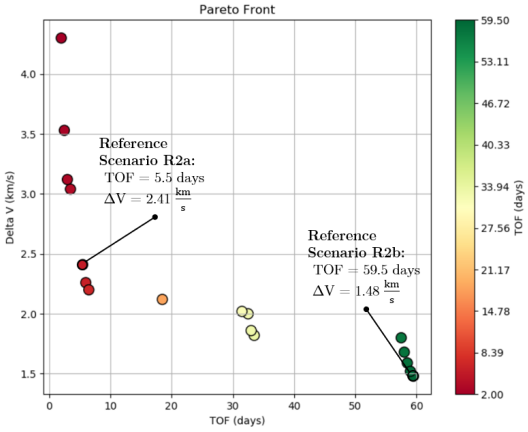

Figure 25: Pareto front for transfer from GEO to 4:1 resonance orbit. Scenario R2a: *TOF* of 5.5 days and ΔV-demand of 2.41 $\frac{\text{km}}{\text{s}}$. Scenario R2b: *TOF* of 59.5 days and ΔV-demand of 1.48 $\frac{\text{km}}{\text{s}}$.

The comparison of the communication coverage simulation indicates that the Lunar Gateway orbit provides the highest coverage with an overall visibility of more than 90%. However, it is evident that the selected NRHO provides sufficient spots in the Shackleton craters with similarly high coverage, ensuring a sufficient communication (Figure 26). The comparison between the 4:1 resonance orbit and the selected NRHO suggests potentials but confirms the adequate coverage for the intended objectives (Figure 26).

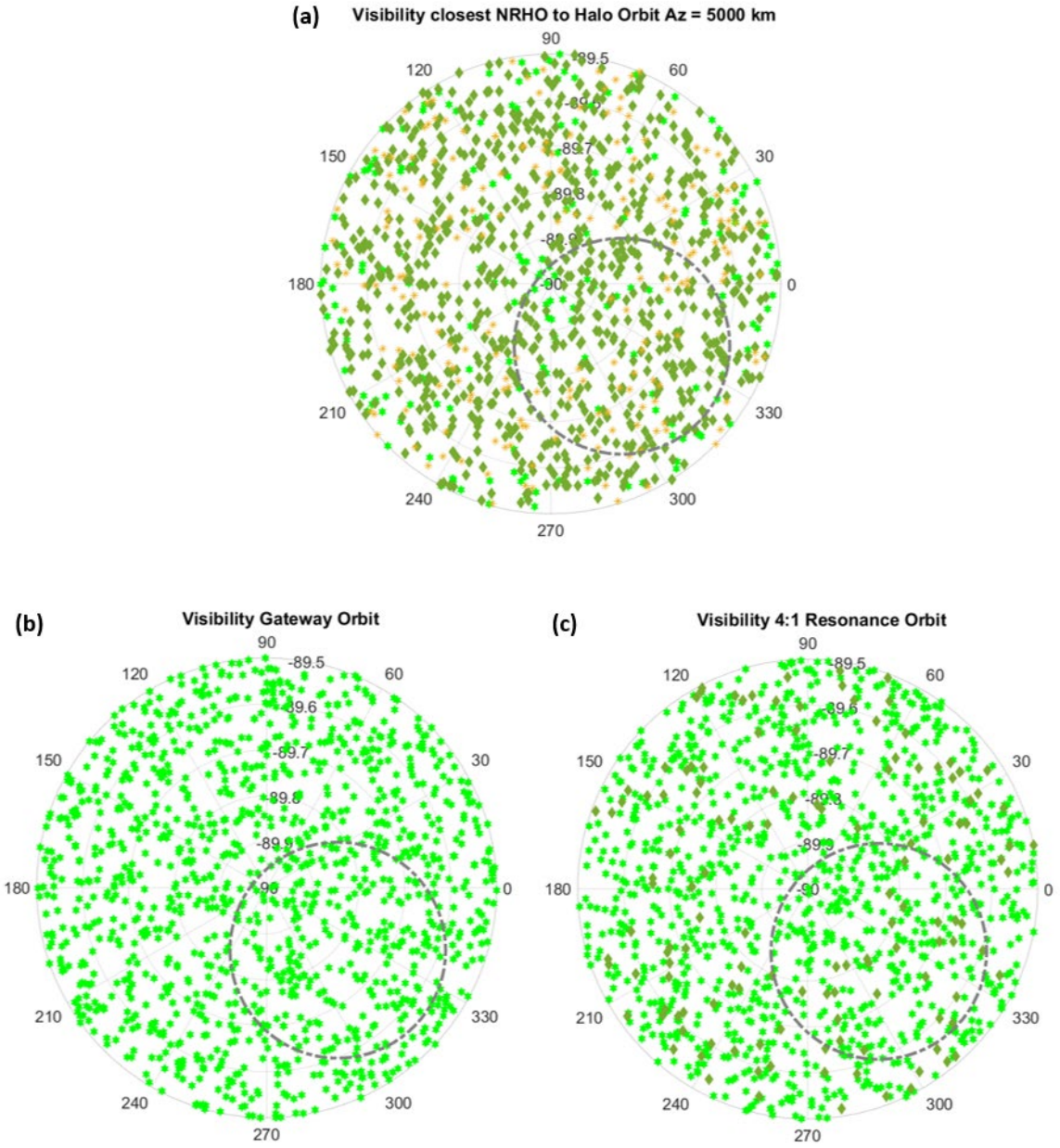

Figure 26: Comparison of communication coverage for the selected NRHO (a) with 9:2 resonance orbit (b) and 4:1 resonance orbit (c) (calculated data based on LSMAT in the latitude range of -89.5 to -90°). Average coverage around the Shackleton crater area (grey dot line) differentiated between coverage above 90% (green star), 85 to 90% (green diamond), 80 to 85% (yellow cross), below 80% (red dot).

Consequently, based on the initial simulation results in terms of ΔV-demand, stability, period, as well as coverage of the lunar south pole region, it can be concluded that the closest NRHO offers better initial conditions than the planar halo orbit for a cargo hub at EML_2, especially in terms of coverage as well as stability. The selection of a NRHO with a larger perilune distance facilitates the avoidance of interference with the Lunar Gateway orbit. Due to the high payload rate of the coilgun (Chapter 5.2.3) and the

associated amount of cargo blocks in orbit, the potential collision risk can be reduced. However, a more detailed analysis between the lunar surface-based trajectories to EML_2 and the Lunar Gateway orbit has to be performed.

In conclusion, first simulations for the transfer trajectories between GEO and EML_2 were performed based on a suitable NRHO. Furthermore, the selected NRHO was evaluated with respect to its sufficient communication coverage. The optimization tool currently includes direct and manifold transfers, whereas an extension to a targeted optimization with Lunar Flyby (LFB) maneuvers is intended to achieve a further reduction of the ΔV-demand.

4.3 Lunar Orbit-based Trajectory

Once the high masses have been successfully transferred to EML_2, the focus will be on further transport to SEL_1. Due to the low ΔV-demand for the transfer between EML_2 and SEL_1 (chapter 4.4), a low-thrust transfer of the bundled cargo packages by space tugs based on solar sails or laser-beam sails is proposed. An energy-efficient transfer starting from EML_2 to SEL_1 has to be designed, but this is not randomly feasible due to the limited transfer possibilities from the Earth-Moon system to the Sun-Earth system Figure 27.

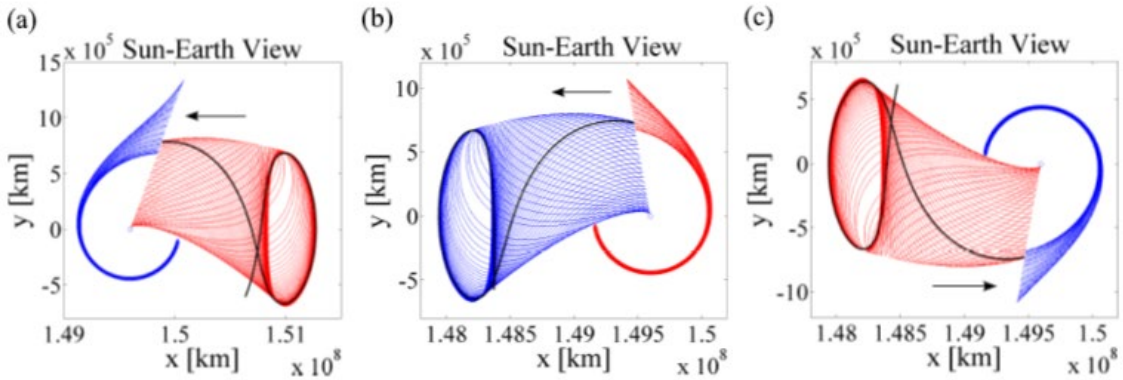

Figure 27: Possible Transfers between EML_2 and SEL_1 / SEL_2. Unstable manifold trajectories in red, stable manifold trajectories in blue. Arrows indicate the direction of flow [85].

Simplified models for impulsive maneuvers indicate that a maneuver-free transfer between the two systems is partly possible [85], but only limited parameter combinations

are allowed. Due to the complexity of the trajectories, larger deviations can occur after converting the trajectory from the simple to the high-fidelity model [85]. The use of low-thrust propulsion systems increases the complexity of the overall system, therefore iterative approaches considering the relevant boundary systems are investigated [86]. In combination with a guided optimization, the effects of a low-thrust propulsion system near Lagrange points can be simulated to detect exit strategies. Within the framework of the optimization tool of Astos Solutions [77], an extension for the calculation of transfer possibilities between two systems is currently in progress and will be designed in future studies.

4.4 ΔV-Mapping

The required ΔV-demand for the defined trajectories for the different phases is shown in Figure 28. The required ΔV-demand depends on the transfer method used as well as the intended TOF, thus direct transfers, as already shown in chapter 4.2, have significantly higher ΔV-demands than indirect transfers with a higher TOF. For the trajectory designed in chapter 4.2 four different transfer methods are feasible.

The shortest transfer possibilities in the Earth-Moon system are direct transfers (DT) with a ΔV of about 4000 $\frac{\mathrm{m}}{\mathrm{s}}$ and a TOF between 3 and 15 days [29]. These classical ballistic transfers require one maneuver to leave LEO and one maneuver to enter the halo orbit.

A reduction of the ΔV-demand can be achieved by an indirect transfer using the EML_2 stable manifold. An optimal point for the entry into the manifold is identified, guiding the spacecraft into the corresponding halo orbit. The TOF varies in dependence of the entry point, allowing an optimization of the manifold transfer with respect to TOF or ΔV [14]. The manifold transfer is also an impulse transfer requiring a boost to leave LEO and another one to enter the manifold at the entrance point. Optimizations have shown that a minimum ΔV-demand of 3200 to 3300 $\frac{\mathrm{m}}{\mathrm{s}}$ can be achieved, while increasing the TOF to 50 to 150 days. In addition, optimizers have been developed to provide low energy solutions in the range of 3200 $\frac{\mathrm{m}}{\mathrm{s}}$ depending on the TOF [28].

An extension of the manifold transfer uses a LFB, where the entrance point is chosen close to the Moon and is therefore no longer freely optimizable. The slingshot effect at

the entry into the manifold is used to optimize the altitude of the lunar LFB and the relative angle to the Moon. As a result, the ΔV-demand can be reduced to 3300 to 3400 $\frac{\mathrm{m}}{\mathrm{s}}$, and significantly shorter TOF of 10 to 25 days can be achieved [15; 17; 35].

The last possibility is the use of weak stability boundaries (WSB), utilizing a two patched three-body problem to include the influence of the Sun. The stable manifolds of the Sun-Earth system are closer to Earth than the unstable manifolds of the Earth-Moon system, therefore the trajectory properties near the Sun-Earth manifold [18] are exploited to leave LEO with a reduced effort and enter a stable Earth-Moon manifold. The WSB strategy requires the longest TOF between 80 and 120 days but provides the lowest ΔV-demand between 3100 and 3200 $\frac{\mathrm{m}}{\mathrm{s}}$.

Based on the ΔV-mapping for the complete mission scenario, the designed trajectories can be optimized in further studies with respect to ΔV as well as TOF.

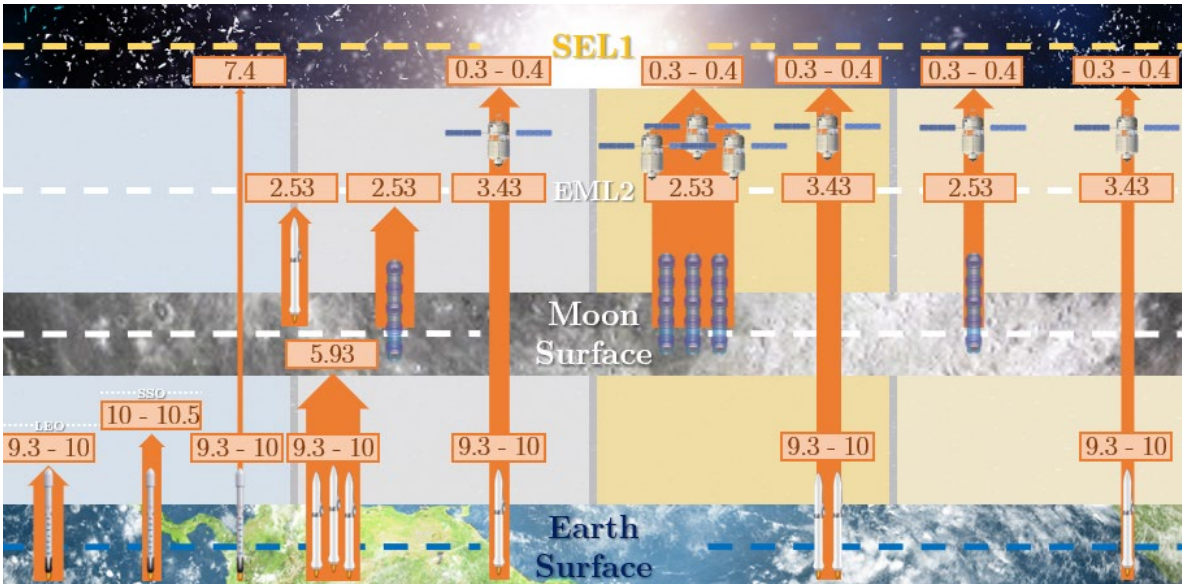

Figure 28: ΔV-mapping for transfer trajectories of the complete mission scenario with required ΔV in $\frac{\mathrm{km}}{\mathrm{s}}$.

5 IPSS Launch System

A key contribution to an efficient IPSS system deployment process is the launch technology to deliver the hundreds of megatons of material in addition to the infrastructure facilities to the Moon, EML_2, and SEL_1. Compared to the previous achievements of mankind in the last two decades to establish an international space station with a current total mass of 420 t, the high mass requirement forms an enormous challenge. To cope with this challenging task, it is necessary to combine current chemical-conventional launcher with propellant-less, mass-efficient launch technologies. The following chapter presents a composition of selected launch technologies, which are designed for the logistical transport of the high masses within the scope of this work.

5.1 Heavy Launcher

Chemical launchers are the only way to launch high masses from the Earth's surface into orbit, since electric propulsion systems do not allow direct utilization from the Earth's surface due to their low thrust [87]. Nowadays, a variety of different launchers are available, which are optimized for different mission scenarios with regard to their payload potential and performance. As a result, a variety of chemical heavy launchers were analyzed regarding the key performance parameters in order to consider not only a simple cost-based approach, but also to create opportunities for international collaboration.

5.1.1 Launcher Requirements

Due to the differing transport masses and target orbits, based on the respective phase, the accessible orbits, the maximum payload, and the specific launch costs have a decisive impact. In addition, the reusability and refueling capability in orbit as well as on the lunar surface will be examined in order to enable a roundtrip transfer to the targeted location. Based on the roadmap and the defined trajectories, described in chapter 3 and chapter 4, the derived requirements (Table 3) for the launchers for the different phases are outlined in the following.

In the first phase, in which the first technology demonstrators are placed in Earth orbit, the processing procedures on the lunar surface are demonstrated, and the first Earth-built sunshade is finally transported to SEL_1, high payload transfers are not required. Consequently, in the first phase in-space refueling does not become a decisive factor. However, in the second phase, high masses have to be transported to build up the lunar infrastructure at the lunar south pole as well as the demonstrators of the production facilities in lunar orbit. In order to transport the necessary materials and equipment from Earth and to enable the transfer from the lunar surface to EML_2, launchers with in-space refueling capabilities will be of major importance. Thus, these enable a logistical exchange between the lunar south pole and EML_2 utilizing lunar water resources. In the third phase, the high masses of raw material for the construction of the sunshades are delivered by the coilgun. Nevertheless, Earth-based components as well as components of the final production facilities still have to be transported to EML_2 by chemical rockets and from there to SEL_1 by space tugs. In Phase 3, chemical rockets have a secondary role, providing only a backup solution in the case of coilgun failures. In the final phase, chemical rockets must have the ability to supply the production site at SEL_1 with Earth-based components.

5.1.2 Launcher Evaluation

Based on the defined launcher requirements (chapter 5.1.1), current and future heavy launchers were examined with regard to their suitability. In the selection process, emerging space nations such as China and India were also considered in order to demonstrate the possibilities for international cooperation (Table 8). The development of new heavy launchers is additionally powered by the international new race to the Moon [88] as well as to Mars [89], resulting in a variety of heavy launchers on the schedule for this decade.

Launcher	Manufacturer	Nation (National Space Agency)	Release
Ariane 5	Ariane Group	Europe (ESA)	1996
Delta IV Heavy	United Launch Alliance	USA (NASA)	2002
Atlas V	United Launch Alliance	USA (NASA)	2002
Falcon 9	SpaceX	USA (NASA)	2010
Long March 5	CALT	China (CNSA)	2016
Falcon Heavy	SpaceX	USA (NASA)	2018
Starship	SpaceX	USA (NASA)	2021
Space Launch System	Boeing	USA (NASA)	2021
H3	Mitsubishi	Japan (JAXA)	2021
Ariane 6	Ariane Group	Europe (ESA)	2022
New Glenn	Blue Origin	USA (NASA)	2022
ULA SHLV	ISRO	India (ISRO)	2022
Vulcan Centaur Heavy	United Launch Alliance	USA (NASA)	2023
Yenisei	RSC Energia	Russia (Roscosmos)	2028
Long March 9	CALT	China (CNSA)	2030
H3 Heavy	Mitsubishi	Japan (JAXA)	2030

Table 8: Overview of International Launcher ordered by release year.

Based on the current state of the art, the Falcon Heavy as well as the Starship offer the best options for mass transportation from Earth. For the first demonstrator phase in the upcoming decade, the Falcon Heavy offers sufficient capacity to place the first sail demonstrators in Earth orbit due to its already successful operation and with a maximum payload of 63.8 t in LEO. Following a not purely cost-based approach, other international launchers, such as Ariane 6, Long March 5, and ULA SHLV could also be used to transport the first demonstrator sails in order to promote international cooperation. In order to transport the Earth-built demonstrator to SEL_1, the Falcon Heavy provides sufficient capacity with 16.8 t of payload.

For the purpose of revealing the feasibility of production demonstrators at EML_2, a high transfer capacity should be provided. The most promising rocket to transfer high masses to EML_2 is SpaceX's Starship. With the successfully completed high-altitude flight test of Starship SN10, SpaceX is getting closer to the ability to lift-up higher masses at lower specific payload costs than with the Falcon Heavy [90]. The future goal to stabilize descending rocket by the flip maneuver without a necessary launchpad will also enable Starship the possibilities to land on the Moon, Mars, and beyond. Currently, due to its low specific payload cost (Appendix B), Starship offers the most favorable opportunities to supply not only the demonstrator facility at EML_2 but also the final production facility at SEL_1 with complex parts and electronic components from Earth which cannot be produced from lunar regolith. The low targeted cost for a Starship launch of only \$28 million combined with the possibility of fully refueling in orbit with five additional Starships [78], lowers the specific payload cost to 1400 $\frac{\$}{\text{kg}}$. Thus, with its high payload of 100 t and low specific payload cost, the Starship significantly undercuts all competing launchers.

5.2 Mass Driver

The following chapter firstly describes the two basic concepts for a mass driver and their different advantages as well as disadvantages. Based on the local conditions on the Moon and the latest advances in the field of superconducting materials, a coilgun concept was selected, which is discussed in more detail in the following chapter with regard to its design and performance. In order to design a concept capable of being implemented as far as possible, the design of the lunar coilgun was derived from terrestrial coilgun projects.

5.2.1 Massdriver Concepts

The basic idea of a mass driver to transport high masses in the solar system instead of the multitude of rockets was already discussed in the works of O'Neill [91]. Subsequently, electromagnetic launcher technology has been examined for terrestrial [92–94] and lunar applications [95; 96] as well as in orbit [97].

In principle, a massdriver uses electromagnetic acceleration to transport payloads. The conceptual design can be distinguished between a railgun and a coilgun.

The concept of a Lorentz Rail Accelerator (LRA) or **railgun** is based on the utilization of the Lorentz force on an armature in a strong magnetic field induced by high currents. The two rails are connected by the armature, allowing the strong current to pass through the armature inducing the Lorentz force in rail direction (Figure 29).

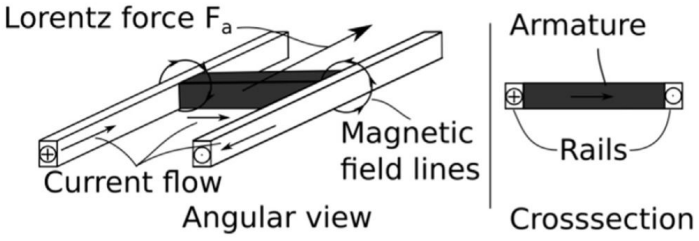

Figure 29: Functional principle of a railgun [98].

The resulting Lorentz force is proportional to the current I, the connecting length of the armature l, and the magnetic flux density B. Due to its simple design as well as launch performance capabilities, it has been highly considered not only for military applications [99; 100] but also for lunar transportation [97]. Despite the simplicity of the design and the ease of detecting defects, wear due to friction between the rails and the

armature requires constant maintenance. In addition, heat generation due to the contact-based guidance increases with heavy loads, high voltage and reduces the number of launch cycles [97].

Coilguns are also known as Gauss rifle, referring to the German mathematician and physicist Carl Friedrich Gauß, who, however, was only concerned with the fundamentals of magnetism. In contrast to railguns, coilguns currently have a lower Technology Readiness Level (TRL) due to their complexity. However, their functional principle enables a significant reduction in the primary weakness of a railgun regarding structural wear. Therefore, coilguns were already investigated as promising transport technologies in initial research of the National Aeronautics and Space Administration (NASA) on space resources and future space settlements [101; 102]. The functional principle is based on the electromagnetic interaction between the payload, called bucket, and a strong magnetic field induced by coils through which a high current passes (Figure 30).

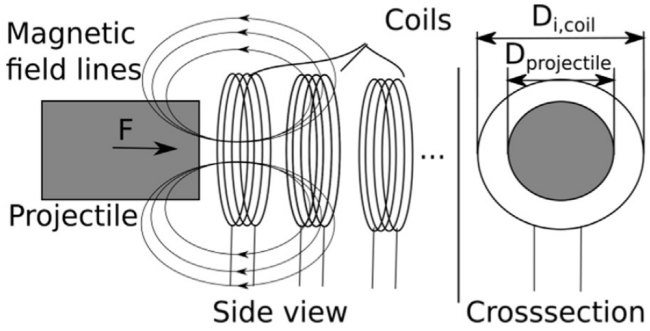

Figure 30: Functional principle of a coilgun [98].

Furthermore, the coilgun can be designed based on reluctance or inductance. The primary utilizes the interaction between the high-current coils and the bucket made of ferromagnetic material or alternatively magnetized by permanent magnets to induce the acceleration force [103–105]. The latter design also enables non-ferromagnetic payloads by wrapping an additional coil around the payload, which induces the driving force due to the interaction with the outer coils [101; 102; 106].

Due to the high masses and associated high launch frequency, this thesis focuses on the coilgun concept to reduce high maintenance requirements. In addition, an inductance coilgun is considered for the application, as it enables high velocities to bring the payload into orbit and also avoids the need for heavy ferromagnetic materials, which additionally suffer from magnetic saturation problems in high magnetic fields [107].

5.2.2 System Requirements

The following system requirements were defined for the design of the system architecture (Table 9). Based on the estimated mass of the sunshade constellation, the coilgun must be able to launch a total mass of 74 to 286 Mt of processed raw material in a time frame of twenty years [13].

Design Parameter	System Requirements
Launch mass ($m_{payload,total}$)	73.74 to 286 Mt (timeframe of 20 years) [13]
Launch mass rate (LMR)	420.6 to 1631.3 $\frac{t}{h}$
Launch velocity (v)	2.6 $\frac{km}{s}$
Environment	location with low temperature, low temperature gradient and constant illumination
Energy	sufficient energy supply and efficient energy storage
Communication	high visibility of EML_2
Maintenance	low structural abrasion

Table 9: System requirements for a lunar coilgun architecture.

Consequently, the right balance in terms of transport mass per launch and launch frequency must be identified in the design of the massdriver. Due to the uncertain lunar terrain, a compact design should be targeted, allowing at the same time a low-wear operation. Based on the lunar environmental conditions, a suitable location with constant temperatures should be targeted. The coilgun should be able to accelerate the payloads to a launch velocity of 2.6 $\frac{km}{s}$, ensuring sufficient velocity to reach EML_2 [108], taking tolerance deviations into account. Apart from the coilgun itself, sufficient power supply must be feasible to enable the infrastructure to provide efficient energy storage and subsequent local energy conversion to generate the high magnetic field variations.

5.2.3 System Architecture

Based on the defined system requirements, the system architecture of the coilgun concept was derived, which is schematically illustrated in Figure 31.

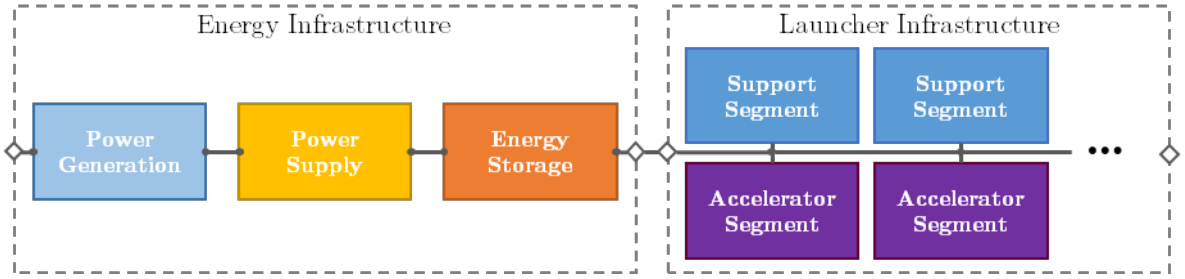

Figure 31: Schematic block diagram of coilgun design. Coilgun design divided into energy and launch infrastructure, energy infrastructure segments consisting of power generation, power supply, and energy storage, launch infrastructure segments consisting of combined units of support segments and accelerator segments.

In the conceptual design a mass estimation for the structural segments of the coilgun, the infrastructure segments of the power supply, as well as for the construction machinery was conducted. Additionally, for the purpose of improving energy consumption and TRL, energy storage and the driving coils shall be designed using superconducting material [109; 110]. The power supply requirements as well as the usability of superconducting materials result in constraints with regard to the location of the coilgun. In addition, the lunar polar regions are in focus for a lunar base concerning the raw material deposits, especially water. The results of Lunar Orbiter Laser Altimeter (LOLA) have shown that most of the water can be found in the polar craters [111], thus it can be used as a fuel source for the production of hydrogen and oxygen by electrolysis. Based on these findings, the Shackleton crater at the lunar south pole was chosen for further conceptual design (Figure 32). Due to its large diameter of 20 km, the crater is sufficient for the positioning of the coilgun. The location of the crater directly at the pole contributes to the coilgun design.

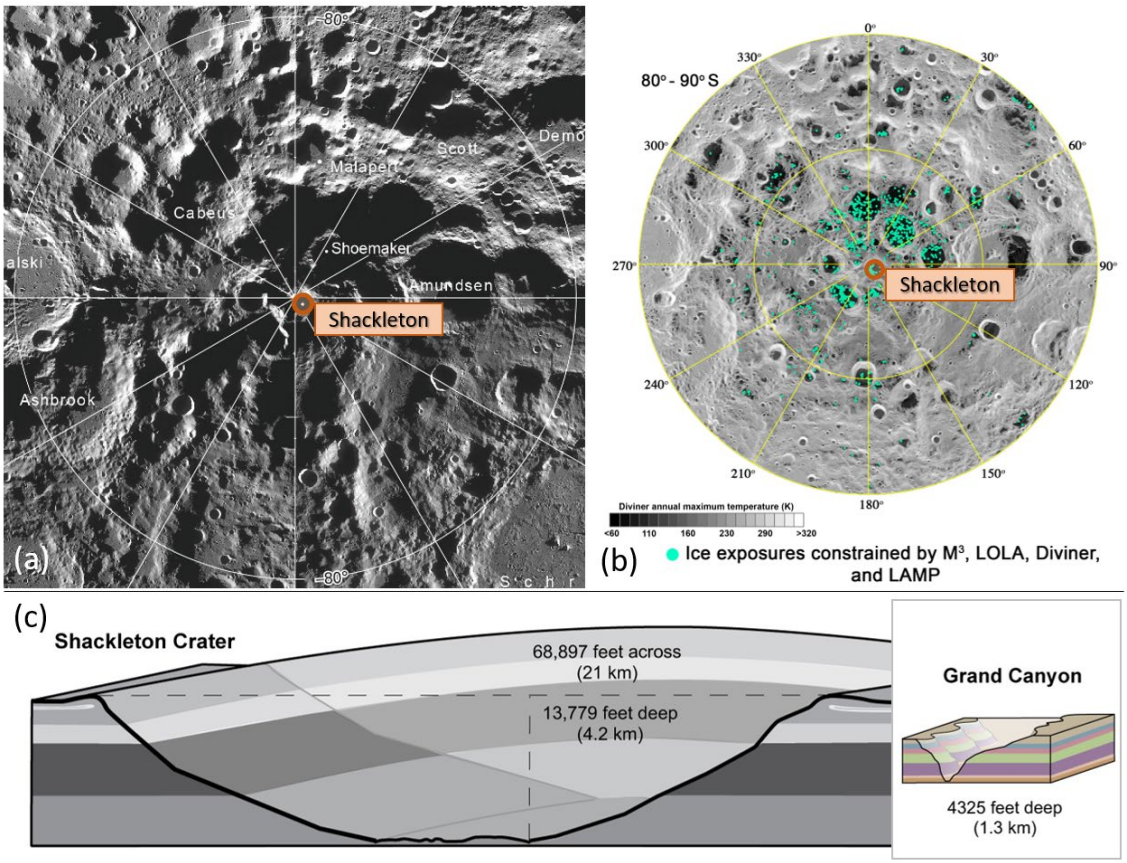

Figure 32: Characteristics of the Shackleton Crater. (a) Location of the Shackleton Crater at the lunar south pole [112]. (b) Availability of water ice in lunar crater regions [111]. (c) Dimension of the Shackleton Crater referring to the Grand Canyon [112].

Compared to equatorial regions, the area around the Shackleton crater is almost continuously in sunlight [113], which can be used to generate energy using solar arrays fabricated from lunar material [114]. At the same time temperatures are not as high as at the equator, where the temperature can reach 400 K [115]. The low Sun results in maximum temperatures around 340 K at the crater slopes [116]. In the crater itself, which is not exposed to sunlight throughout the year, maximum temperatures are around 90 K [116]. Due to the low temperatures, the application of superconducting materials enables a promising technology for effective energy storage as well as for the generation of large magnetic fields, or in the case of an inductive coilgun, a rapidly changing magnetic field. Thus, the application of superconducting material as well as the location in the crater using the crater slopes for energy generation fulfill the defined infrastructure requirements.

Figure 33 demonstrates the system architecture of the coilgun with the functionally relevant components.

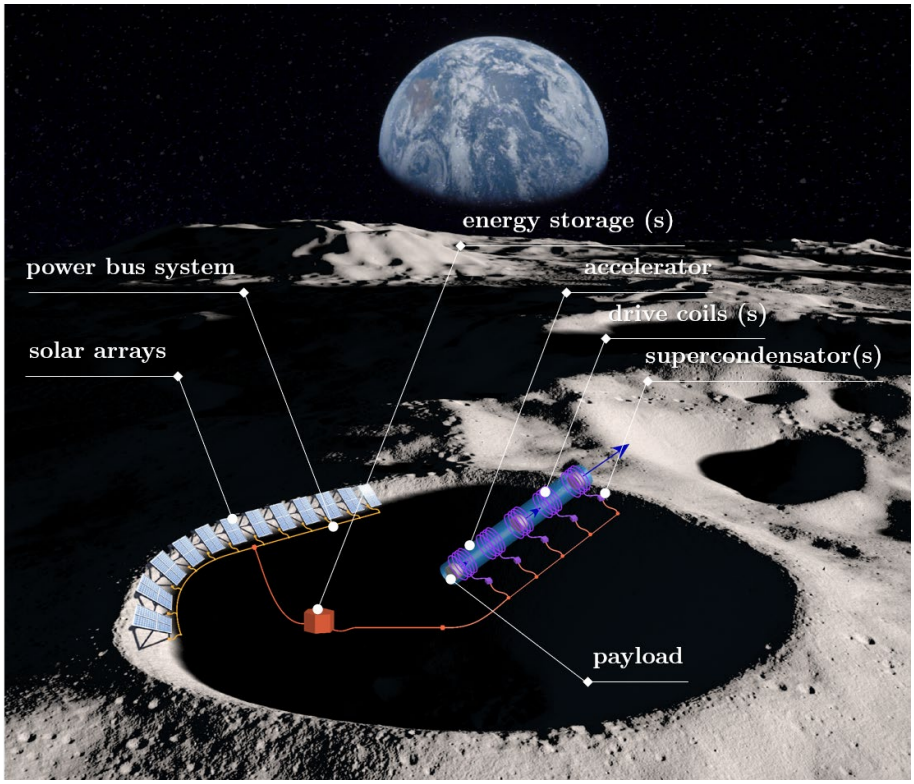

Figure 33: System architecture of the coilgun with the functionally relevant components. Energy storage, drive coils and supercondensators made of superconducting material(s).

The power supply is provided by solar arrays fabricated out of lunar regolith [114], which are positioned on the crater slopes. The power is subsequently transferred by a conventional power bus system to an energy storage device located in the crater, which is made of superconducting compounds [110], with the advantage of minimizing energy loss while taking advantage of the low temperatures inside the crater. The rectilinear accelerator can be constructed along the crater slopes, which are not exposed to sunlight, by utilizing Rare Earth Barium Copper Oxide (REBCO)-based superconducting magnetic coils [110] to accelerate the payload. A variation of the accelerator shape can offer optimization potential with regard to different aspects, which is shortly discussed in chapter 5.2.6. Local supercapacitors are used to realize high-frequency discharge pulses to generate rapidly alternating magnetic fields. After the payload or projectile is accelerated to the required velocity, the directing tubes are used to launch the raw material cargo into orbit.

Apart from the launch infrastructure on the Moon, a logistical system in the intended EML_2 orbit is required to capture the arriving cargo blocks and to assemble them at the cargo hub. In order to support the interception system and provide orbit correction, the

cargo blocks will be equipped with a small propulsion and communication unit, capable of performing local orbit corrections. Based on the required high mass rate, the operation of an active interceptor fleet at EML_2 is not considered, because the fuel requirements and the size of the fleet would demand an extensive logistical effort. Initial estimations and a rough design of the control system are presented in the upcoming chapter.

The positioning of the coilgun at the Shackleton crater offers a suitable baseline for future lunar missions [117] such as for the installation of an infrared telescope [118]. In addition, the Shackleton crater is in the focus for potential extravehicular activities (EVA) at the lunar south pole within the Artemis 2024 program [119]. Thus, the coilgun in combination with a radio relay station at the Malapert Mountain [120], which is located 120 km from the crater, can provide a solid starting point for a lunar outpost [121].

5.2.4 Coilgun Design

Despite numerous publications related to coilgun designs, estimation of design parameters is limited. For this purpose, the design of the lunar coilgun is based on the design parameters for a terrestrial application [122]. The coilgun variant of the Electromagnetic Mortar (EMM) [123; 124], developed by the US Defense Advanced Research Projects Agency (DARPA) provides the baseline for design of the lunar coilgun. The EMM is a closed system, which is intended to demonstrate the possibilities for an electromagnetic mortar, whereby the ability to achieve high velocities, at a high firing rate as well as sufficient accuracy should be demonstrated.

A closed design generally means that a fixed payload geometry has to be provided. Since the coilgun is primarily intended for the transport of raw material blocks, this aspect does not constitute an exclusion criterion for the design. Consequently, the diameter of the coilgun and consequently the diameter of the payload is limited by the maximum possible dimension of the magnetic field generating superconducting coils.

In addition, a strong magnetic field variation is essential for the acceleration of high masses. Current superconductors are unable to achieve such high field variation [125], but efforts are currently in progress within the SPARC project [126] to enable large-scale high field high temperature superconductors (HTS) for application in tokamak fusion reactors. The Massachusetts Institute of Technology (MIT) and Commonwealth Fusion Systems (CFS) are collaborating to enable large-bore, high-field REBCO magnets by

2023. Pulsed magnetic fields with a cycle time of 10 seconds (s) are planned as part of the SPARC net-energy tokamak project. In addition to HTS coils, HTS cables for high current supply are also investigated. Thus, with these promising technologies low energy loss and fast energy supply for the coils can be achieved. In the next step, the impact on efficiency as well as the suitability for space applications have to be tested.

Derived Design Parameters

Based on the characteristics of the EMM coilgun version (Table 10), the generalized design parameters for the lunar coilgun can be derived (Table 11). The energy E of the EMM is calculated from the EMM payload $m_{payload,EMM}$ and the intended velocity v. The force F on the EMM accelerator with the track length L, the resulting acceleration a, and the mass per unit length ϑ, characterized by the ratio between the total EMM mass M and L are essential parameters. The possible launch mass $m_{EMM,EML2}$, which is transported to the EML_2 with the performance of the EMM system, serves as an indication of the current performance of the EMM system.

Characteristics	Parameter	Value	Unit
Launch mass	m	18	[kg]
Velocity	v	430	[m/s]
Track length	L	2.4	[m]
Total mass	M	1,516	[kg]

Table 10: Characteristics of EMM coilgun version [123; 124].

The comparison of the derived design parameters with other terrestrial electromagnetic launchers such as the Electromagnetic Aircraft Launch System (EMALS) [127] indicates that with an increasing payload mass, ϑ also grows [122], as the coilgun structure is exposed to higher loads. Hence, the lowest possible payload mass per launch favors a lightweight coilgun design. However, it should be noted that the high mass demand (Table 9) over the defined period of 20 years requires an average mass flow between 421 to 1632 t per hour ($\frac{t}{h}$), which is used for further calculations.

Design Parameter	Physical Equation	Design Value	Unit
Payload kinetic energy	$E = \frac{1}{2}\, m_{payload,EMM} v^2$	1.66E+06	[J]
Force	$F = \frac{E}{L}$	6.93E+05	[N]
Acceleration	$a = \frac{v^2}{2L}$	3.85E+04	$[\frac{\mathrm{m}}{\mathrm{s}^2}]$
Launch mass to EML_2	$m_{EMM,EML2} = \frac{2E}{{v_{EML2}}^2}$	4.92E-01	[kg]
Mass per unit length	$\vartheta = \frac{M}{L}$	6.32E+02	$[\frac{\mathrm{kg}}{\mathrm{m}}]$

Table 11: Derived design parameters from EMM characteristics for a coilgun based on a launch velocity of 2.6 $\frac{\mathrm{km}}{\mathrm{s}}$ to reach EML_2.

Thus, the minimum payload mass is limited by the required launch rate to ensure the mass flow. In addition, the launch rate is limited by the capacity of the interception system at EML_2, which must be able to manage high arrival rates.

Electromagnetic launchers offer the possibility of achieving high accelerations, at the cost of higher structural loads. Based on the required velocity, Table 12 illustrates the dependence between track length and achievable acceleration. For a constant payload, a longer track length results in lower loads on the structure, which allows a lower mass per unit length. By avoiding a shuttle-based coilgun design, an increase of the track length implies a longer acceleration time, but it does not affect the launch rate.

Acceleration		Track length	Launch Force	Launch time
a		$\mathrm{L} = \frac{\mathrm{v}^2}{2\mathrm{a}}$	$\mathrm{F} = \mathrm{m}_{\mathrm{payload}}\mathrm{a}$	$t_L = \frac{\mathrm{v}}{\mathrm{a}}$
[g]	$[\frac{\mathrm{m}}{\mathrm{s}^2}]$	[m]	[N]	[s]
10	9.81E+01	3.45E+04	9.81E+03	2.65E+01
100	9.81E+02	3.45E+03	9.81E+04	2.65E+00
1000	9.81E+03	3.45E+02	9.81E+05	2.65E-01
2000	1.96E+04	1.72E+02	1.96E+06	1.33E-01

Table 12: Track length, launch force, and launch time for defined accelerations regarding a launch velocity of 2.6 $\frac{\mathrm{km}}{\mathrm{s}}$ and a payload mass of 100 kg.

Due to its properties and lunar availability, aluminum is the main material component for the sunshade concept [13]. The launch force of the coilgun is based on the interaction between the external pulsed magnetic field generated by the coils and the induced eddy currents in the conductive material of the payload. Aluminum, with 37.7x10^6 $\frac{\mathrm{s}}{\mathrm{m}}$, offers about 60% of the electrical conductivity of copper, eliminating the need for additional conductive encapsulation of the processed raw aluminum for transportation. However,

the influence of contaminants on the interactions during launch should be analyzed in more detail in order to define the required quality level for processing and to prevent uncontrolled inductions.

Propulsion and Communication Module

Small deviations in the launch velocity can result from different influences such as vibrations or magnetic field variations. The distance between the center of the Moon and EML_2 is about 59,844 km (Table 2), resulting in a strongly elliptical transfer trajectory with a lunar radius of 1,737.4 km [26]. Due to the high sensitivity of elliptical orbits, even small variations in cross-track or along-track velocity can result in a position displacement of several kilometers at EML_2 [122]. For orbit correction, a propulsion and communication module (PCM) consisting of a microthruster propulsion technology, digital radio, and patch antennas is intended [122].

Assuming a specific impulse (I_{sp}) of 200 s, the propellant fraction ($\frac{m_{prop}}{m_{payload}}$) can be calculated by

$$\frac{m_{prop}}{m_{payload}} = e^{\frac{\Delta V_c}{I_{sp} g}} \qquad \text{(Eq. 4)}$$

with ΔV_c, as the maximum velocity correction and g, as Earth gravitational constant of 9.81 $\frac{\mathrm{m}}{\mathrm{s}^2}$. The EMM coilgun was designed with a velocity deviation of 1.5 $\frac{\mathrm{m}}{\mathrm{s}}$. Consequently, according to (Eq. 4), a maximum velocity correction of 3 $\frac{\mathrm{m}}{\mathrm{s}}$ would require an additional propellant fraction 0.15%. Thus, the propellant requirement for a 100 kg cargo block would be only 0.150 kg. For the further design, the PCM is estimated with a total weight of 1 kg and the attachment of the PCM to the cargo block with another 1 kg.

Definition of Key Performance Parameters

Due to the uncertain lunar terrain, a rectilinear coilgun design is considered initially. Based on the depth of 4.2 km and a diameter of 21 km of the Shackleton crater, a track length of 689 m is specified. The resulting key performance parameters are listed in Table 13, where the launch force is within the capacity of the EMM coilgun concept.

Acceleration		Track length	Launch Force	Launch time
a		$L = \frac{v^2}{2a}$	$F = m_{payload}a$	$t_L = \frac{v}{a}$
[g]	[$\frac{m}{s^2}$]	[m]	[N]	[s]
500	4.91E+03	6.89E+02	4.91E+05	5.30E-01

Table 13: Acceleration, launch force, and launch time for a track length of 689 m regarding a launch velocity of 2.6 $\frac{km}{s}$ and a payload mass of 100 kg.

Assuming scalability, the reduction of the launch force to 71% of the EMM launch force results in a reduced ϑ of 447 $\frac{kg}{m}$ and consequently in a total accelerator mass of 308 t (Table 14).

	Track length L in [m]	Launch Force F in[N]	Launch Force ratio $\frac{F_{LC}}{F_{EMM}}$ in [-]	Mass per unit length ϑ in [$\frac{kg}{m}$]	Total mass M in [$\frac{kg}{m}$]
EMM	2.40E+00	6.93E+05	70.7%	6.32E+02	1.52E+03
LC	6.89E+02	4.91E+05		4.47E+02	3.08E+05

Table 14: Calculated design parameters for a lunar coilgun with track length of 689 m regarding a launch velocity of 2.6 $\frac{km}{s}$ and a payload mass of 100 kg assuming scalability.

5.2.5 Energy Assumptions

An essential aspect for the operation of a lunar coilgun is a sufficient energy infrastructure. The efficiency of industrially available solar cells for space applications is currently 30% [128; 129]. Due to the transportation cost of terrestrial space solar cells, the utilization of lunar solar arrays is proposed. Hence, the solar arrays with an area A and an efficiency η_P provide a power supply P_P

$$P_P = AS\eta_P \quad \text{(Eq. 5)}$$

with S being the solar constant of 1,360 $\frac{W}{m^2}$. The required energy of the coilgun is defined by

$$E_C = \frac{E}{\eta_C} \quad \text{(Eq. 6)}$$

with η_C as the efficiency of the coilgun.

Consequently, the energy recharge time $t_{recharge}$ can be calculated by

$$t_{recharge} = \frac{E_C}{P_P} = \frac{E}{AS\eta_P\eta_C} \quad \text{(Eq. 7).}$$

In order to provide the high mass flow to EML_2, the required cycle time $t_{req,cycle}$ can be defined by

$$t_{req,cycle} = \frac{m_{payload}}{MLR} \quad \text{(Eq. 8)}$$

with $m_{payload}$ in kg, as payload mass per launch and MLR, as required mass launch rate in $\frac{kg}{s}$ (Table 9). As a result, based on the dependence between $t_{recharge}$ (Eq. 7) and $t_{req,cycle}$ (Eq. 8) with

$$\frac{E}{AS\eta_P\eta_C} = \frac{E_C}{P_P} = t_{recharge} < t_{req,cycle} = \frac{m_{payload}}{MLR}$$

including the provided launch energy by

$$E = \frac{1}{2}\, m_{payload} v^2 \quad \text{(Eq. 9)}$$

the relationship between the required solar array area A is obtained by

$$A(MLR) = \frac{v^2}{S\eta_P\eta_C} MLR \quad \text{(Eq. 10)}$$

as a function of the required MLR for the selected coilgun design.

Due to the high availability of lunar silicon [13], the application of lunar silicon solar cells [114] with an efficiency of 9% is suggested. At a coilgun efficiency η_C of 30%, the minimum MLR (MLR_{min}) of 117 $\frac{\text{kg}}{\text{s}}$ and the maximum MLR (MLR_{max}) of 453 $\frac{\text{kg}}{\text{s}}$ result in a required solar array area A between A_{min} of 2.20x10^7 m^2 and A_{max} of 8.52x10^7 m^2 (Table 15).

	Minimum Mass Sunshade	Photovoltaic Sunshade
Raw material MLR in [kg/h]	4.21E+05	1.63E+06
Raw material fraction	98%	98%
MLR in [kg/s]	1.17E+02	4.53E+02
A in [m^2]	2.20E+07	8.52E+07

Table 15: Required solar array area for a lunar coilgun with track length of 689 m regarding a launch velocity of 2.6 $\frac{\text{km}}{\text{s}}$ for a minimum mass sunshade and a photovoltaic sunshade.

The comparison with terrestrial photovoltaic plants such as the largest solar park on Earth, the Bhadla Solar Park in India [130], indicates that the surface area is in a similar

magnitude [131]. The simplified calculation of the power capacity of the lunar solar park leads to higher nominal power performance, compared to the Bhadla Solar Park (Table 16). However, the comparison of the capacities reveals similar order of magnitude. Furthermore, the annual addition of power in Germany by photovoltaic plants of 4.8 GW in 2020 [132], indicates the promising feasibility of the scale of a lunar solar park, producing between 2.7 and 10.4 GW.

	Minimum Lunar Solar Park	Maximum Lunar Solar Park	Bhadla Solar Park (India)
Surface area A in [ha]	2197	8516	5700
Power capacity P_P in [MW]	2689	10424	2245

Table 16: Comparison between lunar and terrestrial solar parks.

5.2.6 Design Optimization

Due to the high MLR requirement and complexity of the coilgun, service shutdowns can have a significant impact on the time schedule. Due to the compact length of only 689 m, the installation of several coilguns is reasonable. The MLR of a coilgun is limited by the preparation time between two launches. Assuming an estimated launch preparation time of 10 s would result in a MLR of 36,000 $\frac{kg}{h}$, which is 12 times lower than the required MLR for a minimum mass sunshade of 421,000 $\frac{kg}{h}$. Therefore, a precise optimization of the required number of coilguns with regard to the required mass and maintenance effort should be performed.

Based on the demand for high energy supply and energy storage capacitors with a high charge-discharge rate as well as high density energy storage are required. Current supercapacitors offer discharge cycles of 1 to 10 s [133]. Due to the short acceleration time of the rectilinear concept of 0.53 s, current supercapacitors encounter their limits. Thus, doubling the distance would lead to a halving of the acceleration and consequently to a doubling of the launch time. Consequently, a continuous operation of the coilgun with a launch mass flow of 100 $\frac{kg}{s}$ could be achieved by accepting a less compact design.

Considering the nearly flat floor and the large dimensions of the Shackleton crater, the use of a ring-shaped accelerator on the crater floor in combination with a directing tube could be a long-term and efficient solution to ensure a high mass rate (Figure 34). In this case, the payload could slowly be accelerated and be diverted tangentially through the directing tube once the launch velocity has been achieved. Such a concept is similar to the structure of a particle accelerator, like the Australian Synchrotron, and enables a stepwise velocity increase. However, due to the closed structure, the possibilities for the insertion mechanism of the payload have to be considered in more detail.

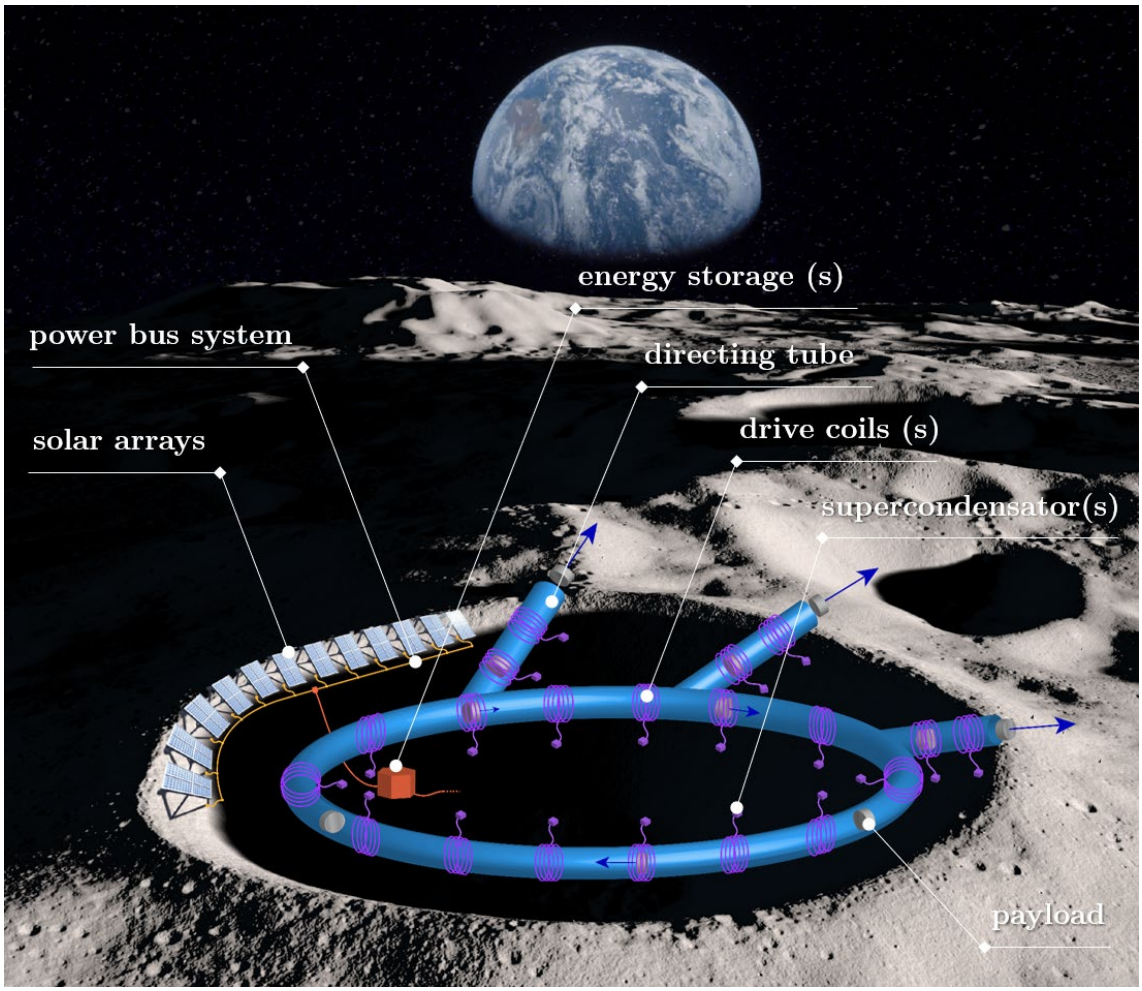

Figure 34: System architecture of a ring-shaped coilgun with the functionally relevant components. Energy storage, drive coils, and supercondensators made of superconducting material(s).

5.2.7 Mass Estimation

The high mass rate of the coilgun allows the transport of the initial materials for the construction of the sunshade constellation, but first the required resources for the construction of the coilgun on the Moon have to be provided. In the following, in addition to the estimation of the mass of the accelerator, first estimations for support structure, energy, as well as for construction infrastructure are performed.

Support Infrastructure

In order to evaluate the mass impact of the support infrastructure, a scalable concept consisting of individual accelerator segments is proposed (Figure 31). In combination with ϑ already described in chapter 5.2.4 the total mass of a single segment can be calculated. The force transmission into the crater slope is done by an anchoring in the lunar regolith, where an anchor weight of 20 kg is specified for a force load of 10,000 N [122]. The intended payload mass of 100 kg leads to an acceleration force of 490,500 N, consequently estimating 50 anchors per segment. As a result, the total mass for the anchoring is 1,000 kg per segment. Furthermore, the support structure is estimated to have an effective density of 5 $\frac{\mathrm{kg}}{\mathrm{m}^3}$ for a resistance of 10,000 N. Due to the lack of environmental influences, a significantly lower density as for terrestrial applications can be assumed. Thus, based on the acceleration force, a density of 250 $\frac{\mathrm{kg}}{\mathrm{m}^3}$ is derived. The volume of the segment is estimated to be 2% of the cube of the segment length L_s as a result of the large forces [122]. Therefore, the mass of a support segment is described by

$$M_{SS,total}\ (L_s) = \frac{L}{L_s} \cdot (M_{Anker}(m_{Payload}, m_{Anker}, a, F_{Anker}\ ) + M_{SS}(L_S, \rho_{SS}, F_{SS}) \qquad \text{(Eq. 11)}$$

with

L_s = length of the segment

$M_{Anker}(m_{Payload},\ a\ ,\ F_{Anker}\ ) = \frac{m_{Payload} \cdot a}{F_{Anker}}\ m_{Anker}$

$M_{SS}(L_S, \rho_{SS}, F_{SS}\ ) = 0.02\ \cdot\ L_s\ \cdot\ \frac{m_{Payload} \cdot a}{F_{SS}}\ \cdot\ \rho_{SS}\ .$

Optimizing the mass function for L_s results in a minimum length of $\sqrt[3]{100}$ m = 4.64 m, which means that the total length is divided into 149 segments and has a total

mass $M_{SS,total}$ of 222,700 kg. Considering the high mass requirement for the accelerator, the use of in-situ material is recommended to reduce the terrestrial mass demand. Lunar regolith has an appropriate density of 1,500 $\frac{\text{kg}}{\text{m}^3}$ [134] and consequently can be used for basic structural elements. However, complex, or safety-relevant structures should not be made from lunar regolith due to the low TRL level of lunar manufacturing processes. With an in-situ mass fraction $\psi_{in-situ}$ of the total mass of the support structure, the mass fraction of terrestrial materials is given by

$$M_{SS,total,Earth} = M_{SS,total} \cdot (1 - \psi_{in-situ}). \qquad \text{(Eq. 12)}$$

Energy Infrastructure

Based on chapter 5.2.4, the simplified energy infrastructure consists primarily of the lunar solar arrays and the high-density energy storage with high discharge rate. REBCO-based highly efficient energy storage and power supply units represent a promising technology, but for a conservative design supercapacitors are used. In contrast to classical lithium-ion batteries, these offer the advantage of a high discharge rate. However, commercial electro-chemical double-layer supercapacitors (EDLC) only have a maximum energy density of 3 to 5 $\frac{\text{Wh}}{\text{kg}}$ [135; 136], whereby ultra-high-energy density supercapacitors are currently being researched [137]. Thus, an energy density of 5 $\frac{\text{Wh}}{\text{kg}}$ is assumed for the estimation. The required launch energy of

$$E = \frac{1}{2} m_{payload} v^2 = 3.38\text{x}10^8 \text{ J} = 338 \text{ MJ} \qquad \text{(Eq. 13)}$$

results in a total mass of 18,778 kg for the energy storage based on supercapacitors.

The energy supply by lunar silicon solar cells requires a large-scale solar park, but terrestrial solar cell technology can be avoided. Nevertheless, a terrestrial mass fraction of the solar park of 0.1 % is estimated because an energy supply has to be guaranteed at the beginning of the construction process. Ultralight solar cells for space solar power satellites are expected to have a surface density ρ_A of 100 $\frac{\text{g}}{m^2}$ [138], which leads to a terrestrial mass fraction $M_{LSP,terrestrial}$ of

$$M_{LSP,terrestrial} = A \cdot \rho_A \qquad \text{(Eq. 14)}$$

resulting in $M_{LSP,terrestrial,min}$ of 2200 kg for A_{min} and $M_{LSP,terrestrial,max}$ of 8520 kg for A_{max}.

	Minimum Lunar Solar Park	Maximum Lunar Solar Park
M_{SC} in [kg]	1.88E+04	1.88E+04
A in [m²]	2.20E+07	8.52E+07
$M_{LSP,terrestrial}$ in [kg]	2.20E+03	8.52E+03

Table 17: Mass estimation for energy infrastructure. Mass for supercapacitors M_{SC} and terrestrial mass fraction $M_{LSP,terrestrial}$ of lunar solar park based on lunar solar park area A and a mass fraction of 0.1%.

Overall Coilgun Mass

Based on the previous calculations, the masses of the coilgun and its infrastructure can be summarized for the minimum mass sunshade and the photovoltaic sunshade (Table 18).

	Minimum Mass Sunshade	Photovoltaic Sunshade
Raw material MLR in [kg/h]	4.21E+05	1.63E+06
Required launches per hour with $m_{Payload}$ = 100 kg	4210	16320
Launch time in [s]	0.53	0.53
Estimated launch preparation time in [s]	1	1
Number of coilguns	1	1
Possible launches per coilgun per hour	3600	3600
Accelerator mass in [kg]	3.08E+05	3.08E+05
Raw material fraction	98%	98%
Solar park area in [m²]	2.20E+07	8.52E+07
Power capacity in [MW]	2.69E+03	1.04E+04
Total mass of support structure in [kg]	2.23E+05	2.23E+05
In-situ material mass fraction	0%	0%
Terrestrial mass of support structure in [kg]	2.23E+05	2.23E+05
Supercapacitor mass in [kg]	1.88E+04	1.88E+04
Terrestrial mass of lunar solar park in [kg]	2.20E+03	8.52E+03
Total mass of coilgun and infrastructure in [kg]	**551594**	**557913**

Table 18: Total mass estimation for a lunar coilgun and infrastructure including essential parameters. Mass fraction of lunar solar park based on lunar solar park area A and a terrestrial mass fraction of 0.1%. Calculated without in-situ material mass fraction.

It is evident that the different mass requirements for raw materials only affect the energy supply provided by the solar array area. However, a detailed analysis reveals that the delay time i.e., the preparation time between two launches, has an impact on the

schedule. The calculated launch time for the coilgun is only 0.53 s, which is less than the discharge time of the supercapacitors. The charge-discharge time is the limiting factor assuming that an unrestricted frequency of pulsed magnetic fields can be achieved. Due to the limitation of the charge and discharge rates of supercapacitors, it is not feasible to achieve the required launch rate with the defined mass of 100 kg.

For this purpose, the payload mass can be increased, but that would have an enormous impact on the total mass due to the increased force effects. The resulting magnitude of forces would question the scalability based on the EMM coilgun concept.

As already suggested in chapter 5.2.6, the approach with multiple coilguns leads to the intended result. Table 19 provides the necessary number of coilguns and the estimated mass requirement to be transported from Earth, assuming a launch preparation time of 10 s.

	Minimum Mass Sunshade	Photovoltaic Sunshade
Raw material MLR in [kg/h]	4.21E+05	1.63E+06
Required launches per hour with $m_{Payload}$ = 100 kg	4210	16320
Launch time in [s]	0.53	0.53
Estimated launch preparation time in [s]	10	10
Number of coilguns	12.0	46.0
Possible launches per coilgun per hour	360	360
Accelerator mass in [kg]	3.70E+06	1.42E+07
Raw material fraction	98%	98%
Solar park area in [m²]	2.20E+07	8.52E+07
Power capacity in [MW]	2.69E+03	1.04E+04
Total mass of support structure in [kg]	2.67E+06	1.02E+07
In-situ material mass fraction	0%	0%
Terrestrial mass of support structure in [kg]	2.67E+06	1.02E+07
Supercapacitor mass in [kg]	2.25E+05	8.64E+05
Terrestrial mass of lunar solar park in [kg]	2.64E+04	3.92E+05
Total mass of coilgun and infrastructure in [kg]	**6619123**	**25663988**

Table 19: Total mass estimation for multiple lunar coilguns and infrastructure to achieve required raw material MLR. Mass fraction of lunar solar park based on lunar solar park area A and a terrestrial mass fraction of 0.1%. Calculated without in-situ material mass fraction.

Assuming a Starship payload capacity of 100 t per launch, this would result in 67 launches for the minimum mass sunshade and 257 launches for the photovoltaic sunshade. The number of required coilguns to perform at the required launch rate per hour varies between 12 and 46. It should be noted that the support infrastructure is provided

entirely from Earth. Assuming 90% in-situ resource utilization for simple structures, the required total mass will be reduced to 4,214 t and 16,444 t (Table 20).

	Minimum Mass Sunshade	Photovoltaic Sunshade
Raw material MLR in [kg/h]	4.21E+05	1.63E+06
Required launches per hour with $m_{Payload}$ = 100 kg	4210	16320
Launch time in [s]	0.53	0.53
Estimated launch preparation time in [s]	10	10
Number of coilguns	12	46
Possible launches per coilgun per hour	360	360
Accelerator mass in [kg]	3.70E+06	1.42E+07
Raw material fraction	98%	98%
Solar park area in [m²]	2.20E+07	8.52E+07
Power capacity in [MW]	2.69E+03	1.04E+04
Total mass of support structure in [kg]	2.67E+06	1.02E+07
In-situ material mass fraction	90%	90%
Terrestrial mass of support structure in [kg]	2.67E+05	1.02E+06
Supercapacitor mass in [kg]	2.25E+05	8.64E+05
Terrestrial mass of lunar solar park in [kg]	2.64E+04	3.92E+05
Total mass of coilgun and infrastructure in [kg]	**4213963**	**16444208**

Table 20: Total mass estimation for multiple lunar coilguns and infrastructure to achieve required raw material MLR. Mass fraction of lunar solar park based on lunar solar park area A and a terrestrial mass fraction of 0.1%. Calculated with in-situ material mass fraction of 90%.

Overall cost estimation

For an initial cost estimation, the budget of the Defense Advanced Research Projects Agency (DARPA) EMM program for the development of an electromagnetic launcher is considered. However, it should be noted that the EMM program included the development of a coilgun as well as a railgun version including the development costs for a sufficient power supply. Based on a cost framework of $5 million dollars for a 2.4 m EMM accelerator including energy supply, a conservative scaling to the LC accelerator length of 689 m would result in US$1.413 billion dollars. Based on the assumptions already mentioned in chapter 5.1 for Starship, a payload cost of US$1400 per kg results in a launch cost for the masses of a coilgun and the associated infrastructure between US$773 million and US$781 million. Considering the overall concept to achieve the necessary MLR (Table 21), the total system consisting of multiple coilguns and the associated infrastructure with a 90% in-situ resource utilization will cost between US$23.245 and US$89.129 billion.

	Minimum Mass Sunshade	Photovoltaic Sunshade
Raw material MLR in [kg/h]	4.21E+05	1.63E+06
Total mass of coilgun and infrastructure in [kg]	4.21E+06	1.64E+07
Number of LC	12	46
Scaled cost per LC system in [US$ million]	1,435	1,435
Total LC system cost in [US$ million]	17,225	66,029
Number of Starship launches	43	165
Payload per Starship launch in [kg]	1.00E+05	1.00E+05
Starship payload cost in [US$/kg]	1.40E+03	1.40E+03
Launch cost in [US$ million]	6,020	23,100
Total cost in [US$ billion]	23.245	89.129

Table 21: Total cost estimation for multiple lunar coilguns and infrastructure to achieve required raw material MLR. Calculated with capabilities of Starship and with in-situ material mass fraction of 90%.

5.3 Solar and Laser-Beam Sails

Conventional propulsion technologies are based on the opposing momentum of the accelerated onboard reaction mass, which is accelerated to high velocities using chemical reactions or electromagnetic forces [87]. The use of solar sails exploiting solar pressure eliminates the reliance on propellant as reaction mass. By harnessing the momentum of photons, continuous unlimited acceleration is achievable, depending only on the lifetime of the applied sail film. Thus, they have the potential to extend the envelope of possible missions and to enable high-energy missions. However, solar sailing utilizing large reflective surface areas provides only a maximum low-thrust transfer capability of 9 $\frac{\mathrm{N}}{\mathrm{km}^2}$ at a distance of one astronomical unit (AU) [139]. The primary objective of a solar sail design is to provide large reflective surfaces with minimal mass. Especially for terrestrial solar sails, sufficient deployment reliability and production ease have to be balanced. In addition, the thin surface has to be tensioned to reduce the ripples and to provide a smooth surface. For this purpose, methods like booms or spars can be used to tension the sail.

The configuration with booms attached to a central node allows the controlled deployment of the sails, whereby the central unit can be jettisoned after successful furling in order to reduce system mass. With respect to the AOCS, articulated reflector blades at the boom ends provide a simple but slow method to relocate reflective area fraction. A faster but more complicated method is to displace the center of mass or the center of

pressure of the spacecraft. The displacement of the center of mass is performed by attaching an additional mass to a boom, which is normal to the sail surface. The active relocation of the mass results in a shift of the center of mass, whereby a complex harmonization of the operations is mandatory and the probability of failure is high. In addition, a certain bending stiffness of the boom has to be ensured, which results in a high mass fraction of the sail. Furthermore, the concept is challenging in terms of packing and deployment. The alternative displacement of the center of pressure is achieved by a non-uniform distribution of the sail area through retraction and deployment.

The concept using centripetal force provides for a heligyro configuration. The sail consists of long blades attached to a central node. By rotation, the blades are deployed and stabilized autonomously, eliminating the need for heavy spars. The configuration offers more compact packing and deployment. Stabilization is achieved by spin, implementing the AOCS by varying the blade pitch across the rotation. Due to the rotation, the blades must be stiffened appropriately with respect to aging by twist.

A hybrid concept combines the two configurations in the form of a disc sail deployed from a central node. Radial booms support the sail to achieve stiffness, while their elastic energy, induced by the initial wrapping process, provides the necessary assistance during the deployment.

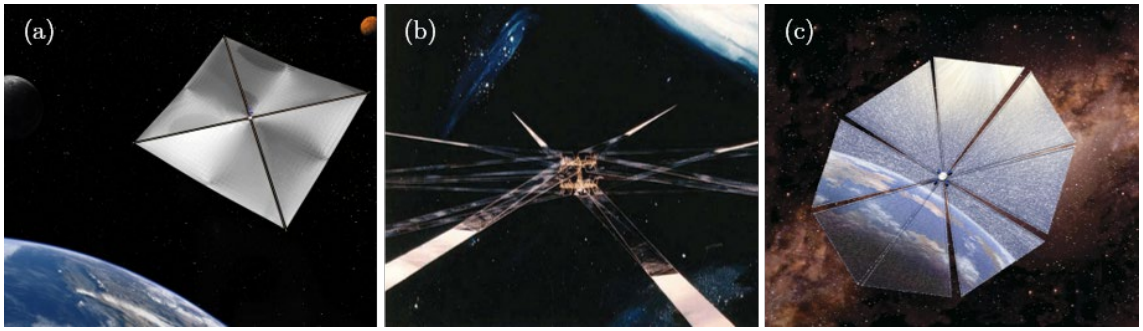

Figure 35: Solar sail configurations.(a) Square sail [140].(b) Heliogyro Sail [141].(c) Spinning Disc Sail [142].

This promising technology has already been applied in a large number of missions (Table 22). The Japanese Interplanetary Kite-craft Accelerated by Radiation Of the Sun (IKAROS) mission has already performed a successful orbit transfer using solar sails in 2010. In 2019, LightSail 2 was able to demonstrate solar pressure-based orbit stabilization in LEO. NASA's Near-Earth Asteroid (NEA) Scout, a CubeSat with solar sail propulsion will be launched into lunar orbit in 2021 to study a near-Earth asteroid. The largest project planned so far, the Solar Cruiser, with an area of 1,650 m^2 is targeting an artificial

Lagrange point between Sun and Earth. Mission objectives are solar science and a warning system to prevent damages on satellites by solar storms. Solar Cruiser will provide a crucial baseline for the stabilization of large-scale sunshades around SEL_1, as well as the sail design and production capabilities. The use of solar sails for the low-thrust transfer between EML_2 and SEL_1 will require large sail structures due to the high masses involved.

NanoSail-D	IKAROS	LightSail-1	CU Aerospace	LightSail-2	Near Earth Asteroid Scout	Solar Cruiser
2010	2010	2015	2018	2019	2021	2025
NASA	JAXA	The Planetary Society	NASA	The Planetary Society	NASA	NASA
EOD only	IFF	EOD only	EOFF	EOFF	IFF	IFF
3U CubeSat	315 kg Smallsat	3U CubeSat	3U CubeSat	3U CubeSat	6U CubeSat	-
10 m^2	196 m^2	32 m^2	20 m^2	20 m^2	86 m^2	1,672 m^2

Table 22: Overview of selected solar sail missions. EOD = Earth orbit deployment, IFF = Interplanetary Full Flight, EOFF = Earth orbit full flight.

Due to the large efforts in connection with solar sails, they will be available for near-term applications. An extension of the potential is provided by laser powered sails [144], which obtain additional ΔV from a directed laser. The energy could be provided for example by a laser on Earth, but high energy dissipation due to the atmosphere has to be accepted. An alternative would be solar power satellites, which could transmit bundled energy to the sail. Laser beam sails were not yet tested but could offer a time-efficient possibility for interstellar travel [144]. The current state of the art indicates that initially solar sails must be optimized in terms of surface density as well as scale through effective designs and material selection in order to enable the next leap to laser powered sails (Figure 37).

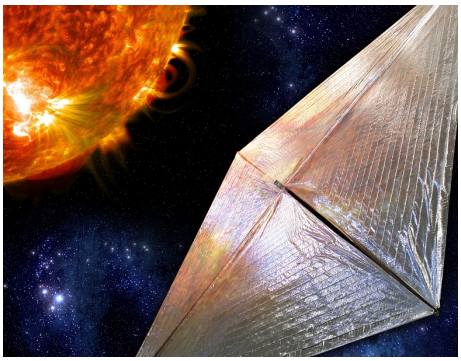

Figure 36: Solar Cruiser [143].

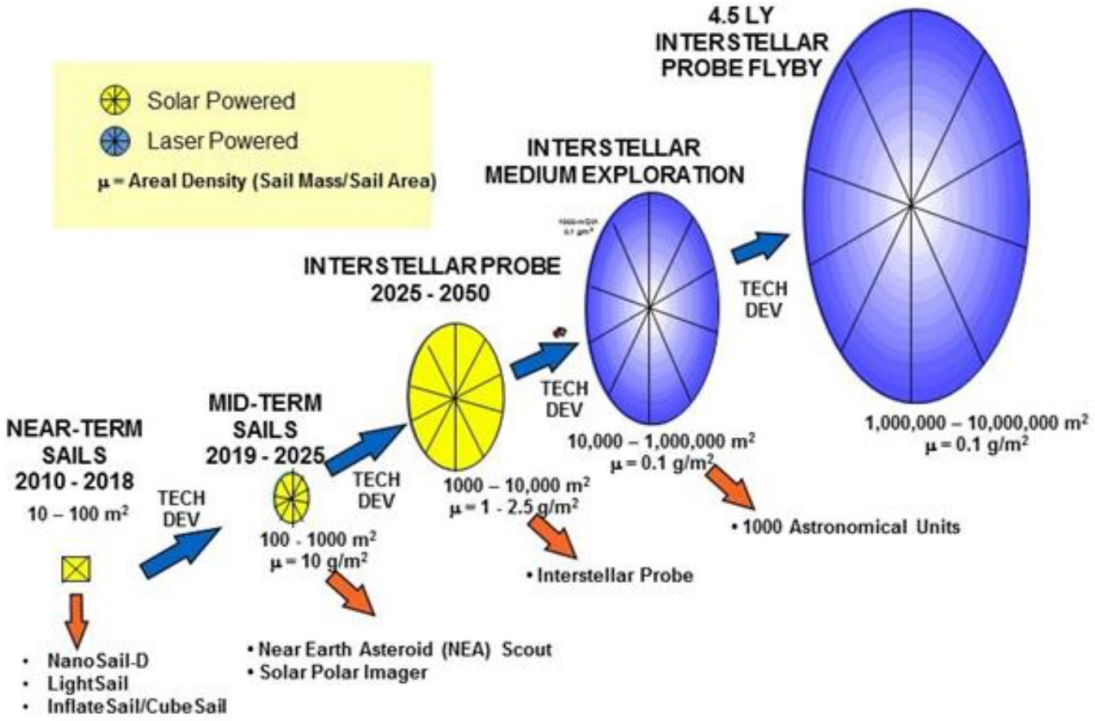

Figure 37: Roadmap for solar and laser powered sails [145].

6 IPSS Attitude and Orbit Control System

In the following chapter, the technological possibilities for an IPSS Attitude and Orbit Control System with respect to stabilization and controllability at SEL_1 are shortly discussed. Based on the defined requirements, a possible concept based on IKAROS is presented.

6.1 Requirements

The designed IPSS system consists of a high number of smaller sunshades, which have to be arranged in a formation around SEL_1 and stabilized to achieve a uniform shading effect on Earth. Thus, there are different requirements for the AOCS, resulting as the baseline for the further design.

The AOCS must be able to apply sufficient momentum to ensure the stabilization of the orbit. The orbit selection should be based on its stability as well as its capability to be mapped accurately in simple models, while the transfer to high-fidelity models should not result in significant displacements. Due to the constant orientation towards the Sun, a continuous solar pressure can be assumed, but a mutual shading of the individual sunshades can occur. Therefore, a complex formation model must be created and simulated for an accurate representation of these effects on the orbit as well as the shading. Consequently, the AOCS concept has to be mapped in terms of its attitude dynamics. In addition, the concept must ensure continuous control and enable infrequent control maneuvers.

6.2 System Architecture

The use of solar sails allows to generate artificial Lagrange points in the CR3BP of the Sun-Earth system by accelerating constantly. For this purpose, in addition to the existing centripetal force in the rotating Sun-Earth frame, the force induced by the solar radiation pressure is directed in the opposite direction to the Sun to provide a constant counterthrust. Thus, artificial Lagrange points can be generated between SEL_1 and the

Sun, as well as between SEL_2 and Earth. These artificial Lagrange points can serve as the reference point for halo orbits, which can be stabilized with little ΔV.

The sunshades are positioned in different layers along the connecting line between the Sun and Earth, whereby the spacing between the layers must be large enough to avoid overlapping of the three-dimensional motions of the sunshades between two different layers. Thus, the entire fleet of sunshades is divided into several groups, which remain in their respective motion areas without interfering with each other. Hereby the communication and control efforts are reduced. The exact definition of the layers as well as the spatial dimension of the occupied space of the sunshade formation, moving on periodic orbits around the respective artificial Lagrange point, has to be simulated.

Tracking has to be performed centrally from the hub at SEL_1 in order to coordinate the sunshades. Due to the high number of sunshades, a complex dynamic system results, which has to be propagated with in high-fidelity models in order to avoid collisions and to initiate evasive maneuvers. Due to the lack of impulsive maneuvers, avoidance maneuvers can only be performed with low thrust, which limits the time response and the possible stable trajectories that can be reached.

Control Mechanism

The orbit control can be performed either by an area variation or an angle variation. The required area variation increases with increasing distance from Earth because higher counterforces are necessary. Based on the values simulated by Bookless [146] (Table 23), an estimation for the ΔV-demand can be derived.

	Around SEL_1	Around SEL_A
Position in [km]	1,530,720	2,487,420
Sail-to-payload ratio	2%	30%
ΔV-demand in $[\frac{\mathrm{m}}{\mathrm{s}}]$	395	6,184
Sunshade size	small	large

Table 23: Estimations for sunshade size based on Bookless [146] simulations.

Based on the scaled ΔV-demand and the corresponding surface area, it becomes evident that larger sunshades should be positioned closer to the Sun, because they can provide a higher surface area variation to stabilize the orbit. Due to TRL and time constraints the first sunshades will be smaller and should be located closer to SEL_1 in order to manage initially with low ΔV-demands and the associated control maneuvers.

Control Design

IKAROS is the only mission to date which used solar sails as the primary propulsion technology for an orbital transfer. The spin stabilized spacecraft was equipped with a 20 m-span sail with a mass of 16 kg and a minimum thickness of 7.5 µm. The centrifugal force-based deployment mechanism enabled a low sail mass with simple support structure.

A similar design of fuel-free and oscillation-free attitude control system as for IKAROS is intended for the sunshades. The use of thin-film-type devices, called reflectance control device (RCD) [147], enables the center of radiation pressure to be displaced from the center of mass by adjusting local optical properties at the sail edges. Thus, a torque normal to the spin axis can be generated. The RCD controls the orientation of liquid crystal components, which are sandwiched between two electrodes. By applying voltage between the applied electrodes, regular and diffuse transmission can be switched. By distributing multiple RCDs over the sail area, the torque can be transferred to the entire sail compared to classical reaction control systems (RCS). Due to the constant torque, a stable attitude control of the large sail structures can be implemented. Figure 38 illustrates the torque generation by local variation of the optical properties between specular and diffuse reflectivity.

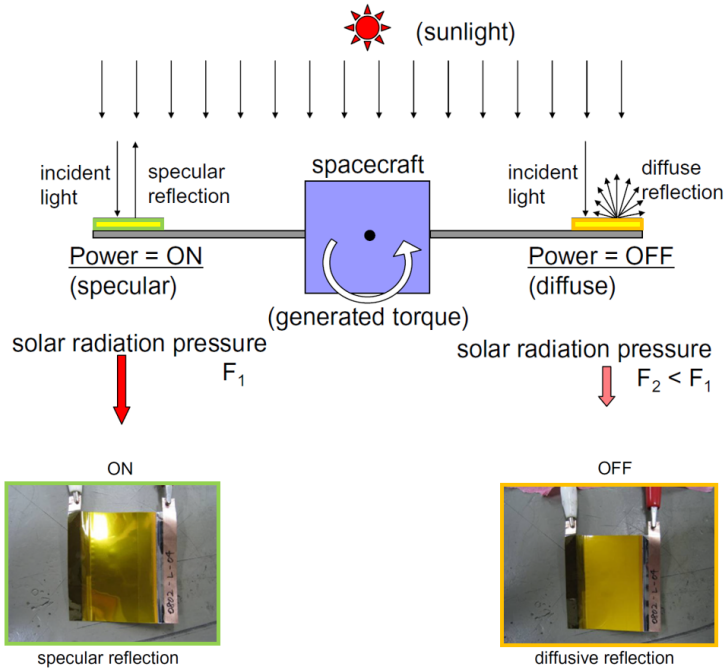

Figure 38: Functionality of SRP-based attitude control using RCDs for torque generation [148].

The design of the exact number of RCDs depends on the size of the sunshade and the required area variation to generate the torque for stabilization. The generated torque depends on the device performance ΔP_{RCD}, which results from the difference of the solar radiation pressure in the ON ($P_{RCD,ON}$) and OFF ($P_{RCD,OFF}$) states (Eq. 15).

$$\Delta P_{RCD} = P_{RCD,ON} - P_{RCD,OFF} \qquad \text{(Eq. 15)}$$

The performance in the two states is obtained from the following integrals (Eq. 16 and Eq. 17) regarding the wave-dependent reflectivity (Figure 39). C_A, C_S and C_D represent the absorptivity, the specular reflectivity, and the diffuse reflectivity in the respective states, which depend on the wavelength λ. The torque of the sunlight per unit wavelength per unit area is given by p_0 and the angle to the sun by θ. Based on experiments, C_A remains constant in both states [148], therefore ΔP_{RCD} is only depending on the difference of the specular reflectivity ΔC_S and the diffuse reflectivity ΔC_D (Eq. 18).

$$P_{RCD,ON} = \int p_0 \left(\cos^2\theta \cdot C_{A,ON} + 2\cos^2\theta \cdot C_{S,ON} + \cos^2\theta \cdot C_{D,ON} + \tfrac{2}{3}\cos\theta \cdot C_{D,ON}\right) d\lambda \qquad \text{(Eq. 16)}$$

$$P_{RCD,OFF} = \int p_0 \left(\cos^2\theta \cdot C_{A,OFF} + 2\cos^2\theta \cdot C_{S,OFF} + \cos^2\theta \cdot C_{D,OFF} + \tfrac{2}{3}\cos\theta \cdot C_{D,OFF}\right) d\lambda \quad \text{(Eq. 17)}$$

$$\Delta P_{RCD} = \int p_0 \cos\theta \left(2\cos\theta \cdot \Delta C_S + \left(\tfrac{2}{3} + \cos\theta\right) \cdot \Delta C_D\right) d\lambda \quad \text{(Eq. 18)}$$

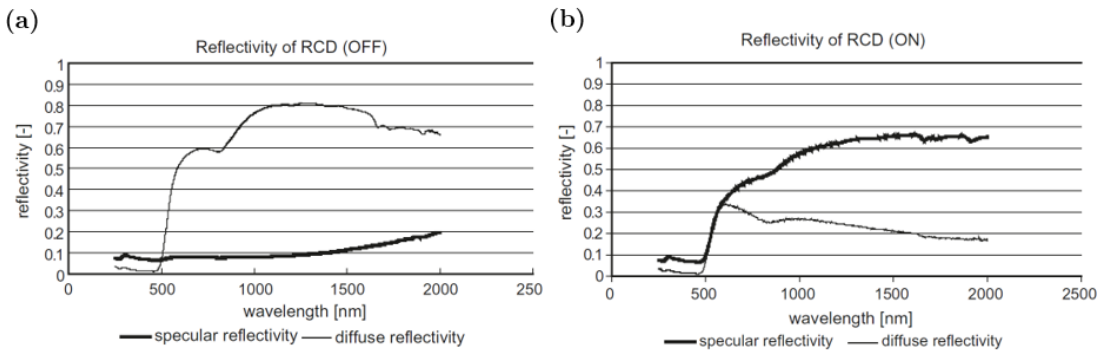

Figure 39: Specular and diffuse reflectivity of RCD. (a) Reflectivity in state ON. (b) Reflectivity in state OFF.

The time-averaged attitude torque $\bar{T}$ (Figure 40) can be derived according to (Eq. 19) from the total area A_{RCD} of the RCDs, the distance R_{RCD} of the individual RCDs to the center of the spacecraft and ΔP_{RCD}.

$$\bar{T} = \frac{A_{RCD}\Delta P_{RCD} R}{\pi} \quad \text{(Eq. 19)}$$

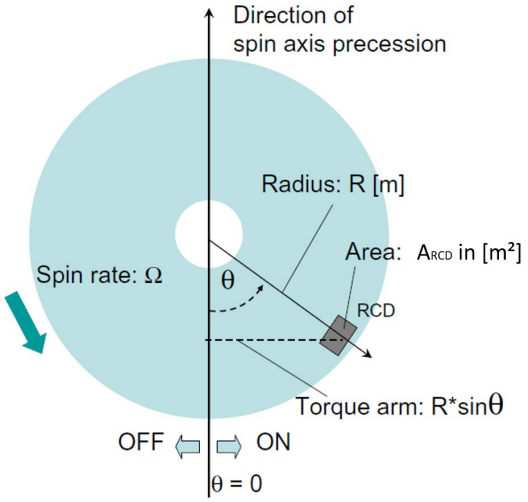

Figure 40: Attitude torque generation by a single RCD.

7 Conclusion

The primary objective of this thesis was the analysis of the logistical aspects of constructing a sunshade constellation, the IPSS system, in the vicinity of SEL_1. Based on the defined roadmap for the development and implementation of the IPSS system, the transfer trajectories for the different phases in the Sun-Earth-Moon system were characterized and designed. Furthermore, the required transport technologies were analyzed and partly conceptualized. Finally, aspects for an IPSS attitude and orbit control system were highlighted to ensure stabilization of the IPSS constellation around SEL_1.

Based on the overall roadmap, the logistical concept for the IPSS system was designed and described first. Based on the required mass flow between the defined destination points, appropriate and phase-specific effective transfer technologies were selected and their significance and application for the phase were outlined.

In the first step, the trajectories were differentiated between Earth-based, Moon-based, and lunar orbit-based trajectories with respect to their targeted destination, the available transfer technologies as well as the required ΔV-demand. The target orbits for the Earth-based transfers were identified, which are initially exploited to test the required technology demonstrators in Earth orbit and finally to demonstrate the functionality of an Earth-built sunshade demonstrator at SEL_1.

A special focus was assigned to the lunar-based trajectories to transport the initial resources to the Moon as well as to ensure a continuous supply of Earth-based components to the cargo hub. The choice of a suitable orbit for the cargo hub at EML_2 was investigated in terms of ΔV-demand, stability, and visibility to the lunar south pole region. With an optimization tool, a short-term transfer with a *TOF* of 5.5 days for manned missions and an energy-efficient long-term transfer with a *TOF* of 59.5 days for cargo missions to a NRHO with a comparable stability as the Lunar Gateway orbit were designed. Subsequently, visibility of the NRHO at the lunar south pole, especially the Shackleton crater, was analyzed with the LSMAT tool to identify possible communication windows between the lunar base and the cargo hub. The results indicate a maximum coverage of 92%, with the area around the Shackleton crater being covered between 85% and 90%. Hence, the coverage level is similar to the visibility of the gateway orbit. Following that, the challenges for a low-thrust transfer based on solar sails between the

Lagrange points EML_2 and SEL_1 were presented in order to finalize a ΔV-mapping for the whole mission scenario.

The second section analyzed suitable propulsion and launch technologies. Chemical reusable rockets, such as the Starship, have emerged as a promising technology for Earth-based transfers. For the high mass transfer from the lunar south pole to EML_2 a scalable modular coilgun concept was designed taking advantage of the lunar conditions at the Shackleton crater. Based on the key performance parameters of the coilgun, a first mass and energy balance based on lunar silicon solar cells was established and a rough cost estimate was derived. The energy demand indicates that a large lunar solar park in the order of magnitude of the largest solar park on Earth, the Bhadla Solar Park, is required. The mass estimate reveals that, depending on the sunshade concept, 12 to 46 coilguns are required to provide the demanded mass flow of 74 to 286 Mt to SEL_1. The initial cost estimate for a lunar launch system based on multiple coilguns is between US$23 and US$89 billion. The further transport of the cargo blocks is carried out by using a solar sail propulsion system, which has been investigated with regard to its potential application in combination with laser powered sailing.

Finally, the IPSS attitude and orbit control system was analyzed with respect to an efficient stabilization of the sunshade constellation at SEL_1. In this context, an orbit and attitude stabilization based on RCDs was investigated in order to ensure uniform and continuous attitude control. Based on previous simulation results, positioning of smaller sunshades closer to SEL_1 should be intended in order to provide the required area variation. The complexity of the low-thrust AOCS and the dynamics of the orbits around SEL_1 require a high-fidelity model to estimate the effects of mutual shading and the effort for control maneuvers.

8 Outlook

A great venture requires initiating small steps in order to be accomplished. The present analyses of the logistical aspects of an IPSS system provide initial estimates with regard to potential transfer trajectories as well as propulsion and launch systems. The analysis of the trajectories especially in connection with the Lagrange points SEL_1 and EML_2 shows high optimization potentials. The simple transfer trajectories in the CR3BP have to be transformed into a high-fidelity model in order to be able to design potential deviations with regard to ΔV-requirements as well as stabilization efforts for the AOCS. In addition, the low-thrust transfer with solar sails has to be simulated in more detail to define possible limits for the space tugs transporting cargo from EML_2 to SEL_1.

Another task in the design of the AOCS will be the manufacturing and especially the maintenance operations at SEL_1, which will require a large number of robotic operations. The stabilization of the on-orbit assembly process of large structures has to be analyzed with respect to induced external disturbances by the movements of the assembly robots and corresponding control methods have to be implemented to prevent uncontrolled drifting on the one hand and to reduce control allocation on the other hand [149].

The coilgun concept is a promising launch technology, however, the high energy and mass input requires optimization. Alternative concepts, such as a ring-shaped structure in combination with directing tubes, should be analyzed more closely in order to reduce the high number of coilguns. The use of solar power satellites at SEL_1 in combination with laser-based energy transmission could accelerate the implementation by reducing energy consumption, but this technology is not yet sufficiently researched. Alternatively, an increase in efficiency of the lunar solar cells would allow a reduction of the required solar park area. The conservative calculation of the key design parameters of the coilgun system can be optimized by a detailed model. At the same time, current results in superconducting technology must be included to enable more efficient energy storage and transmission.

The current design of the coilgun is limited to use for the high mass transport of raw materials. Further use of the coilgun with adaptable accelerations could enable a future technology for lunar transportation. For this purpose, additional use-cases as well as the

necessary requirements, should be analyzed in order to derive a modular design for different objectives.

One of the biggest challenges is the design, optimization, and control of the sunshade constellation at SEL_1. Due to the high number of sunshades, an instantaneous coordination of their motion as well as an avoidance of mutual shadowing has to be ensured. The use of a laser-aided control system at SEL_1 for active trajectory and attitude control could provide additional relief and should be considered for the formation design.

Due to the logistical complexity of the overall system, an extension of the designed concepts to a model-based approach for the IPSS system can enable systematic design (Figure 41). For this purpose, the overall system is divided into parameterized subsystems for the individual fields of the IPSS system. These, in turn, are clustered into relevant optimization fields, so that a cross-linking of the subsystems can enable optimization regarding different priorities. Especially the logistical model should be able to represent the transfer optimization, the design of the mega constellation, as well as the shading impact on Earth. By integrating the ISRU and ISM models in combination with a detailed sunshade model, a realistic simulation of the implementation and operation can be achieved. The crucial coupling with a sophisticated climate model provides a holistic system that could be used to demonstrate the promising impact of an IPSS system on climate change.

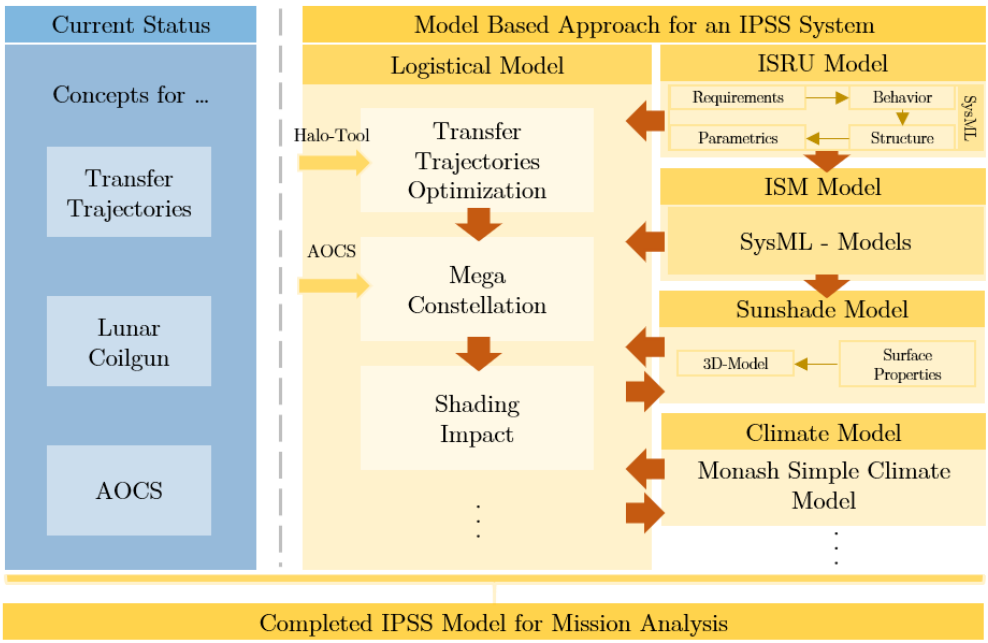

Figure 41: Model-based approach for an IPSS system.

Despite increasing efforts and financial support through private companies, an international alliance is necessary to achieve climate goals as well as efficient reduction of global warming. The promotion of innovative concepts by private investors [150; 151] in cooperation with international organizations can enable an efficient development of an IPSS system to cope with the impacts of climate change until 2060 and beyond. In addition to the organizational and legal aspects of an IPSS system, national responsibilities concerning climate change are essential [152]. The IPSS system thus not only provides the opportunity to achieve a global reduction of climate change in order to secure the future of mankind; but it could also initiate the first steppingstone towards a sustainable era of international spaceflight by driving international cooperation and competition as well as by extending international frameworks for lunar settlements [153] and even beyond.

9 Literature References

[1] United Nations, Security Council, Press Release: *Climate Change 'Biggest Threat Modern Humans Have Ever Faced', World-Renowned Naturalist Tells Security Council, Calls for Greater Global Cooperation: Meetings Coverage and Press Releases.* Website: https://www.un.org/press/en/2021/sc14445.doc.htm [accessed: 31.03.2021]

[2] Bhatia, Kieran T.; Vecchi, Gabriel A.; et al.: *Recent increases in tropical cyclone intensification rates,* Nature communications, 10, Nr. 1, 2019, S. 635

[3] Anderson, Jason; Bausch, Camilla: *Climate Change and Natural Disasters: Scientific evidence of a possible relation between recent natural disasters and climate change,* Policy Department Economic and Scientific Policy, 2, 2006

[4] Lenton, T. M.; Vaughan, N. E.: *The radiative forcing potential of different climate geoengineering options,* Atmospheric Chemistry and Physics, 9, Nr. 15, 2009, S. 5539–5561

[5] Collins, Matthew; Knutti, Reto; et al.: Long-term climate change : Projections, commitments and irreversibility. In: *Climate Change 2013-The Physical Science Basis: Contribution of Working Group I to the Fifth Assessment Report of the Intergovernmental Panel on Climate Change:* Cambridge University Press, 2013, S. 1029–1136

[6] Mäder, Claudia; Umweltbundesamt, Deutschland: *Kipp-punkte im Klimasystem: welche Gefahren drohen?,* Umweltbundesamt, 2008

[7] Gielen, Dolf; Boshell, Francisco; et al.: *The role of renewable energy in the global energy transformation,* Energy Strategy Reviews, 24, Nr. 6, 2019, S. 38–50

[8] International Renewable Energy Agency: *Global Energy Transformation: A Roadmap to 2050*

[9] Dommenget, Dietmar; Nice, Kerry; et al.: *The Monash Simple Climate Model experiments (MSCM-DB v1. 0): an interactive database of mean climate, climate change, and scenario simulations,* Geoscientific Model Development, 12, Nr. 6, 2019, S. 2155–2179

[10] Warren, R.; Andrews, O.; et al.: *Risks associated with global warming of 1.5 C or 2 C,* Briefing Note, Tyndall Centre for Climate Change Research, UK, 2018

[11] Bindi, M.; Brown, S.; et al.: *impacts of 1.5° C of global warming on natural and human systems,* IPCC: Geneva, Switzerland, 2018

[12] Lindsey Rebecca, Dahlman LuAnn: *Climate Change: Global Temperature.* Website: https://www.climate.gov/news-features/understanding-climate/climate-change-global-temperature [accessed: 31.03.2021]

[13] S. Fix: *Feasibility study of a sunshade in the vicinity of the Sun Earth L1 Lagrange Point (IRS-21-S-006).* University of Stuttgart, Institute of Space Systems, Master Thesis, 2021.

[14] Alessi, Elisa Maria; Gómez, Gerard; et al.: *Two-manoeuvres transfers between LEOs and Lissajous orbits in the Earth–Moon system,* Advances in Space Research, 45, Nr. 10, 2010, S. 1276–1291

[15] Gordon, Dawn Perry: *TRANSFERS TO EARTH-MOON L2 HALO ORBITS.* Purdue University West Lafayette, 2008.

[16] Szebehely, V.: *Theory of Orbits, The Restricted Problem of Three Bodies, Acad,* Press, New York, 1967

[17] Renk, F.; Hechler, M.; Messerschmid, E.: *Exploration missions in the Sun–Earth–Moon system: A detailed view on selected transfer problems,* Acta Astronautica, 67, 1-2, 2010, S. 82–96

[18] Koon, Wang Sang; Lo, Martin W.; et al.: Dynamical Systems, the Three-Body Problem and Space Mission Design. In: Fiedler, Bernold; Gröger, Konrad; Sprekels, Jürgen (Hrsg.): *Equadiff 99:* World Scientific Publishing Company, 2000, S. 1167–1181

[19] Domingo, V.; Fleck, B.; Poland, A. I.: *The SOHO mission: An overview,* Solar Physics, 162, 1-2, 1995, S. 1–37

[20] Roberts, Craig E.: *Long term missions at the Sun-Earth libration point L1: Ace, SOHO, and WIND,* 2011

[21] Peiris, Hiranya V.; Komatsu, E.; et al.: *First-year Wilkinson microwave anisotropy probe (WMAP)* observations: Implications for inflation,* The Astrophysical Journal Supplement Series, 148, Nr. 1, 2003, S. 213

[22] Collaboration, Planck: *The Scientific programme of planck,* arXiv preprint astro-ph/0604069, 2006

[23] Gardner, Jonathan P.; Mather, John C.; et al.: *The james webb space telescope,* Space Science Reviews, 123, Nr. 4, 2006, S. 485–606

[24] Neil, C. J.: *The Lagrange Points,* Cornish Document Created for WMAP Education and Outreach, 1998

[25] Whitley, Ryan; Martinez, Roland: *Options for staging orbits in cislunar space,* IEEE, 2016

[26] Parker, Jeffrey S.; Anderson, Rodney L.: *Low-energy lunar trajectory design,* John Wiley & Sons, 2014

[27] Farquhar, Robert Willard: *The utilization of halo orbits in advanced lunar operations,* National Aeronautics and Space Administration, 1971

[28] Canalias, E.; Gomez, G.; Marcote, M.; Masdemont, J. J.: *Assessment of mission design including utilization of libration points and weak stability boundaries,* ESA Advanced Concept Team, 2004

[29] Le Bihan, Bastien; Kokou, Pierre; Lizy-Destrez, Stéphanie: *Computing an optimized trajectory between Earth and an EML2 halo orbit,* 2014

[30] Lo, Martin; Ross, Shane: *The Lunar L1 Gateway: Portal to the stars and beyond,* 2001

[31] Lo, Martin; Chung, Min-Kun: *Lunar sample return via the interplanetary superhighway,* 2002

[32] Grebow, Daniel: *Generating periodic orbits in the circular restricted three-body problem with applications to lunar south pole coverage,* MSAA Thesis, School of Aeronautics and Astronautics, Purdue University, 2006

[33] Hamera, Kathryn; Mosher, Todd; et al.: An Evolvable Lunar Communication and Navigation Constellation Architecture. In: *26th International Communications Satellite Systems Conference (ICSSC).* Reston, Virigina: American Institute of Aeronautics and Astronautics, 2008

[34] Howell, Kathleen C.; Kakoi, Masaki: *Transfers between the Earth–Moon and Sun–Earth systems using manifolds and transit orbits,* Acta Astronautica, 59, 1-5, 2006, S. 367–380

[35] Mingtao, Li; Jianhua, Zheng: *Impulsive lunar Halo transfers using the stable manifolds and lunar flybys,* Acta Astronautica, 66, 9-10, 2010, S. 1481–1492

[36] Davis, Kathryn E.; Anderson, Rodney L.; Scheeres, Daniel J.; Born, George H.: *Optimal transfers between unstable periodic orbits using invariant manifolds,* Celestial Mechanics and Dynamical Astronomy, 109, Nr. 3, 2011, S. 241–264

[37] Howell, K. C.; Breakwell, J. V.: *Almost rectilinear halo orbits,* Celestial Mechanics and Dynamical Astronomy, 32, Nr. 1, 1984, S. 29–52

[38] Davis, Diane; Bhatt, Sagar; et al.: *Orbit maintenance and navigation of human spacecraft at cislunar near rectilinear halo orbits,* 2017

[39] Guzzetti, Davide, et al: *Stationkeeping analysis for spacecraft in lunar near rectilinear halo orbits,* AAS Marriott Plaza, Texas, 2017

[40] Gerstenmaier, William ; Crusan, Jason: *Cislunar and Gateway Overview.* Website: https://www.nasa.gov/sites/default/files/atoms/files/cislunar-update-gerstenmaier-crusan-v5a_tagged_0.pdf [accessed: 31.03.2021]

[41] Williams, Jacob; Lee, David E.; et al.: *Targeting cislunar near rectilinear halo orbits for human space exploration,* 2017

[42] Caldeira, Ken; Bala, Govindasamy; Cao, Long: *The Science of Geoengineering,* Annual Review of Earth and Planetary Sciences, 41, Nr. 1, 2013, S. 231–256

[43] Irvine, Peter J.; Ridgwell, Andy; Lunt, Daniel J.: *Climatic effects of surface albedo geoengineering,* Journal of Geophysical Research: Atmospheres, 116, D24, 2011, n/a-n/a

[44] Ridgwell, Andy; Singarayer, Joy S.; et al.: *Tackling regional climate change by leaf albedo bio-geoengineering,* Current biology : CB, 19, Nr. 2, 2009, S. 146–150

[45] Akbari, Hashem; Menon, Surabi; Rosenfeld, Arthur: *Global cooling: Increasing worldwide urban albedos to offset CO2,* Climatic Change, 94, 3-4, 2009, S. 275–286

[46] Pidwirny, M.: *Introduction to the Oceans. Fundamentals of Physical Geography, Date Viewed: 2013 March: Introduction to the Oceans. Fundamentals of Physical Geography, Date Viewed: 2013 March,* 2006

[47] Seitz, Russell: *Bright water: Hydrosols, water conservation and climate change,* Climatic Change, 105, 3-4, 2011, S. 365–381

[48] Latham, John; Bower, Keith; et al.: *Marine cloud brightening,* Philosophical transactions. Series A, Mathematical, physical, and engineering sciences, 370, Nr. 1974, 2012, S. 4217–4262

[49] Latham, John; Gadian, Alan; et al.: *Marine cloud brightening: regional applications,* Philosophical transactions. Series A, Mathematical, physical, and engineering sciences, 372, Nr. 2031, 2014

[50] Rasch, Philip J.; Tilmes, Simone; et al.: *An overview of geoengineering of climate using stratospheric sulphate aerosols,* Philosophical transactions. Series A, Mathematical, physical, and engineering sciences, 366, Nr. 1882, 2008, S. 4007–4037

[51] Robock, Alan: CHAPTER 7. Stratospheric Aerosol Geoengineering. In: Harrison, Roy; Hester, Ron (Hrsg.): *Geoengineering of the Climate System.* Cambridge: Royal Society of Chemistry, 2014, S. 162–185

[52] Halstead, John: *Stratospheric aerosol injection research and existential risk,* Futures, 102, Nr. 5615, 2018, S. 63–77

[53] Ahlm, Lars; Jones, Andy; et al.: *Marine cloud brightening – as effective without clouds,* Atmospheric Chemistry and Physics, 17, Nr. 21, 2017, S. 13071–13087

[54] Shepherd, John: *Geoengineering the climate: Science, governance and uncertainty,* London, The Royal Society, 2009

[55] Smith, Wake: *The cost of stratospheric aerosol injection through 2100,* Environmental Research Letters, 15, Nr. 11, 2020, S. 114004

[56] Bewick, R.; Lücking, C.; Colombo, C.; Sanchez, J. P.; McInnes, C. R.: *Heliotropic dust rings for Earth climate engineering,* Advances in Space Research, 51, Nr. 7, 2013, S. 1132–1144

[57] Pearson, Jerome; Oldson, John; Levin, Eugene: *Earth rings for planetary environment control,* Acta Astronautica, 58, Nr. 1, 2006, S. 44–57

[58] Struck, Curtis: *The Feasibility of Shading the Greenhouse with Dust Clouds at the Stable Lunar Lagrange Points,* J British Interplanetary Society, 2007

[59] Walter Seifritz: *Mirrors to halt global warming?,* Nature, 1989

[60] Sánchez, Joan-Pau; McInnes, Colin R.: *Optimal Sunshade Configurations for Space-Based Geoengineering near the Sun-Earth L1 Point,* PloS one, 10, Nr. 8, 2015, e0136648

[61] Lenton, T. M.; Vaughan, N. E.: *The radiative forcing potential of different climate geoengineering options,* Atmospheric Chemistry and Physics, 9, Nr. 15, 2009, S. 5539–5561

[62] Early, James T.: *Space-based solar shield to offset greenhouse effect,* Journal of the British Interplanetary Society, 42, 1989, S. 567–569

[63] Seifritz, Walter: *Mirrors to halt global warming?,* Nature, 340, Nr. 6235, 1989, S. 603

[64] McInnes, Colin R.: *Minimum mass solar shield for terrestrial climate control,* Journal of the British Interplanetary Society, 55, 2002, S. 307–311

[65] McInnes, Colin R.: *Space-based geoengineering: Challenges and requirements,* Proceedings of the Institution of Mechanical Engineers, Part C: Journal of Mechanical Engineering Science, 224, Nr. 3, 2010, S. 571–580

[66] Sanchez, J. P.; McInnes, C.: *Asteroid Resource Map for Near-Earth Space,* Journal of Spacecraft and Rockets, 48, Nr. 1, 2011, S. 153–165

[67] Angel, Roger: *Feasibility of cooling the Earth with a cloud of small spacecraft near the inner Lagrange point (L1),* Proceedings of the National Academy of Sciences, 103, Nr. 46, 2006, S. 17184–17189

[68] Glaser, P. E.: *Power from the sun: Its future,* Science (New York, N.Y.), 162, Nr. 3856, 1968, S. 857–861

[69] Kennedy, Robert G.; Roy, Kenneth I.; Fields, David E.: *Dyson Dots: Changing the solar constant to a variable with photovoltaic lightsails,* Acta Astronautica, 82, Nr. 2, 2013, S. 225–237

[70] Kosugi, Takanobu: *Role of sunshades in space as a climate control option,* Acta Astronautica, 67, 1-2, 2010, S. 241–253

[71] Hufenbach, Bernhard, et al: *International missions to lunar vicinity and surface-near-term mission scenario of the Global Space Exploration Roadmap,* 2015

[72] Laurini, Kathleen C., et al: *The global exploration roadmap and expanding human/robotic exploration mission collaboration opportunities,* 2015

[73] ESA: *Luna facility brings Moon to Earth.* Website: https://www.esa.int/About_Us/EAC/Luna_facility_brings_Moon_to_Earth [accessed: 31.03.2021]

[74] NASA: *OSAM-1: On-Orbit Servicing, Assembly and Manufacturing-1.* Website: https://nexis.gsfc.nasa.gov/OSAM-1.html [accessed: 31.03.2021]

[75] ESA: *Types of orbits: Polar orbit and Sun-synchronous orbit (SSO).* Website: https://www.esa.int/Enabling_Support/Space_Transportation/Types_of_orbits#lagrange [accessed: 31.03.2021]

[76] ESA: *Exploration of the Moon: About PROSPECT.* Website: https://exploration.esa.int/web/moon/-/59102-about-prospect [accessed: 31.03.2021]

[77] Tatay-Sanguesa Jose: *Robust Multi-objective Trajectory OptimizationTool in the CR3BP,* 8th ICATT (International Conference on Astrodynamics Tools and Techniques), 2021

[78] Elon Musk: *Making Humans a Multiplanetary Species,* The 68th International Astronautical Congress, 2017

[79] Jensen, Jessica: *Starship Users Guide*

[80] Schlueter, Martin: *MIDACO software performance on interplanetary trajectory benchmarks,* Advances in Space Research, 54, Nr. 4, 2014, S. 744–754

[81] Farquhar, Robert W.; Dunham, David W.; et al.: *Utilization of libration points for human exploration in the Sun–Earth–Moon system and beyond,* Acta Astronautica, 55, 3-9, 2004, S. 687–700

[82] Fasoulas, Stefanos; Zimmermann, Frank: *Bahnmechanik für Raumfahrtsysteme: Vorlesung 9 - Interplanetare Bahnen.* Stuttgart, University of Stuttgart, Institute of Space Systems, Lecture slides, 2021.

[83] Schwinning Marius: *Mission Analysis for future Lunar Surface Exploration.* Stuttgart, University of Stuttgart, Institute of Space Systems, Dissertation, 2021.

[84] Davis, Diane C., et al: *Heliocentric escape and lunar impact from near rectilinear halo orbits,* 2019

[85] Kakoi, Masaki: *Design of transfers from Earth-Moon L 1/L2 libration point orbits to a destination object,* 2015

[86] DeBenedictis, Erika A.: *Autonomous Navigation System for Spacecraft Using Low-Thrust Trajectories,* Journal of Propulsion and Power, 28, Nr. 2, 2012, S. 380–386

[87] Messerschmid, Ernst; Fasoulas, Stefanos: *Raumfahrtsysteme,* Springer, 2017

[88] Jeffrey Kluger: *Dueling Superpowers, Rival Billionaires. Inside the New Race to the Moon.* Website: https://time.com/longform/race-to-the-moon/ [accessed: 31.03.2021]

[89] Bruce Einhorn: *The Race for Mars Takes China-U.S. Tensions Into Outer Space.* Website: https://www.bloomberg.com/news/articles/2021-01-20/will-u-s-or-china-reach-mars-first-space-race-heats-up [accessed: 31.03.2021]

[90] SpaceX: *Starship SN10 High-Altitude Flight Test.* Website: https://www.spacex.com/vehicles/starship/ [accessed: 31.03.2021]

[91] O'Neill, Gerard K.: The colonization of space. In: *Space Manufacturing Facilities,* 1974, S. 2041

[92] Schroeder, J. M.; Gully, J. H.; Driga, M. D.: *Electromagnetic launchers for space applications,* IEEE Transactions on Magnetics, 25, Nr. 1, 1989, S. 504–507

[93] McNab, I. R.: *Launch to space with an electromagnetic railgun,* IEEE Transactions on Magnetics, 39, Nr. 1, 2003, S. 295–304

[94] Powell, James; Maise, George; et al.: Maglev Launch : Ultra-low Cost, Ultra-high Volume Access to Space for Cargo and Humans, S. 121–136

[95] Wright, Michael R.; Kuznetsov, Steven B.; Kloesel, Kurt J.: *A Lunar Electromagnetic Launch System for In Situ Resource Utilization,* IEEE Transactions on Plasma Science, 39, Nr. 1, 2011, S. 521–528

[96] Snow, William R.; Kolm, Henry H.: *Electromagnetic launch of lunar material,* 1992

[97] Ehresmann, Manfred: *Mission and System Analysis for Lunar Massdriver Applications.* Master Thesis, IRS-16-035, Institute of Space Systems University of …, 2016.

[98] Ehresmann, Manfred; Gabrielli, Roland Atonius; et al.: *Lunar based massdriver applications,* Acta Astronautica, 134, 2017, S. 189–196

[99] McNab, I. R.; Beach, F. C.: *Naval Railguns,* IEEE Transactions on Magnetics, 43, Nr. 1, 2007, S. 463–468

[100] Hundertmark, S.; Vincent, G.; Simicic, D.; Schneider, M.: *Increasing Launch Efficiency With the PEGASUS Launcher,* IEEE Transactions on Plasma Science, 45, Nr. 7, 2017, S. 1607–1613

[101] O'Neill, Gerard K.; Billingham, John; et al.: *Space resources and space settlements,* NASA, SP-428, 1977

[102] O'Neill, Gerard K.; O'Leary, Brian: *Space-Based Manufacturing from Nonterrestrial Materials,* American Institute of Aeronautics and Astronautics, 1977

[103] Bresie, D. A.; Andrews, J. A.: *Design of a reluctance accelerator,* IEEE Transactions on Magnetics, 27, Nr. 1, 1991, S. 623–627

[104] Daldaban, Ferhat; Sari, Vekil: Design and implementation of a three-coil linear reluctance launcher. In: *2014 16th International Power Electronics and Motion Control Conference (PEMC),* S. 1084–1088

[105] Thor Barrera, Robby Beard: *Exploration and verification analysis of a linear reluctance accelerator,* IEEE, 2014

[106] Kolm, Henry; Mongeau, Peter; Williams, F.: *Electromagnetic launchers,* IEEE Transactions on Magnetics, 16, Nr. 5, 1980, S. 719–721

[107] Luigi Mascolo; Adrian Stoica: *Electro-Magnetic Launchers on the Moon: A Feasibility Study,* Piscataway, NJ, IEEE, 2018

[108] Lipinski, R. J.; Beard, S.; et al.: *Space applications for contactless coilguns,* IEEE Transactions on Magnetics, 29, Nr. 1, 1993, S. 691–695

[109] Andrews, J. A.; Devine, J. R.: *Armature design for coaxial induction launchers,* IEEE Transactions on Magnetics, 27, Nr. 1, 1991, S. 639–643

[110] Ciceron, Jérémie; Badel, Arnaud; et al.: *Superconducting magnetic energy storage and superconducting self-supplied electromagnetic launcher,* The European Physical Journal Applied Physics, 80, Nr. 2, 2017, S. 20901

[111] Li, Shuai; Lucey, Paul G.; et al.: *Direct evidence of surface exposed water ice in the lunar polar regions,* Proceedings of the National Academy of Sciences of the United States of America, 115, Nr. 36, 2018, S. 8907–8912

[112] Kring, David ; Stopar, Julie: *Lunar South Pole Atlas.* Website: https://www.lpi.usra.edu/lunar/lunar-south-pole-atlas/ [accessed: 31.03.2021]

[113] Stopar, Julie; Meyer, Heather: *Topographic Map of the Moon's South Pole (80° S to Pole),* Lunar and Planetary Institute, Regional Planetary Image Facility, 2019

[114] Ignatiev, A.; Freundlich, A.; Duke, M.; Rosenberg, S.: *New architecture for space solar power systems: Fabrication of silicon solar cells using in-situ resources,* NIAC Phase I Final Report, 2000

[115] Vasavada, Ashwin R.; Bandfield, Joshua L.; et al.: *Lunar equatorial surface temperatures and regolith properties from the Diviner Lunar Radiometer Experiment,* Journal of Geophysical Research: Planets, 117, E12, 2012, n/a-n/a

[116] Stopar, Julie: *Near-Surface Temperatures Modeled for the Moon's South Pole (85° S to Pole),* 2019. Website: https://repository.hou.usra.edu/bitstream/handle/20.500.11753/1336/SPole_85S_DLREallT_v20190829.pdf?sequence=1&isAllowed=y [accessed: 31.03.2021]

[117] Fristad, K., et al.: *Ideal landing sites near the lunar poles,* 2004

[118] van Susante, P.: *Design and Construction of a lunar south pole infrared telescope (LSPIRT),* 2002

[119] Gilmour, C. M., et al: *Artemis 2024: Potential EVA targets at the lunar south pole,* 2020 (2326)

[120] Sharpe, Burton L.; Schrunk, David G.: Malapert Mountain Revisited. In: *Space 2002 and Robotics 2002,* 2002, S. 129–135

[121] Dunbar, Brian: *Moon's South Pole in NASA's Landing Sites,* NASA, NASA, 15, 2019

[122] Roesler, Gordon: *Mass Estimate for a Lunar Resource Launcher Based on Existing Terrestrial Electromagnetic Launchers,* Machines, 1, Nr. 1, 2013, S. 50–62

[123] Kaye, R.; Turman, B.; et al.: Induction coilgun for EM mortar. In: *2007 16th IEEE International Pulsed Power Conference:* IEEE, 2007, S. 1810–1813

[124] Turman, B. N.; Kaye, R. J.; et al.: *EM mortar technology development for indirect fire.* 2006

[125] Joseph V. Minervini: *A pathway to fusion energy based on high-field REBCO superconducting magnets.* Website: https://indico.cern.ch/event/775529/contributions/3309887/attachments/1828600/2993908/Minervini_HTS-for-Fusion-WAMHTS-5.pdf [accessed: 31.03.2021]

[126] Creely, A. J.; Greenwald, M. J.; et al.: *Overview of the SPARC tokamak,* Journal of Plasma Physics, 86, Nr. 5, 2020, S. 12033

[127] Doyle, M. R.; Samuel, D. J.; et al.: *Electromagnetic aircraft launch system-EMALS,* IEEE Transactions on Magnetics, 31, Nr. 1, 1995, S. 528–533

[128] Gerlach Lothar: *Inside a solar cell.* Website: https://www.esa.int/Enabling_Support/Space_Engineering_Technology/Inside_a_solar_cell [accessed: 31.03.2021]

[129] CESI: *Space Solar Cells.* Website: https://www.cesi.it/space-solar-cells/ [accessed: 31.03.2021]

[130] Climate Investment Funds: *BHADLA: Solar parks transform India's energy landscape.* Website: https://www.climateinvestmentfunds.org/CIF10/india/bhadla [accessed: 31.03.2021]

[131] Sanjay Priya: *With 2,245 MW of Commissioned Solar Projects, World's Largest Solar Park is Now at Bhadla.* Website: https://mercomindia.com/world-largest-solar-park-bhadla/ [accessed: 31.03.2021]

[132] Federal Ministry for Economic Affairs and Energy: *Energy Data: Complete Edition: Gesamtausgabe der Energiedaten - Datensammlung des BMWi.xlsx.* Website: https://www.bmwi.de/Redaktion/DE/Artikel/Energie/energiedaten-gesamtausgabe.html [accessed: 31.03.2021]

[133] Battery University: *Supercapacitors Information.* Website: https://batteryuniversity.com/learn/article/whats_the_role_of_the_supercapacitor [accessed: 31.03.2021]

[134] French, Bevan M.; Heiken, Grant; Vaniman, David: *Lunar sourcebook: A user's guide to the Moon,* CUP Archive, 1991

[135] Kaempgen, Martti; Chan, Candace K.; et al.: *Printable thin film supercapacitors using single-walled carbon nanotubes,* Nano letters, 9, Nr. 5, 2009, S. 1872–1876

[136] Chen, Zheng; Wen, Jing; et al.: *High-Performance Supercapacitors Based on Hierarchically Porous Graphite Particles,* Advanced Energy Materials, 1, Nr. 4, 2011, S. 551–556

[137] Rani, Janardhanan R.; Thangavel, Ranjith; et al.: *An Ultra-High-Energy Density Supercapacitor; Fabrication Based on Thiol-functionalized Graphene Oxide Scrolls,* Nanomaterials (Basel, Switzerland), 9, Nr. 2, 2019

[138] Manan Arya, Lee Nicolas, Pellegrino Sergio: *Ultralight structures for space solar power satellites,* 2016

[139] Rieber Richard: *Principals of Solar Sailing.* Website: https://www.colorado.edu/faculty/kantha/sites/default/files/attached-files/reiber_solar_sailing.pdf [accessed: 31.03.2021]

[140] ESA: *Solar sail.* Website: https://www.esa.int/ESA_Multimedia/Images/2014/01/Solar_sail [accessed: 31.03.2021]

[141] Macdonald, Malcolm: *Advances in Solar Sailing,* Berlin, Heidelberg, s.l., Springer Berlin Heidelberg, 2014

[142] The Planetary Society: *Cosmos 1.* Website: https://planetary.s3.amazonaws.com/web/assets/pictures/20170724_cosmos1-hr.jpg [accessed: 31.03.2021]

[143] The Planetary Society: *Solar Cruiser.* Website: https://www.planetary.org/space-images/solar-cruiser-illustration [accessed: 31.03.2021]

[144] Perakis, Nikolaos; Schrenk, Lukas E.; et al.: *Project Dragonfly: A feasibility study of interstellar travel using laser-powered light sail propulsion,* Acta Astronautica, 129, 2016, S. 316–324

[145] Dervan, Jared: *Solar & Electric Sailing Overview,* 2018

[146] Bookless, John; McInnes, Colin: *Control of Lagrange point orbits using solar sail propulsion,* Acta Astronautica, 62, 2-3, 2008, S. 159–176

[147] Tsuda, Yuichi: *An attitude control strategy for spinning solar sail,* IFAC Proceedings Volumes, 40, Nr. 7, 2007, S. 401–406

[148] Funase, Ryu; Shirasawa, Yoji; et al.: *On-orbit verification of fuel-free attitude control system for spinning solar sail utilizing solar radiation pressure,* Advances in Space Research, 48, Nr. 11, 2011, S. 1740–1746

[149] Yuan Chai, Jianjun Luo, Mingming Wang: *Uncertainty estimation based game control for attitude regulation,* 71st International Astronautical Congress, CyberSpace Edition, 2020

[150] Karen Weise: *Jeff Bezos Commits $10 Billion to Address Climate Change: The world's richest man unveiled a fund to help climate scientists and activists, an escalation of his philanthropic efforts.* Website: https://www.nytimes.com/2020/02/17/technology/jeff-bezos-climate-change-earth-fund.html [accessed: 31.03.2021]

[151] Rupert Neate: *Elon Musk pledges $100m to carbon capture contest: Fifteen teams will get $1m to develop ideas, with a $50m prize awaiting the winner.* Website: https://www.theguardian.com/environment/2021/feb/08/elon-musk-pledges-100m-to-carbon-capture-contest [accessed: 31.03.2021]

[152] Hickel, Jason: *Quantifying national responsibility for climate breakdown: An equality-based attribution approach for carbon dioxide emissions in excess of the planetary boundary,* The Lancet Planetary Health, 4, Nr. 9, 2020, e399-e404

[153] Koumi, Elissavet; Manghaipathy, Pavithra: *Moon Village Association (MVA) Global Collaboration Framework for Lunar Missions,* 2020

[154] Espace & Exploration: *Technical data sheet: Falcon Heavy.* Website: https://en.wikipedia.org/wiki/Falcon_Heavy#cite_note-EspaceEtExplorationNo51-66 [accessed: 31.03.2021]

[155] MacInnis, Dillon: *Falcon_Users_Guide_082020.* Website: https://www.spacex.com/media/Falcon_Users_Guide_082020.pdf [accessed: 31.03.2021]

[156] Space Launch Report: *Space Launch Report: SpaceX Falcon Heavy.* Website: https://www.spacelaunchreport.com/falconH.html#components [accessed: 31.03.2021]

[157] SpaceX: *Capabilities&Services.* Website: https://www.spacex.com/media/Capabilities&Services.pdf [accessed: 31.03.2021]

[158] Space X: *SpaceX Merlin.* Website: https://web.archive.org/web/20130715094112/http://www.spacex.com/falcon9#merlin_engine [accessed: 31.03.2021]

Appendix

A Detailed Roadmap

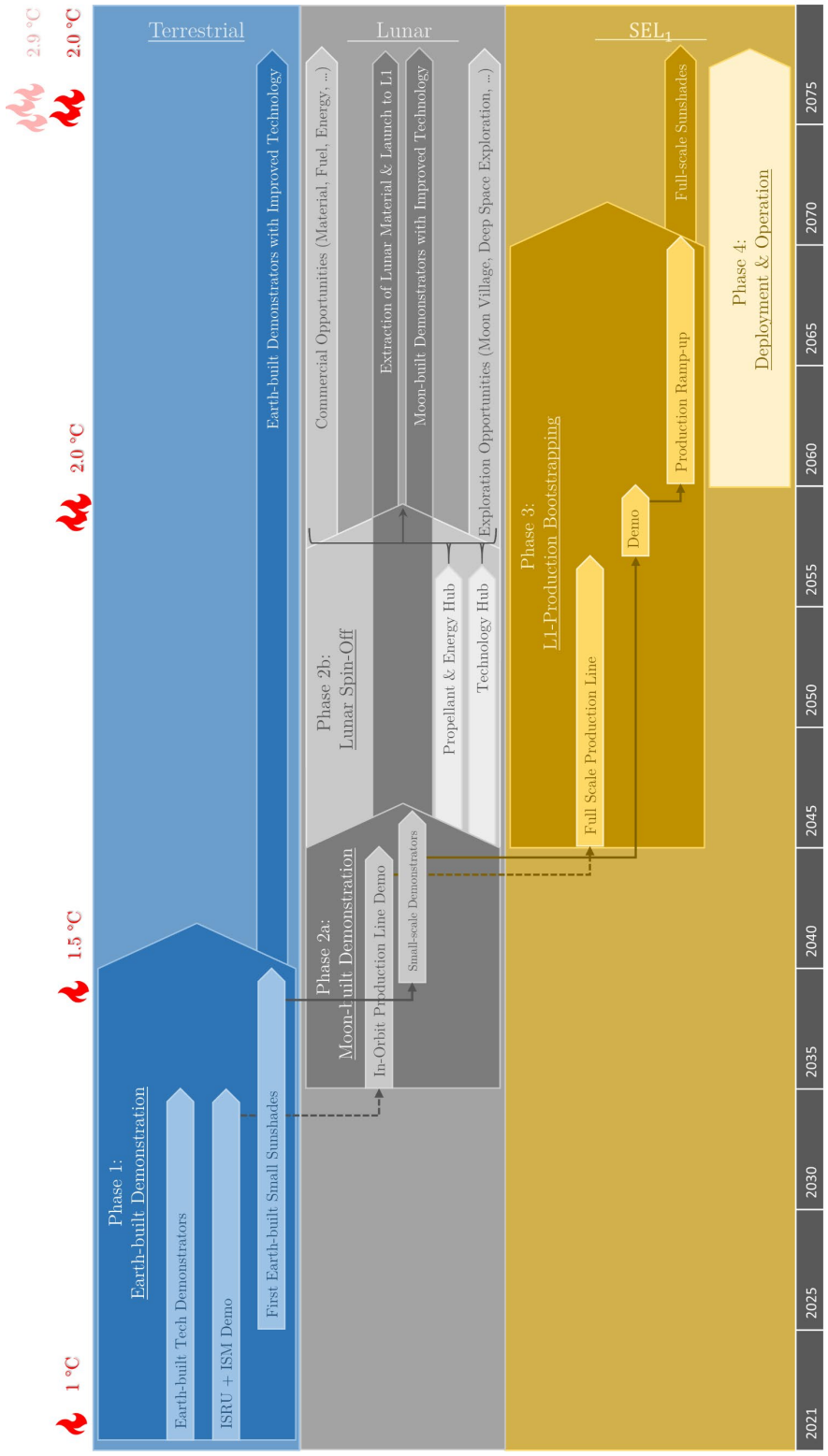

Figure 42: Roadmap for an International Planetary Sunshade.

B Overview of International Launchers

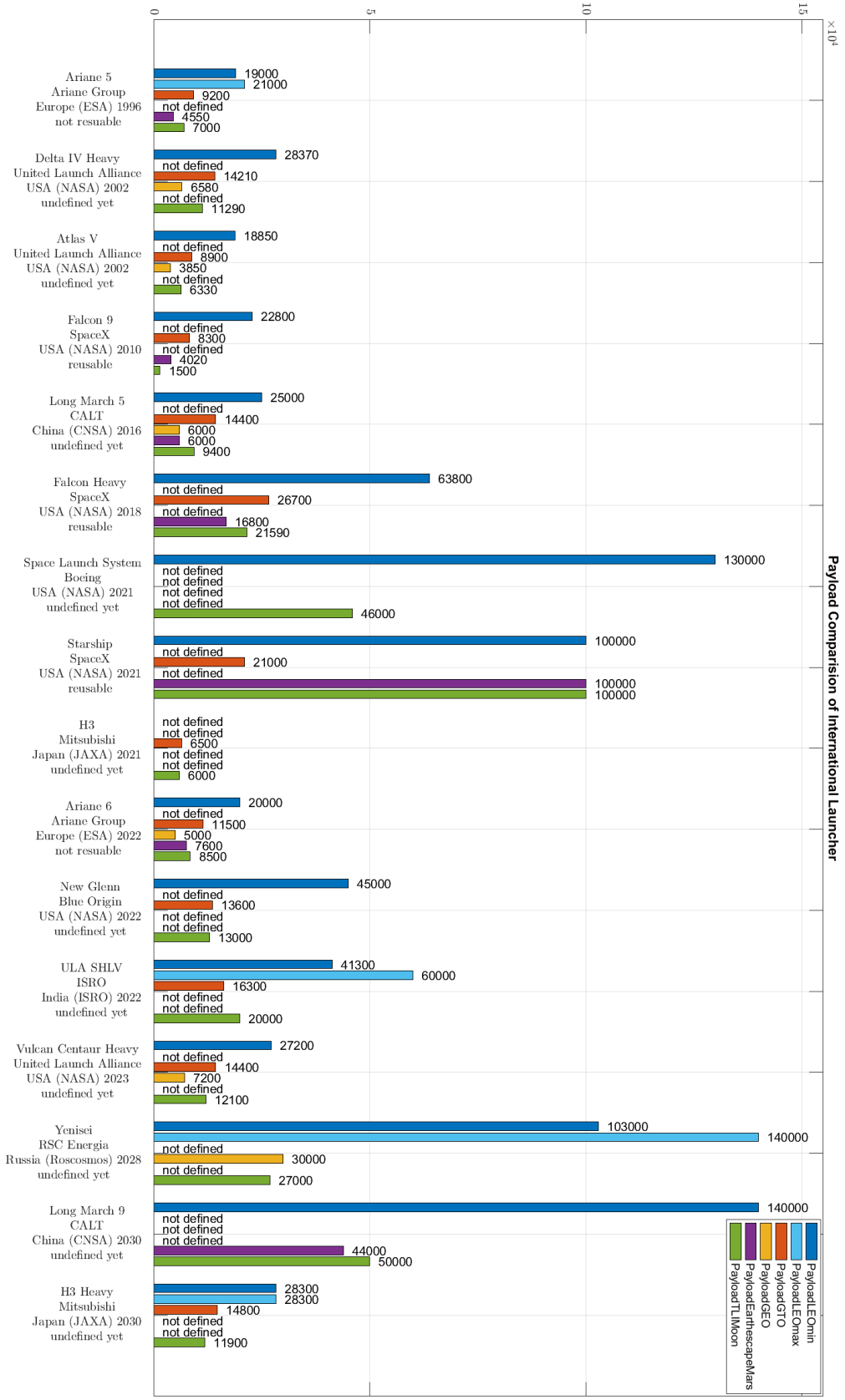

Figure 43: Overview of International Launchers.

C Launcher Calculations Falcon Heavy

The calculation of the TLI payload as well as the Lunar Orbit Payload is based on the following Falcon Heavy specifications and characteristics [154–158; 158]:

Characteristics	First stage core unit	Second stage	Payload fairing	Payload (LEO)
Engines	9 × Merlin 1D (sea level)	1 × Merlin 1D (vacuum)	N/A	N/A
Dry Mass in [kg]	22,200	4,000	1,700	63,800
Fueled mass in [kg]	433,100	111,500	N/A	N/A

Table 24: Falcon Heavy stage masses.

Characteristics	Merlin 1D (vacuum)	Merlin 1D (sea level)
Effective exhaust velocity ($\mathbf{v_e}$) in $[\frac{\mathrm{km}}{\mathrm{s}}]$	3.05	2.77

Table 25: Falcon Heavy Engine Effective exhaust velocity

Following orbit parameters were estimated for the calculation:

Characteristics	LEO (h = 600 km)	TLO
Distance regarding Earth in [km]	6,978	384,400
Standard gravitational parameter of Earth in $[\mathrm{m}^3\mathrm{s}^{-2}]$	3.986 x 10^{14}	N/A

Table 26: Orbital Parameter for Falcon Heavy Calculation.

Calculations based on following equations [87]:

Vis-viva equation: $$v^2 = \mu \cdot (\tfrac{2}{r} - \tfrac{1}{a}) \quad (1)$$

Tsiolkovsky rocket equation: $$\Delta v_{1\to 2} = c_e \cdot ln\left(\tfrac{m_1}{m_2}\right) \quad (2)$$

Calculation

Stage 1: two boosters, upper stage, payload fairing, payload

Total take-off mass:

$$m_{total} = 3 \cdot 433{,}100\ kg + 111{,}500\ kg + 1{,}700\ kg + 63{,}800\ kg$$

$$m_{total} = 1476{,}300\ kg = m_{1s}$$

Mass after Stage 1 burn:

$$m_{1e} = 433{,}1000 + \ 2 \cdot 22{,}200\ kg + \ 111{,}500\ kg + 1{,}700\ kg + 63{,}800\ kg$$

$$m_{1e} = 654{,}500\ kg$$

ΔV after Stage 1 based on (2) at sea level:

$$\Delta V_1 = 2{,}253\ \tfrac{m}{s}$$

Stage 2: Fairing and boosters jettisoned, core stage, upper stage, payload remaining

$$m_{2s} = 433{,}100\ kg + 111{,}500\ kg + 63{,}800\ kg$$

$$m_{2s} = 608{,}400\ kg$$

Mass after Stage 2 burn:

$$m_{2e} = 22{,}200\ kg + 111{,}500\ kg + 63{,}800\ kg$$

$$m_{2e} = 197{,}500\ kg$$

ΔV after Stage 2 based on (2):

$$\Delta V_2 = 3{,}117\ \tfrac{m}{s}$$

Velocity V_2 after Stage 2:

$$V_2 = 5{,}370\ \frac{m}{s}$$

Stage 3: Core jettisoned, core stage, upper stage, payload remaining

$$m_{3s} = 111{,}500\ kg + 63{,}800\ kg$$

$$m_{2s} = 175{,}300\ kg$$

Mass after Stage 3 burn:

$$m_{2e} = 4{,}000\ kg + 63{,}800\ kg$$

$$m_{2e} = 67{,}800\ kg$$

ΔV after Stage 3 based on (2) in vacuum:

$$\Delta V_3 = 2{,}897\ \tfrac{m}{s}$$

Velocity V_3 after Stage 3:

$$V_3 = 8{,}267\ \frac{m}{s}$$

The final speed in LEO with an altitude of h = 600 km based on (1) would be:

$$V_{LEO} = 7{,}558 \ \frac{m}{s}$$

Due to atmospheric drag and gravitational loss a reduction of the final velocity V_3 to V_{LEO} with a ΔV-reduction of

$$\Delta V = \ \Delta V_3 - \ V_{LEO} = 709 \ \frac{m}{s}$$

is estimated.

Based on a Hohmann transfer from LEO to TLO the characteristic ΔV for the transfer is calculated based on (1):

Characteristics	LEO (h = 600 km)	TLO
orbital radius in [km]	6,978	384,400
velocity on circular orbit in $[\frac{m}{s}]$	7,558	1,018
ΔV needed for transfer in $[\frac{m}{s}]$	3,033	961
total ΔV needed for transfer in $[\frac{m}{s}]$	3,995	

Table 27: Hohmann transfer parameters from LEO to TLO.

For the calculation of the TLI payload based on (1) only the required ΔV in LEO is considered. The payload-to-fuel-ratio $(\frac{m_p}{m_f})$ was calculated to

$$\frac{m_p}{m_f} = 0.63$$

And with a safety margin of 5% equation (1) delivers an estimated TLI payload of

$$m_{P,TLI} = 21{,}590 \text{ kg} \ .$$

Considering the whole Hohmann transfer to the defined TLO with a safety margin of 5% fuel would enable a total payload of

$$m_{P,TLO} = 14{,}890 \text{ kg} \ .$$